THE FLORIDA STATE UNIVERSITY

COLLEGE OF ARTS AND SCIENCES

SEARCH FOR LARGE EXTRA DIMENSIONS IN THE EXCLUSIVE PHOTON + MISSING ENERGY CHANNEL IN $P\overline{P}$ COLLISIONS

By

JOSE A. LAZOFLORES

A Dissertation submitted to the
Department of Physics
in partial fulfillment of the
requirements for the degree of
Doctor of Philosophy

Degree Awarded:
Summer Semester, 2006

The members of the Committee approve the Dissertation of Jose A. Lazoflores defended on April 28, 2006.

Vasken Hagopian
Professor Co-Directing Dissertation

Sharon Hagopian
Professor Co-Directing Dissertation

Gregory A. Riccardi
Outside Committee Member

Howard Baer
Committee Member

Simon Capstick
Committee Member

The Office of Graduate Studies has verified and approved the above named committee members.

This thesis is dedicated to my family and, in particular, to my mother...
She always told me that there was nothing I could not do as long as I believe in myself. I love my mother for many reasons, but I specially love her for that.

ACKNOWLEDGEMENTS

This dissertation is a cumulative effort of many years of research conducted by a large number of people. I would like to thank everyone who has contributed to this work in one way or another. First and foremost, I would like to thank my advisor and co-advisor, Professor Vasken Hagopian and research scientist Sharon Hagopian, for their continuous support and interest in this analysis and in my work as a graduate student at the Florida State University (FSU). Their expertise, guidance and patience were greatly appreciated as they helped to get me started on many projects that needed the input of experienced high energy physicists.

Next I would like to thank all the members of the FSU High Energy Physics (HEP) group for their patience, guidance, and advice based on their expertise. In no particular order: Thanks to Professor Yuri Gershtein for his help on many subjects of which he is an expert. In particular his guidance on electromagnetic object identification, the EMCal, and statistical analysis proved to be very helpful in the development of this study. Dr Andrew Askew guided me through some of the last calculation needed in order to finish this work in a proper way. In particular, thanks for his help on the acceptance calculation, bremsstrahlung veto algorithm development, and systematic error analysis among many other subjects of which he is an expert. I benefited greatly from Professor Todd Adams expertise on data analysis and the data format used at DØ . In particular, his help in event revertexing and Monte Carlo (MC) event generation proved to be indispensable. Professor Harrison Prosper for his guidance in statistical analysis, programing and on the data format used at DØ . He is a person of many talents and patience being one of his virtues. From professor Susan Blessing I learned the subtleties of data analysis and attention to detail which helped me to identify problems that otherwise would have gone un-noticed, until they became big problems. Professor Horst Wahl for sharing his expertise in jet energy scale, technical knowledge of the DØ detector and experimental particle physics in general. His door was always open and he was always willing to help. Professors Howard Baer and Joseph Owens

for their help in understanding the theory and the proper way to generate signal events. They were always willing to help and their doors were always open.

At the DØ collaboration, I like to thank the New Phenomena (NP) group for their input in identifying problems and their advise on how to solve them. From the forward preshower (FPS) group I learned about the technical aspects of data analysis and acquisition. I was first introduced to data reconstruction and analysis while working on the commissioning of the FPS. The experience I gained while working for the FPS proved to be extremely useful many times during the development of this work. I also like to thank the DØ community as a whole for providing a working environment that is friendly and optimized for learning. There, I learned about other cultures and customs from the diverse community that is DØ .

Here at FSU, I like to thank my fellow students and peers, past and present. Their friendly nature helped me maintain my sanity in times when I thought I was losing it. Their presence and sense of humor helped to relieve the pressures that this work sometimes produces. Their expertise in their particular area of research helped me gain a broader understanding of physics, in general, and HEP, in particular. In chronological order, they are: Craig Group, Jorge O'Farrill, Yuri Lebedev, Chris Jackson, Sinjini Singupta, Jelena Trbovic, Daekwang Kau, Suharyo Sumowidagdo, Dan Duggan, Tzvetalina Stavreva, Fernando Febres Cordero, Paulo Rottmann, Edgar Carrera, and Azar Mustafayev among others.

I like to acknowledge the influence that my undergraduate professor had in my decision to change from engineering to physics. Professor Robert Fleck, at Embry-Riddle University, showed me that science can be as fun and fulfilling as flying fighter aircrafts for the US Air Force. In particular he introduced me to particle physics when he recommended that I read "The God Particle," by Leon Lederman. He also exposed me to the beauty of astronomy and by doing so, he awoke in me a desire to learn more about the beauty of the universe and to try to make sense of it.

Finally, I want to thank my family. It has been a long journey in my education and my family has stood by me the entire way in more ways that I can count. I credit my mother's patience, love and encouragement as the reason why I have come this far. I don't consider this to be my work alone, but our work. Her influence can be seen on every page of this dissertation and in my life.

TABLE OF CONTENTS

List of Tables . . . viii

List of Figures . . . x

Abstract . . . xiv

1. Introduction . . . 1

2. Theories . . . 3
- 2.1 The Standard Model . . . 3
- 2.2 Motivation for New Physics . . . 6
- 2.3 Graviton Production at Collider Experiments . . . 10

3. Experimental Apparatus . . . 14
- 3.1 Definitions and Conventions . . . 14
- 3.2 The Tevatron . . . 16
- 3.3 The DØ Detector . . . 20
- 3.4 The DØ Trigger System . . . 37

4. Event Reconstruction . . . 44
- 4.1 Electromagnetic Object Reconstruction . . . 44
- 4.2 Jet Reconstruction . . . 51
- 4.3 Muon Reconstruction . . . 55
- 4.4 Track Reconstruction . . . 59
- 4.5 Vertex Reconstruction . . . 60
- 4.6 $\not\!\!E_T$ Computation . . . 62

5. The Analysis . . . 64
- 5.1 Data and Event Selection . . . 64
- 5.2 Backgrounds . . . 71
- 5.3 Signal Analysis . . . 80

6. The Results and Conclusion . . . 91

A. Cosmic Bremsstrahlung Events . . . 93
- A.1 Data and EM Object Selection . . . 93

A.2 Bremsstrahlung Event Identification 95
A.3 Efficiencies 96
A.4 Conclusion 96
A.5 The Code 97

B. Track Match Efficiency Calculation 105
B.1 Data Selection 105
B.2 The Efficiency Equation 106
B.3 Error Calculation 109
B.4 Results 109

REFERENCES 110

BIOGRAPHICAL SKETCH 114

LIST OF TABLES

2.1 Quark family in the Standard Model and some individual properties. The quarks have been divided in terms of their generation with the mass values and ranges obtained from the Particle Data Book [5]. 4

2.2 Lepton family in the Standard Model and some individual properties. The leptons are divided in terms of their generation. [5]. 4

2.3 Gauge bosons and their basic properties in the SM. The bosons are arranged in terms of the force they carry. The masses are a world average including direct measurements [5]. 5

2.4 List of a few baryons and some of their properties. 5

2.5 List of a few Mesons and some of their properties. 6

2.6 *Size of the extra dimensions for $M_D \sim 1$ TeV and different values of n.* . . . 8

4.1 Muon quality definitions for data reconstructed with production release p14. 58

4.2 Luminosity block selection cuts. 63

5.1 Event count after every cut. The photon ID contains all of the cuts as described in the first set of bullets in Section 5.1.2 69

5.2 Background estimates for the single photon and $\not\!\!E_T$ data sample corresponding to the 196 pb^{-1} dataset. 81

5.3 Results of acceptance calculation for signal events processed with PMCS for different values of M_D and number of extra dimensions. 83

5.4 Area of the tails α outside $\pm\delta$ from the mean of a Gaussian distribution . . . 85

5.5 Lower limits of M_D for n = 2,3,4,5,6,7, and 8 assuming 28 signal events. Presented are both, the central value and the 95% CL. 90

6.1 Lower limits of M_D for n = 2, 3, 4, 5, 6, 7, and 8. Presented are both the central value and the 95% CL. The errors noted in the central values are the statistical and systematic errors combined. The largest contribution to the errors comes from the uncertainty of the $\mathcal{L}_{int}$. 91

6.2 Lower limits of M_D (GeV) for n = 3, 4, 5, 6, 7, and 8. Presented are: The central value and the 95% CL for data, 95% CL for the reduced data, 95% for the CDF Run I results, and the 95% CL for the Run I DØ Monojet search. . 92

A.1 Summary of event count for single photon and $\not\!\!E_T$ sample. 95

A.2 Summary of event count for $W \to e\nu$ sample. 95

B.1 Presented is the estimation of the tracking efficiency, ϵ_{trk}, for each combination. 108

LIST OF FIGURES

2.1 95% confidence level upper limits on the inverse square law violating interactions of the form given by Eq. 2.5 9

2.2 *Single Vector boson production at hadron or e^+e^- colliders. Here, $f(\bar{f})$ can be a quark(anti-quark) or a lepton(anti-lepton).* 11

2.3 *Total $\gamma + \not{E}_T$ cross-section versus $E_{T\gamma}^{min}$ for n = 4, 6 and the SM background.* 12

3.1 Schematic of the Run II Fermilab accelerator complex. 17

3.2 Two-dimensional view of the Run II DØ detector, showing the three integral systems outlined in the text. 21

3.3 Three-dimensional view of the DØ silicon microstrip tracker. 23

3.4 Schematic of an observed displaced vertex originating form b or c quarks in a silicon microstrip detector. 24

3.5 Simulation results for the momentum resolution with the Fiber Tracker as a function of pseudo-rapidity for three different p_T values. 25

3.6 Quarter $r-z$ view of the CFT detector at DØ , Shown is a) the nested eight barrel configuration, b) a magnified $r-\phi$ end-view of the two ribbon doublet layers per barrel. 26

3.7 a) Distributions for the position resolution measured in the Fiber Tracker for single muons traversing an interlocking ribbon doublet configuration. The fiber ribbons are pictured in b). 27

3.8 a) The location of the preshower detectors CPS and FPS with their coverage in η in $r-z$ view. b) An $r-\phi$ view of the CPS with a close-up showing the three layers of triangular shaped scintillating fibers. 28

3.9 A cut-away view of the DØ calorimeter. 29

3.10 Schematic view of a portion of the DØ calorimeters showing the transverse and longitudinal segmentation pattern. The shading pattern indicates groups of cells ganged together for signal readout, called a tower readout. The rays indicate η intervals from the center of the detector. 30

3.11 Calorimeter channel configuration in terms of depth and η. 31

3.12 Readout chain of the calorimeter in Run II indicating the three major components: preamplifiers, baseline subtracter and storage circuitry (BLS), and the ADCs. 32

3.13 $r - z$ half-view of the Muon System. Components of both the Forward and Central systems are shown. 34

3.14 Exploded view of the muon wire chambers. 35

3.15 Exploded view of the muon scintillation detectors. 36

3.16 Illustration view of one $r - \phi$ plane in the muon mini-drift tube. The insert shows the cross section of a single Iarocci tube, which consists of eight 1×1 cm^2 cells. 37

3.17 $r - \phi$ segmentation of the muon scintillator pixel counters. 38

3.18 Summary of the three-level DØ Trigger System for Run II with the decision time and bandwidth allocated to each level. 39

3.19 L1 and L2 trigger data pathway. The arrow indicates the direction of data flow. Multiple arrows from a particular subsystem are present for a parallel processing information thus permitting fast trigger decisions and sophisticated physics filters. 40

3.20 Configuration of L2 trigger components. 42

3.21 L3 trigger framework. Data flow is indicated by the direction of the arrow. . 43

4.1 Shower shape for electrons, muons, jets and neutrinos in the Calorimeter. . 45

4.2 A circle of towers in $\eta - \phi$ space. 47

4.3 Schematic of Isolation for the Scone algorithm. 48

4.4 Invariant mass for $Z \rightarrow ee$ from calorimeter. 49

4.5 Data JES correction as a function of jet uncorrected energy (top) and pseudo-rapidity (bottom). Results are shown for $R = 0.5$ cone jet in events with one reconstructed primary vertex and T42 algorithm is applied (see [37] for T42 details). The jet η and physics η are set to the same value. 54

4.6 Example of Segment construction from Drift Tube Hits. 56

5.1 On the left is the p_T distribution for events that pass all the EM ID requirements including HMx7. On the right is the distribution after making the muon veto. 67

5.2 p_T distributions for events passing the following additional requirements: No isolated tracks (left) and the $\not\!\!E_T$ requirement (right). 68

5.3 p_T distributions for events passing the following additional requirements: Veto on bremsstrahlung events (left) and the vertex requirement (right). 68

5.4 p_T distributions for events passing the vertex requirement (left) and the final 70 events (right) superimposed on the p_T distribution of the events passing the photon ID requirements. 69

5.5 EM ID requirements for efficiency as function of the p_T for central photons. 71

5.6 EM ID requirements for efficiency as function of the detector η for central photons. 72

5.7 Distribution of the difference between the z-coordinate from the primary vertex and z-coordinate returned by the pointing program. The data plotted is for $W \to e\nu$ events in data. The triple Gaussian fit was needed because there are three distinct shapes in the distribution. 73

5.8 Distribution of the difference between the z-coordinate from the primary vertex and z-coordinate returned by the pointing program for a sample of bremsstrahlung events. The fitting function is a single Gaussian. 74

5.9 Distribution of the difference between the z-coordinate from the primary vertex and z-coordinate returned by the pointing program for the data events. The fitting function is a combination of the fit functions used to fit the bremsstrahlung and W samples. 75

5.10 Feynman Diagrams for $q\bar{q} \to W^{\pm} \to e^{\pm}\nu$. 76

5.11 Feynman Diagrams for $q\bar{q} \to W^{\pm}\gamma$ production. 77

5.12 Feynman Diagrams for direct $\gamma\gamma$ production. 77

5.13 Examples of dijet production Feynman Diagrams. 78

5.14 Example of Gamma+Jet production Feynman Diagram. 79

5.15 Feynman Diagram of the electroweak process $Z\gamma \to \nu\nu\gamma$. This is the only irreducible background of the single photon and $\not\!\!E_T$ data set. 79

5.16 Illustration of a symmetric 90% condidence interval (unshaded) for a measurement of a single quantity with Gaussian errors. Integrated probabilities, defined by α, are shown. 85

5.17 Cross section as function of M_D for n=2,3,4,5,6,7,8. The black line marks the central value based on the assumption of 56 signal events and the red line marks the 95% CL. 86

5.18 Cross section as function of M_D for n=2,3,4,5,6,7,8. The black horizontal line marks the central value and the red horizontal line marks the 95% CL. The vertical lines point down to the lower limit of the M_D. 87

5.19 Cross section as function of M_D for n=2,3,4,5,6,7,8 after an additional removal of bremsstrahlung events. The black line marks the central value based on the assumption of 28 signal events and the red line marks the 95% CL. . . . 89

A.1 $z - y$ view of a cosmic bremsstrahlung event 99

A.2 ϕ view of a cosmic bremsstrahlung event 100

A.3 The red and green lines depict the vectors from the muon hits, A-segments in this case, to the EM candidate. As this display shows, it is possible to have more than one χ calculation per event. 101

A.4 Cosine of χ distribution for a single photon and $\not\!\!E_T$ data sample passing all of the photon ID requirements including muon veto, isolated track veto, and $\not\!\!E_T$ requirement. The red lines mark the values where the cut was made, which is $|cos(\chi)| > 0.9$. 102

A.5 Cosine of χ distribution for a data sample of $W \rightarrow e\nu$ events passing all of the photon ID requirements including muon veto and $\not\!\!E_T$ requirement. . . . 103

A.6 E_{Cal}/P_{Track} distribution for events in $\cos(\chi) > 0.9$. This distribution indicates that these events are electrons from $W \rightarrow e\nu$ events that happen to line up with muon segments hits. 104

B.1 $Z \rightarrow ee$ peak for diEM events after the certified EM ID requirements as defined in Section 4.1.3. Since these events do not have track match requirements, they includes events in which both EM objects have matched track, 1 EM object has a track match and neither EM objects has a matched track. . . . 106

B.2 $Z \rightarrow ee$ peak for events with one electron having a track match 107

B.3 $Z \rightarrow ee$ peak for events with two electrons having a track match 108

ABSTRACT

A search was conducted for evidence of large extra dimensions (LED) at Fermi National Accelerator Laboratory's Tevatron using the DØ detector. The Tevatron is a $p\bar{p}$ collider at a center of mass energy of 1.96 TeV. Events with particles escaping into extra dimensions will have large missing energy. The search was carried out using data from a total luminosity of 197 ± 13 pb^{-1} with an observable high transverse momentum photon and a large transverse missing energy. The 70 observed events are consistent with photons produced by standard known reactions plus other background processes produced by cosmic muons. The mass limits on the fundamental mass scale at 95% confidence level for large extra dimensions of 2, 4, 6 and 8 are 500 GeV, 581 GeV, 630 GeV, and 668 GeV respectively.

CHAPTER 1

Introduction

The need to understand nature around us has led human beings to undertake one of the greatest journeys in our relatively brief history. To make progress in this journey, we have constructed theories and models that have shed some light into how the universe works. Particle Physics, in particular, is concerned with the understanding of matter at the smallest scales and energy at the largest scales. History records that one of the fundamental ideas of particles physics, the existence of an indivisible piece of matter, started in ancient times. Democritus, about 2500 years ago, postulated that matter could not be divided indefinitely [1]. He referred to these smallest pieces of matter as atoms.

At present times, scientific developments has brought us the *Standard Model* (SM) of Particles and Interactions which is a triumph of theoretical thought and experimentation. It is believed to be a description of the fundamental particles and their interactions and many of its predictions have been confirmed by experimentation. The SM has unified the strong and electroweak interactions under the gauge group $SU(3)_C \otimes SU(2)_L \otimes U(1)_Y$ at energy scales of about 10^2 GeV [3]. To name a few of these experimental successes, the W and Z bosons were discovered at CERN by the $UA1$ and $UA2$ collaborations in 1983 [11, 12], and the top quark was discovered at Fermilab's Tevatron by the $D\emptyset$ and CDF collaborations in 1995 [13, 14]. Despite all of the SM successes, it is not a complete model since gravity is not included. To date, we do not have a unification of gravity with the other forces at energies that can be probed with present day accelerators. String theories appear to be a promising quantum theory of gravity but they require extra space-like dimensions for them to be mathematically consistent. Superstrings, in particular, requires the existence of 7 extra dimensions and it unifies gravity with the other forces at the Plank Scale (M_P) which is of order 10^{19} GeV. A comprehensive review of the SM is beyond the scope of this dissertation,

however, an overview is included in section 2.1 which contains references that the reader can review for a complete discussion.

String theorists have pointed out that explicit calculations in the strong coupling regime using string duality show that the string scale, M_S, receives large corrections and can be lowered from M_P to values comparable with gauge coupling unification [15]. Recently, it was suggested that M_S is not necessarily tied to M_P and can be as low as the electroweak scale in the theories with Large Extra Dimensions (LED) [16]. This is an exciting result to experimentalists because it suggest that a unification of Gravity with the other forces might be proved with present day accelerators. The topic of this dissertation is a search for LED where a proton and an antiproton collide producing a single photon and a massive graviton which then escapes detection and leads to missing transverse momentum. Data collected by the $D\emptyset$ collaboration at Fermilab is used.

CHAPTER 2

Theories

2.1 The Standard Model

The Standard Model (SM) is a Quantum Field theory based on the principle of local gauge symmetry under transformations of the group $SU(3)_C \otimes SU(2)_L \otimes U(1)_Y$[1] as noted in the introduction. It collectively incorporates the strong and electroweak interactions of elementary particles [2]. $SU(3)_C$ is the symmetry group of strong interactions known as Quantum Chromodynamics (QCD). $SU(2)_L \otimes U(1)_Y$ represents the symmetry group describing the unified weak and electromagnetic processes. The model arranges all particles into two groups:

- Fundamental fermions with intrinsic spin $\frac{1}{2}$.
- Gauge vector bosons with integral spin 1.

Fermions are subdivided into colored quarks[2] and non-colored leptons. Tables 2.1 and 2.2 list the names and some properties of quarks and leptons respectively. The SM does not put a limit on the number of generations of quarks and leptons. However, it does require that both leptons and quarks appear in left-handed doublets and right-handed singlets for purposes of electroweak interactions. The fundamental fermions interact by the exchange of gauge bosons. In total, there are twelve such bosons with the following properties:

- Eight massless, colored gluons[3], which mediate the strong interaction, coupling to the color $SU(3)_C$ charge.

[1] C stands for color, L for weak-isospin, and Y for weak-hypercharge

[2] Quarks participate in the strong interaction and come in three colors; red, green, and blue (RGB).

[3] Conventionally named g_i, where $i = 1...8$ and corresponds to the $3^2 - 1$ generations of the $SU(3)$ symmetry group.

Table 2.1: Quark family in the Standard Model and some individual properties. The quarks have been divided in terms of their generation with the mass values and ranges obtained from the Particle Data Book [5].

Particle	Symbol	Electric Charge	Mass(GeV)
Up	u	$+\frac{2}{3}$	$1.5 \sim 4 \times 10^{-3}$
Down	d	$-\frac{1}{3}$	$4 \sim 8 \times 10^{-3}$
Charm	c	$+\frac{2}{3}$	$1.35 \sim 1.5$
Strange	s	$-\frac{1}{3}$	$0.08 \sim 0.130$
Top	t	$+\frac{2}{3}$	174.3 ± 5.1
Bottom	b	$-\frac{1}{3}$	$4.1 \sim 4.4$

Table 2.2: Lepton family in the Standard Model and some individual properties. The leptons are divided in terms of their generation. [5].

Particle	Symbol	Electric Charge	Mass(MeV)
Electron	e	-1	0.511
Electron Neutrino	ν_e	0	$< 3 \times 10^{-6}$
Muon	μ	-1	105.7
Muon Neutrino	ν_μ	0	< 0.19
Tau	τ	-1	1777
Tau Neutrino	ν_τ	0	< 18.2

- Two W bosons ($W^{\pm}$) and a Z^0 for weak interactions.
- The massless photon (γ) which carries the electromagnetic force.

The $W^{\pm}$, Z^0, and the γ mix and form the gauge fields of the $SU(2)_L \otimes U(1)_Y$ sector of the electroweak interactions. Table 2.3 lists the force carriers in terms of their interaction type and it also contains some of their properties. Hadrons are composite particles made of quarks and/or gluons. Protons and antiprotons, for example, are hadrons made of u and d quarks but there are many other possible combinations to make baryons[4] and mesons[5][6]. Tables 2.4 and 2.5 lists some hadrons of the baryon and meson families respectively.

[4]Baryons are particles made from a basic structure of three quarks or antiquarks.
[5]Mesons are color neutral particles with basic structure of one quark and one antiquark

Table 2.3: Gauge bosons and their basic properties in the SM. The bosons are arranged in terms of the force they carry. The masses are a world average including direct measurements [5].

Force Carrier	Force	Mass (GeV)	Electric Charge	Spin	Color Charge
Gluon (g)	Strong	0	0	1	R G B
W^+	Weak	80.417 ± 0.035	1	1	Neutral
W^-		80.417 ± 0.035	-1	1	
Z		91.187 ± 0.007	0	1	
Photon (γ)	EM	0	0	1	Neutral

Table 2.4: List of a few baryons and some of their properties.

Symbol	Name	Quark Content	Electric Charge	Mass (GeV)	Spin
p	Proton	uud	1	0.938	1/2
$\overline{p}$	Antiproton	$\overline{u}\overline{u}\overline{d}$	-1	0.938	1/2
n	Neutron	udd	0	0.940	1/2
Λ	Lambda	uds	0	1.116	1/2
Ω^-	Omega	sss	-1	1.672	3/2

The SM Lagrangian is:

$$\begin{aligned}
\mathcal{L} &= \overline{q}\gamma^{\mu}(i\partial_{\mu} - g_s T_a G^a_{\mu})q - \frac{1}{4}G^a_{\mu\nu}G^{\mu\nu}_a \\
&+ \overline{L}\gamma^{\mu}\left(i\partial_{\mu} - \frac{g}{2}\tau \cdot W_{\mu} - \frac{g^{'}}{2}B_{\mu}Y\right)L \\
&+ \overline{R}\gamma^{\mu}\left(i\partial_{\mu} - \frac{g^{'}}{2}B_{\mu}Y\right)R \\
&- \frac{1}{4}W^a_{\mu\nu}W^{a\mu\nu} - \frac{1}{4}B_{\mu\nu}B^{\mu\nu} \\
&+ \left|\left(i\partial_{\mu} - \frac{g}{2}\tau \cdot W_{\mu} - \frac{g^{'}}{2}B_{\mu}Y\right)\phi\right|^2 - V(\phi) \\
&- G_e(\overline{L}\phi R + \overline{R}\phi^{\dagger}L - h.c.).
\end{aligned} \tag{2.1}$$

which observes the SM gauge symmetries. In Equation 2.1, the first line describes the strong interaction which has a strong coupling constant g_s and involves the gluon gauge field. The second, third and fourth lines describe the electroweak interaction, which has the coupling

Table 2.5: List of a few Mesons and some of their properties.

Symbol	Name	Quark Content	Electric Charge	Mass (GeV)	Spin
π^+	Pion	$u\bar{d}$	+1	0.140	0
π^0	Pion	$u\bar{u}$-$d\bar{d}/\sqrt{2}$	0	0.135	0
π^-	Pion	$d\bar{u}$	-1	0.140	0
K^-	Kaon	$s\bar{d}$	-1	0.494	0
ρ^+	Rho	$u\bar{d}$	+1	0.770	1

constants g and $g^{'}$ and involves the electroweak gauge fields W and B. Had the masses of the particles been zero, the SM could be completely formulated with the first four lines [3]. However, in order to generate mass, the SM spontaneously breaks its own symmetry through a mechanism called the Higgs mechanism. A discussion of the Higgs mechanism is beyond the scope of this dissertation. However, the reader is pointed to reference [4], in particular, and many other publications for an in depth discussion. The fifth line introduces two $SU(2)_L \otimes U(1)_Y$ gauge invariant terms for a scalar field, with the second term, $V(\phi)$, being the Higgs potential. If the Higgs potential is in the following form:

$$V(\phi) = \mu^2\phi^\dagger\phi + \lambda(\phi^\dagger\phi)^2. \tag{2.2}$$

with $\mu^2 < 0$ and $\lambda > 0$, the W and B field will mix to give rise to three massive gauge bosons and one massless gauge boson, listed in table 2.3. The sixth line describes the Yukawa coupling between the fermions and the scalar fields which gives mass to the fermions.

2.2 Motivation for New Physics

The standard model is indeed a great scientific achievement and it is the driving force in particle physics. As mentioned before, nearly all of its predictions have been experimentally confirmed to a high degree of precision. However, there are problems that the SM does not address. A few of these are:

- The hierarchy problem which is discussed below.
- Dark Matter: The motion of stars about the galactic center or that of galaxies in galaxy clusters can not be explained with observed mass distributions. It seems that

the observed matter is not enough to account for the observed motion; more mass is needed. Its properties are not like those of visible matter in that it only manifests itself gravitationally [7]. Therefore, dark matter is not included or predicted by the SM.

- Dark Energy: In cosmology, dark energy is a hypothetical form of energy which permeates all of space and has strong negative pressure. According to the theory of relativity, the effect of such a negative pressure is qualitatively similar to a force acting in opposition to gravity at large scales. Invoking such an effect is currently the most popular method for explaining recent observations that the universe is expanding at an accelerating rate, as well as accounting for a significant portion of the energy balance of the universe [8].

- Unification of gauge couplings: In the SM, unification of gauge couplings does not occur. Super Symmetry (SUSY) is an extension of the SM and it contain coupling unification. However, its predictions have yet to be confirmed by experimentation. For a complete discussion of SUSY, the reader is pointed to Ref. [9].

- Charge Parity (CP) violation and the observed ratio of matter to antimatter: Without CP violation, the existence of the universe as we know it would not be possible. For a complete discussion of CP Violation, see Reference [10].

The hierarchy problem has to do with the difference between the electroweak scale (M_{EW}) and the Planck scale (M_P) where gravity is expected to become as strong as gauge interactions. The smallness and radiative stability of the hierarchy $M_{EW}/M_P \sim 10^{-17}$ has relied on low energy supersymmetry or technicolor for possible explanations. Recent work that utilizes large spatial extra dimensions brings forth a framework for solving the hierarchy problem. In this framework, M_P, M_D and the grand unification scale (M_{GUT}) may be brought down to the TeV scale. The observed weakness of gravity at long distances is postulated to be due to its expansion into sub-millimeter extra spatial dimensions. In this picture the SM fields are localized to a (3+1)-dimensional brane or '3-brane', but the graviton[6] is free to propagate in the extra dimensions, as suggested by Arkani-Hamed, Dimopoulos, and Dvali[16]. The hierarchy problem can be related to the problem of the largeness of the extra dimensions.

[6]The graviton is the particle that carries the gravitational force. It is massless, chargeless and a gauge boson of spin 2.

Table 2.6: *Size of the extra dimensions for $M_D \sim 1$ TeV and different values of n.*

n	1	2	3	4
R	1.2×10^{12} m	0.48 mm	3.6 nm	9.7×10^{-12} m

The relative weakness of gravity with respect to weak forces is related to the size of the compactified extra dimensions, which maybe large in units of TeV^{-1}. In the 3+1-dimensional space, Newton's constant can be expressed as [16, 17]

$$G_N^{-1} = 8\pi R^n M_D^{2+n} \tag{2.3}$$

where $M_D \sim$ TeV is the fundamental mass scale, n is the number of extra dimensions, and R is the radius of the compactified space which is assumed to be a torus. The hierarchy problem is avoided because there is a single fundamental mass scale M_D which is identified with the M_{EW}. Their relationship is

$$R = \frac{1}{\sqrt[n]{8\pi} M_D} \left(\frac{M_P}{M_D} \right)^{2/n}. \tag{2.4}$$

Table 2.6 contains the sizes of the extra dimensions as function of the number of extra dimensions assuming $M_D \sim 1$ TeV. For $n = 1$, R is of the size of the solar system which is very large. This is ruled out by the known inverse square law of the gravitational force at large distances. For the case when $n = 2$, the current limit is $R < 0.19$ mm, as shown in figure 2.1 [18]. The figure shows the 95% confidence level upper limit on the inverse square law violating interactions of the general expressions of the Newtonian gravitational potential:

$$v(r) = -G\frac{m_1 m_2}{r}(1 + \alpha e^{-r/\lambda}). \tag{2.5}$$

The most simple scenario with two large extra dimensions predicts that $\lambda = R$ and $\alpha = 3$ or $\alpha = 4$ for compactification on a 2-sphere or a 2-torus, respectively[19]. In figure 2.1, the intersection point of the 2 extra dimensions noted by the double line and the heavy line labeled Eöt-wash gives us $R < 0.19$ mm [18]. Therefore, $n > 2$ is out of the reach of direct gravitational measurements and the compactification radius drops as a power law.

Observations from the 1987 supernova in the Large Magellanic Cloud placed rather stringent astrophysical bounds on M_D. These bounds come from the requirement that

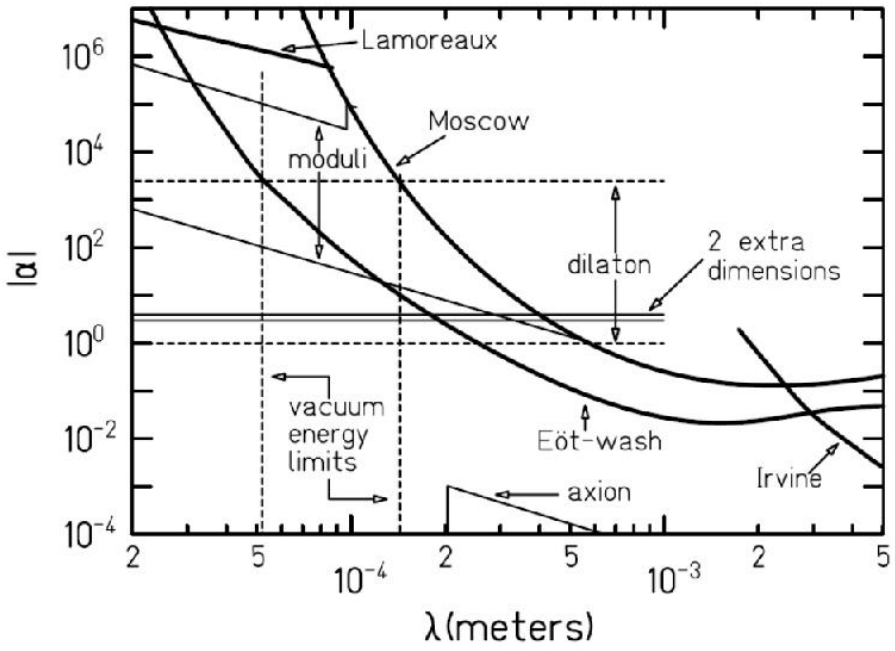

Figure 2.1: 95% confidence level upper limits on the inverse square law violating interactions of the form given by Eq. 2.5

graviton emissions do not rapidly cool the hottest system, such as stars, preventing the occurrence of the observed neutrino flux. This bound has been estimated to be about $M_D \gtrsim 10^{\frac{15-4.5n}{n+2}}$ TeV [16], so that $M_D = 30$ TeV for $n = 2$ and 2 TeV for $n = 3$. Therefore, this astrophysical constraint excludes observable signals for $n = 2$, and limits the available region for $n > 2$.

By first compactifying the higher-dimensional theory and constructing a 3+1 dimensional low-energy effective field theory of the graviton Kaluza-Klein (KK) excitations and their interactions with ordinary matter, the consequences of the supposition that the observed smallness of Newton's constant is a consequence of the large compactified volume of the extra dimensions could be investigated [17][20]. From the $3 + 1$ dimensional space time point of view, a graviton in the extra dimensions is equivalent to a tower of an infinite number of KK states. These states are with mass splittings $M_{KK} = 2\pi/R$, which is $M_k = 2\pi k/R$ $(k = 0, 1, 2, ..., \infty)$. Each of these KK modes is very weakly coupled $(1/M_P)$, however their high multiplicity can give a large enhancement to any effect they mediate. The coupling

becomes proportional to $1/M_D$ rather than $1/M_P$. The gravitational interaction is as strong as the electroweak interaction, since M_D is in the TeV range. The mass of each KK mode corresponds to the modulus of its momentum in the direction transverse to the brane. The scenarios of a massive KK graviton propagating in four dimensions and of a massless graviton propagating in $D = 4+n$ dimensions are equivalent. Note that a massive spin 2 particle has 5 degrees of freedom [17].

2.3 Graviton Production at Collider Experiments

The different excitations of graviton KK modes have mass splittings [17]

$$\Delta m \sim \frac{1}{R} = M_D \left(\frac{M_D}{\overline{M}_P}\right)^{2/n} \sim \left(\frac{M_D}{TeV}\right)^{\frac{n+2}{2}} 10^{\frac{12n-31}{n}} eV, \tag{2.6}$$

where $\overline{M}_P$ is the reduced Planck mass, $\overline{M}_P = M_P/\sqrt{8\pi}$. With $M_D = 1$ TeV and $n = 4$, 6, 8, $\Delta m = 20$ keV, 7 MeV, and 0.1 GeV, respectively. The mass splitting only becomes comparable with the experimental energy resolution for a large number of extra dimensions, but then only a small number of KK modes can be produced and the total cross section is very small and unobservable. When the number of extra dimensions is not too large, less than 10, the enormous number of accessible KK modes can compensate the $1/\overline{M}_P^2$ factor in the scattering amplitude which is the case of interest.

For experimental applications, it is convenient to describe the relevant observables for graviton production in terms of the inclusive cross sections. For not too large n, Δm is small enough that the sum over the different KK states can be replaced by a continuous integration. The differential cross section of inclusive graviton production is[17]:

$$\frac{d^2\sigma}{dtdm} = S_{n-1} \frac{\overline{M}_P^2}{M_D^{2+n}} m^{n-1} \frac{d\sigma_m}{dt}, \tag{2.7}$$

where S_{n-1} is the surface of a unit-radius sphere in n dimensions,

$$S_{n-1} = \frac{2\pi^{n/2}}{\Gamma(n/2)}, \tag{2.8}$$

and $d\sigma_m/dt$ is the differential cross section for producing a single KK graviton of mass m.

From the point of view of the D-dimensional theory, the cross section for an initial brane state $|p_1, p_2\rangle$ to go in a final brane state $|f\rangle$ plus a bulk graviton $|G\rangle$ is then

$$d\sigma = \frac{S_{n-1} m^{n-1} dm}{M_D^{2+n}} |\langle f, G|T^{\mu\nu} h_{\mu\nu}|p_1, p_2\rangle|^2 (2\pi)^4 \delta^4(P_i - P_f) \frac{d\Phi_f}{F(p_1, p_2)} \tag{2.9}$$

where $T^{\mu\nu}$ is the energy-momentum tensor, $d\Phi_f$ is the brane final state phase space, and $F(p_1, p_2)$ is the usual flux factor for two particle collision. This equation agrees with Equation 2.7 [17]. The cleanest process for graviton production comes from events with a photon and $\not{E}_T$ in the final state. This production arises from the sub-process $q\overline{q} \to \gamma G$, pictured in Figure 2.2. The differential cross-section for producing a Kaluza-Klein graviton of mass m

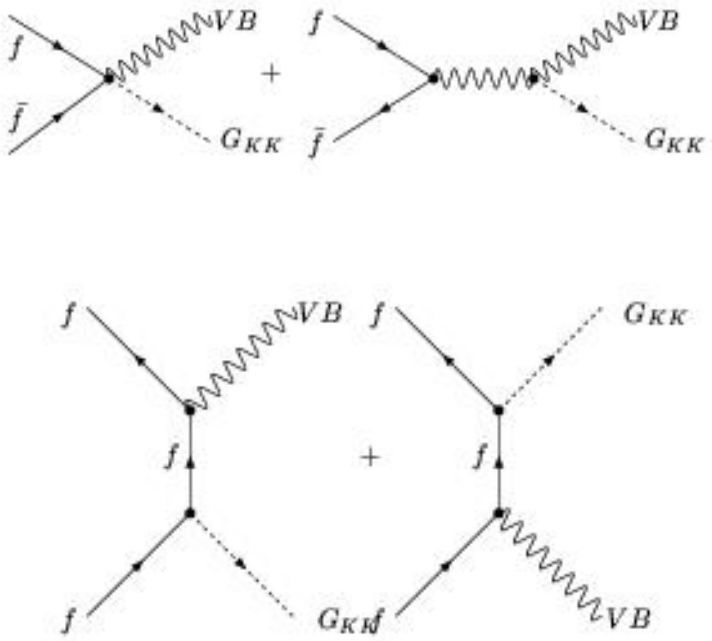

Figure 2.2: *Single Vector boson production at hadron or e^+e^- colliders. Here, $f(\bar{f})$ can be a quark(anti-quark) or a lepton(anti-lepton).*

and a photon in a fermion-antifermion collision is

$$\frac{d\sigma_m}{dt}(f\overline{f} \to \gamma G) = \frac{\alpha Q_f^2}{16 N_f} \frac{1}{s\overline{M}_P^2} F_1(t/s, m^2/s). \tag{2.10}$$

Here Q_f and N_f are the electric charge and number of colors of the fermion f, and F_1 is:

$$\begin{aligned} F_1(x,y) &= \frac{1}{x(y-1-x)}[-4x(1+x)(1+2x+2x^2) \\ &+ y(1+6x+18x^2+16x^3) - 6y^2x(1+2x) + y^3(1+4x)], \end{aligned} \tag{2.11}$$

For the real graviton emission, the production cross section ranges from 10^2 pb to 10^1 pb for different values of n and M_D, which will be shown in Section 5.3 for the chosen kinematic region. In the Figure 2.3, the total cross section for $p\bar{p} \rightarrow \gamma + \not{E}_T$ at $\sqrt{s} = 2$ TeV as a function of $E_{T,\gamma}^{min}$ with $M_D = 1.0$ TeV fixed, and $|\eta_d| < 3$ is shown[7]. The dotted line labeled

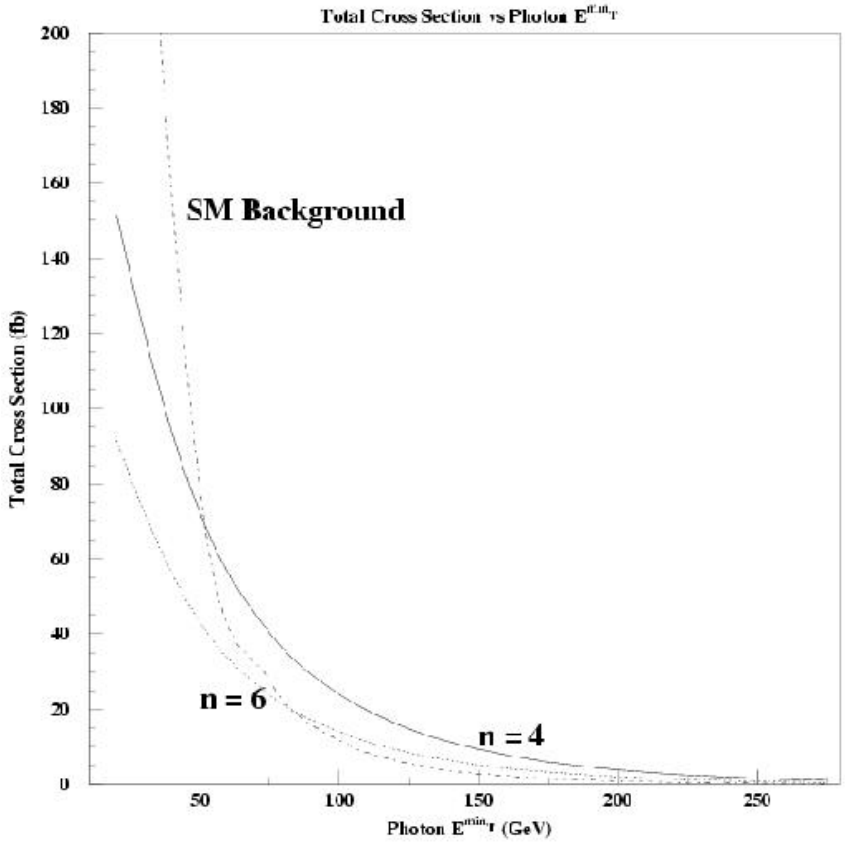

Figure 2.3: *Total $\gamma + \not{E}_T$ cross-section versus $E_{T\gamma}^{min}$ for $n = 4$, 6 and the SM background.*

'SM Background' marks the expected total standard model background for the single photon and $\not{E}_T$ signal. The other two lines labeled $n = 4, 6$ show what the Large Extra Dimensions signal would look like for 4 and 6 extra dimensions. Based on what is shown, the transverse momentum cut will be > 55 GeV/c to minimize SM background contribution and maximize LED signal/background ratio.

Gravitons couple to matter only gravitationally, but the $1/\overline{M}_P^2$ suppression present in

[7]Here, $|\eta_d|$ is the detector pseudorapidity which is defined in Section 3.1.1.

their production cross section can be compensated by the large multiplicity of the KK modes or, in other words, by the D-dimensional phase-space factor. On the other hand, the $1/\overline{M}_P^2$ suppression in the graviton decay rate into ordinary matter is not compensated by the phase space and thus its lifetime is $\tau_G \sim \overline{M}_P^2/m^3\ (\mathrm{TeV}/m) \times 10^3$ seconds with graviton mass m[17]. The $1/\overline{M}_P^2$ suppression factor can also be interpreted as the small probability that a graviton propagating in the D-dimensional space crosses the three-dimensional brane.

For experimental purposes, this means that the KK graviton behaves like a massive, non-interacting, stable particle and its collider signature is an imbalance in final state momenta and missing mass. The graviton has a continuous distribution in mass described by Equation 2.7. This mass distribution corresponds to the probability of emitting gravitons of different momenta into the extra dimensions. This is a specific feature of the graviton signal relative to any other new processes. Also, for graviton production in the perturbative regime, each extra particle in the final state is associated with an extra suppression factor, so the missing energy signal is unlikely accompanied by a variety of leptons and hadronic activity coming from the decay of heavier particles. The emission of a single graviton into the extra dimensions violates momentum conservation along the directions transverse to the brane since translational invariance in the D-dimensional space is broken by the presence of the brane. From a four-dimensional point of view, energy and momentum are conserved, but the KK gravitons can have any arbitrary mass smaller than about M_D[17]. In the ADD formalism, M_D can have any value. However, it is noteworthy to point out that the smaller the value of M_D, the larger the size of the extra dimensions and vice versa. The main purpose of this study is to set better limits from those already published for M_D in this particular channel since a discovery of LED is unlikely.

Since the graviton escapes into extra dimensions, this would result in a large missing transverse energy ($\not\!\!E_T$) signature at $D\emptyset$ along with a photon with large transverse energy E_T, so the search signature is an event with large E_T photon and high $\not\!\!E_T$. This signal contains only one irreducible physics background, which is $q\bar{q} \rightarrow Z\gamma \rightarrow \nu\bar{\nu}\gamma$. Additional backgrounds are instrumental backgrounds from photon mis-measurement, direct photon, cosmic rays, etc. All of which will be discussed in coming chapters.

CHAPTER 3

Experimental Apparatus

This chapter describes the Fermilab Tevatron $p\overline{p}$ accelerator complex and the DØ detector during its second operating period, known as Run II. Both the accelerator and the DØ detector have completed a major upgrade in preparation for an extended run that began in early March, 2001. Emphasis is placed here on these upgraded components.

3.1 Definitions and Conventions

A few definitions and conventions used in the experiment are given below. Unless otherwise specified, these definitions will be assumed for the remainder of the dissertation.

3.1.1 Coordinate Systems

A right-handed cylindrical coordinate system (r, ϕ, z) is the convention used to describe interactions occurring at DØ . The origin is taken at the nominal detector center: $(x, y, z) =$ (0, 0, 0,). The direction of the antiproton ($\overline{p}$) beam defines the polar axis (*i.e.*, the z-axis, $\theta =$ 0) with the positive y-axis pointing vertically up. In certain instances, spherical coordinates (r, ϕ, θ) are used. The angle θ defines the polar angle relative to the beam direction, and ϕ defines the azimuth about the beam direction with respect to the positive x-axis. The rapidity, y, is defined as:

$$y = \frac{1}{2} ln \left(\frac{E + p_z}{E - p_z} \right) \tag{3.1}$$

and the pseudo-rapidity, η, is defined as:

$$\eta = -ln(tan \left(\frac{\theta}{2} \right)). \tag{3.2}$$

where m is the invariant mass $m^2 = E^2 - p^2$ [1]; in the limit $m \ll E$, $\eta \approx y$. Consequently, the rapidity variable y (or η) is often used in place of the polar angle, θ, because it contains convenient transformation properties under Lorentz boost along the beam direction. Thus, the spatial vectors of detector elements are usually denoted by (r, ϕ, η).

Additionally, in $p\overline{p}$ collisions, the momenta near the beam direction of the constituents are not known since many of the collision products may escape detection down the beam pipe. As a result, another physically important quantity, which is also proportional to the "intensity" of the interactions, is the transverse momentum, p_T, of the secondary particles and is defined as the momentum vector projected onto a plane perpendicular to the beam axis. p_T is effectively conserved because particles in the beam pipe have very small p_T. Therefore, in reconstructing events it becomes convenient to use:

$$p_T = p \times sin\theta \tag{3.3}$$

and similarly, a transverse energy, E_T, whose direction is taken to be the same as the p_T vector:

$$E_T = E \times sin\theta \tag{3.4}$$

3.1.2 Luminosities and Cross Sections

Any measurement of the reaction rate is often expressed in terms of a *cross section*, σ, the interaction probability per unit flux. The particle flux is known as the *luminosity*, $\mathcal{L}$; for colliding-beam machines, it is proportional to the product of the number of particles passing through a unit area per unit time in each direction. Luminosities are typically given in units of $\mathrm{cm}^{-2}\mathrm{s}^{-1}$, whereas cross sections are often expressed in *barns*, where 1 $barn = 10^{-24}$ cm^2. The product of the luminosity and cross section subsequently yields the reaction rate, R, expressed in units of hertz:

$$R = \sigma\mathcal{L} \tag{3.5}$$

A luminosity of about 0.4×10^{31} $\mathrm{cm}^{-2}\mathrm{s}^{-1}$ is expected at the Tevatron during Run II. In the first part of the 2006 running period, an instantaneous luminosity of $15.9 \times 10^{31}\mathrm{cm}^2\mathrm{s}^{-1}$

[1] In high energy particle physics, the natural units system is used. In this system, the speed of light (c) and Planck's constant divided by 2π ($\hbar$) are set to 1, *i.e* $c = \hbar = 1$.

had been achieved [21]. Further, in order to prevent saturation[2], the rate for an experiment is often limited to a specified bandwidth and is established by event filters or triggers (See Sec. 3.4) made possible through a combination of detector and software selection algorithms characterizing a desired physics signature. Within any interval of time during which an experiment operates, the number of expected events, N, of a specific type is determined by integrating the rate with respect to time:

$$N = \sigma \int \mathcal{L} dt \tag{3.6}$$

The quantity $\int \mathcal{L} dt$ is referred to as the *integrated luminosity* ($\mathcal{L}_{int}$). A goal of 2 fb^{-1} of total $\mathcal{L}_{int}$ is expected for Run IIa, at which time additional upgrades to the accelerator and to portions of the DØ detector will extend the run to 8 fb^{-1} and beyond. This latter operating period has been classified as Run IIb. As of mid 2006, the delivered $\mathcal{L}_{int}$ stands at 1.41 fb^{-1} of which DØ has recorded 1.19 fb^{-1}.

3.2 The Tevatron

The Tevatron, is located at the Fermi National Accelerator Laboratory near Chicago, Illinois. It is currently the worlds most energetic accelerator, with a center of mass energy of 1.96 TeV. A general layout of the accelerator complex is shown in Fig. 3.1. The Tevaton serves as a storage ring in which protons and antiprotons circulate in opposite directions and are brought into collisions at two points, the B0 and D0 beam crossing areas. It is at these areas where the two main experiments at the Tevatron are located, CDF and DØ respectively. Between 1989-1996, collisions took place at a center-of-mass (CMS) energy of 1.8 TeV. The subsequent analysis of this data led to the discovery of the top-quark by the two collaborations[13, 14].

The Tevatron primarily consists of two basic components: superconducting magnets and radio frequency (RF) cavities. Protons and antiprotons complete many cycles in opposing directions around the accelerator ring, each time being appropriately bent into a circular orbit by the magnets and receiving a small boost of energy at a RF cavity. The final beams are made to interact, colliding at the two experimental areas. However, the overall process leading to collisions at each of these two points is much more complicated, requiring detailed

[2]Since data can be written to tape at a rate of less than 100 events per second and the events rate is over 10,000 events per second, a sophisticated selection is required. This is called the trigger system and it requires both hardware and software.

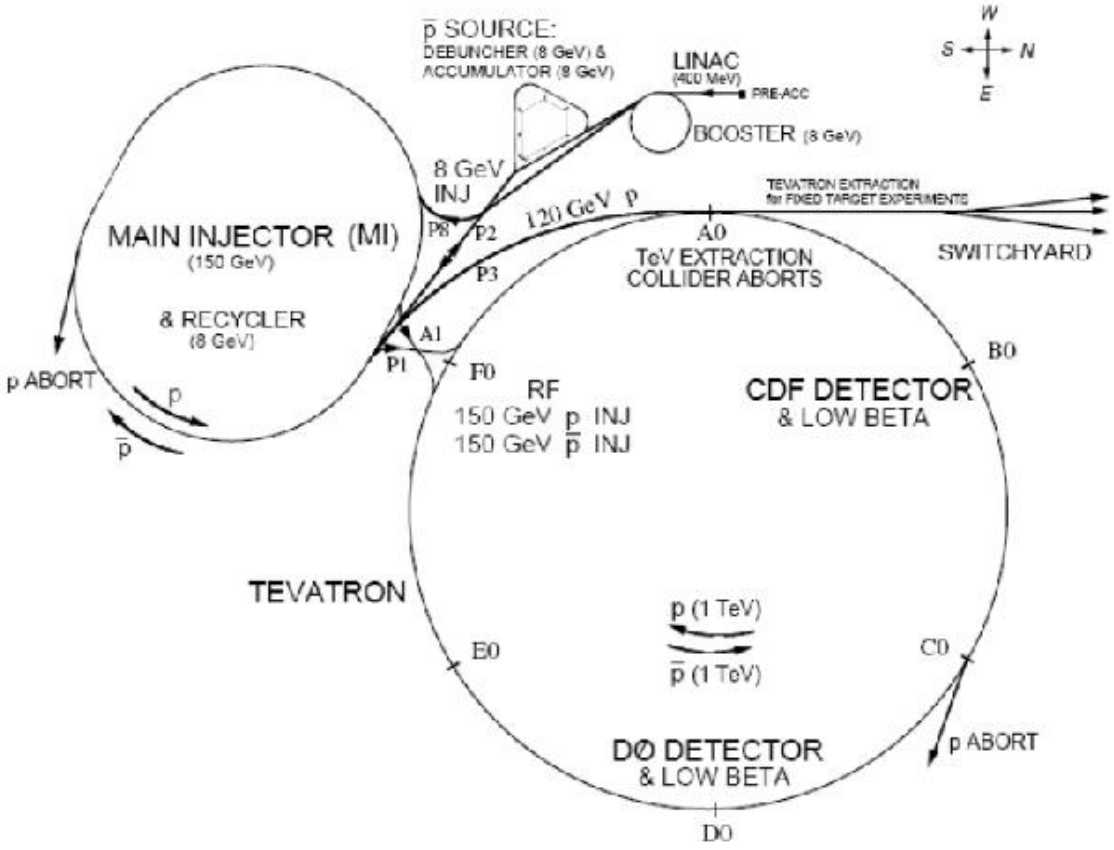

Figure 3.1: Schematic of the Run II Fermilab accelerator complex.

considerations and demanding that a number of performance specifications be met. A general outline of the collision process is given here, but the reader is directed to consult additional references ([22]) for a more technical overview. The process does require completing several accelerations stages, which can be separated into eight basic components:

- Pre-accelerator: A Cockroft-Walton
- Linear Accelerator: The Linac
- The Booster synchrotron
- The Main Injector
- The $\overline{p}$ Source: production and extraction

- The Debuncher and Accumulator
- The Recycler
- The Tevatron Ring synchrotron

All of these stages must be integrated to yield the desired beam energies and/or luminosities and thereby, provide the signals for physics studies.

The beam originates with H^- ions formed with an 'ion source' and injected into an electrostatic Cockroft-Walton accelerator. There, the H^- ions are accelerated by an electric field to 750 keV. After leaving the Cockroft-Walton, the ions are injected into the 500-foot-long Linac where oscillating electric fields boost the negative hydrogen ions to 400 MeV. The ions subsequently pass through a carbon foil, which strips both electrons from each ion, leaving only protons. The extracted protons are then steered into the Booster which is a 1570-foot circumference fast-cycling synchrotron ring. Here, the protons are constrained to a closed circular orbit by a series of bending magnets with quadrupole focusing fields that prevent the beam from diverging. At each revolution around the ring, the energy of the particles steadily increases by acceleration through a set of RF cavities. As the particle's momentum increases, the magnetic field must increase in a synchronous manner in order to confine the particles to the same orbit. The protons travel around the Booster about 20,000 times until they reach an energy of 8 GeV. A pulse train of approximately 5 to 7 bunches, each containing 5-6 $\times 10^{10}$ protons are subsequently delivered from the Booster to the next stage of acceleration: the Main Injector.

The Main Injector consists of a 120 GeV synchrotron ring, located tangentially next to the Tevatron ring at the F0 straight section (see Fig. 3.1). It was constructed for the Run II upgrade at the Fermilab facility and significantly enhances the Tevatrons collider program. In Run II, the Main Injector replaces the Main Ring, which operated during the accelerator's first running period (Run I). In general, the Main Injector has been built to perform, with improved capabilities, all the duties that were available with the Main Ring. With the removal of the Main Ring from the Tevatron enclosure, beam halos and backgrounds seen in the colliding detectors, such as DØ , during Run I are reduced. The primary function of the Main Injector is to coalesce proton bunches exiting the Booster into a single high intensity bunch of approximately 5 $\times 10^{12}$ protons. The bunch size depends largely on the nominal

performance of the Booster and the Main Injector. After reaching an energy of 150 GeV in the Main Injector, the protons are transferred to the Tevatron.

The Main Injector also extracts proton bunches at 120 GeV and allows these to impact on an external nickel/copper target for a $\overline{p}$ production cycle at a rate of once every 1.5 s. These secondary $\overline{p}$s are produced with a range of momenta and production angles and are focused through a lithium collector lens, which carries a large pulsed current (peak at 670 kA) flowing in the direction of the beam. The emerging $\overline{p}$s are collected into the first of two $\overline{p}$ storage rings.

The first ring is the Debuncher, which applies complex computer-controlled RF techniques to contract the $\overline{p}$ beam into as compact a phase space as possible (*i.e.*, a continuous band with a very narrow momentum spread). The $\overline{p}$s are further stochastically cooled in order to restrict their transverse oscillations. This is done by applying correction signals to the particles to minimize their deviation from an ideal orbit. Once a coherent beam is achieved, the 8 GeV antiprotons are transfered to the Accumulator ring where they are further cooled. In the Accumulator, stored $\overline{p}$ bunches are produced with stacking rates of up to 10^{12} antiprotons/hour. The Debuncher and Accumulator are in the same tunnel, which is roughly 520 meters in circumference. The beam from the Accumulator is transferred to the 8 GeV Recycler ring, which is located in a tunnel shared with the Main Injector.

The Recycler is a 8 GeV permanent magnet storage ring utilizing stochastic cooling systems. It is capable of delivering more antiprotons to the Tevatron, compared to Run I, and thereby, proportionally increasing the beam luminosity. The main function of the Recycler is to operate as a recovery channel, or post-Accumulator, for antiprotons left at the end of a previous collider store. The Recycler accumulates and re-cools diluted 1-6$\times 10^{11}$ antiprotons, every 0.5 to 3 hrs., up to a total stack of about 3×10^{12} antiprotons. Once the accumulated $\overline{p}$ beam reaches 8 GeV, it can be extracted into the Main Injector, where the energy of the antiprotons is raised to 150 GeV.

The 150 GeV proton-$\overline{p}$ bunch from the Main Injector are delivered in opposing directions into the Tevatron collider. Here, the final phase of acceleration is accomplished. The plan in Run II is to deliver 36×36 $p\overline{p}$ bunches with a 396 ns bunch spacing. Within the Tevatron's approximate 6.4 km circumference tunnel, superconducting magnets operating with cold compressors and upgrades to cryogenic controls, produce fields of 4 Tesla, allowing the beams to reach the maximum energy of 1 TeV each. Once accelerated to this energy, the beams

are squeezed to small transverse dimensions through the use of quadrupole magnets at the interaction points, initiating collisions at DØ and CDF. The Tevatron normally operates with an expected mean lifetime of about 72 hours between intermittent failures that frequently arise by the random loss of stores. However, this rate depends largely on the day-to-day performance of all stages and components in the collider facility.

3.3 The DØ Detector

The DØ detector is a general purpose detector, designed and constructed to study interactions originating from $p\overline{p}$ collisions at a center of mass energy of 2.0 TeV in the Tevatron collider (most of the information on the DØ detector that will be given in the following sections can be found in the Ref. [23]). The detector has been optimized to measure final states that contain electrons, photons, muons, jets and missing energy from a number of key processes occurring during these collisions. It is particularly suited for the study of high mass states and large transverse momenta, high-p_T, phenomena. Commensurate with the improvements to the Tevatron, DØ has completed a major upgrade program. The new Run II detector aims to extend the physics reach to lower-p_T final states. The detector is shown in Fig. 3.2 and consists of three main components:

- Inner Tracking System: The innermost system at DØ provides enhanced particle trajectory and tracking measurements over a broad range in pseudo-rapidity. The system is composed of four tracking sub-detectors. Immediately surrounding the Tevatron beam pipe is a Silicon Microstrip Tracker (SMT), designed to reconstruct both primary and secondary vertices. This is radially followed by a finely segmented Scintillating Fiber Tracker (CFT), which provides efficient tracking in the central pseudo-rapidity region and, jointly with the SMT, provides track reconstruction and momentum measurements for all charged particles. Both the SMT and CFT are enclosed within a central magnetic field provided by a 2.73 m-long, and 1.42 m in diameter, 2 Tesla superconducting solenoidal magnet. Directly outside of the solenoid, and within the inner bore existing in the DØ central calorimeter, a Central Preshower system aids in electron and photon identification as well as samples energy of particles traversing the solenoid coil. Similarly, a Forward Preshower (FPS), covers the forward pseudo-rapidity region.

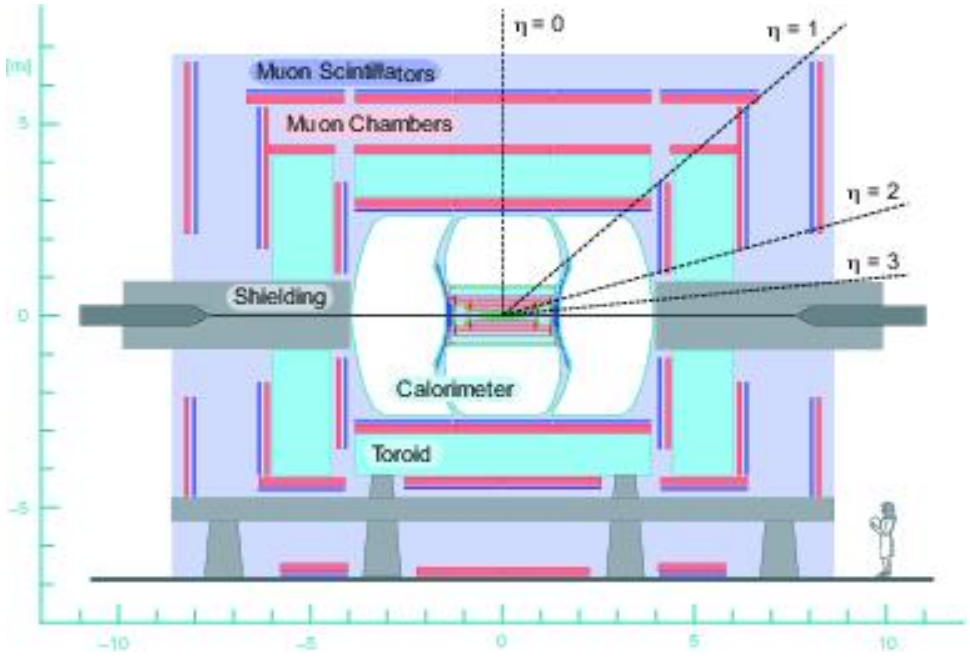

Figure 3.2: Two-dimensional view of the Run II DØ detector, showing the three integral systems outlined in the text.

- Calorimeter: Three finely segmented (*i.e.* one Central and two Forward) sampling calorimeters surround the tracking volume, providing accurate measurements of the energy of electrons, photons, and hadronic jets. Together, they enable the measurement of the total missing transverse momentum of non-interacting particles, known as missing transverse energy ($\not\!\!E_T$). Thought a measurement of the energy cluster's centroid (within any particular calorimeter cell(s)), the calorimeter provides an additional tool in determining the positions of electrons and/or photons and thereby, enhance particle identification in the DØ detector.

- The Muon System: Immediately surrounding the calorimeter, an iron toroid spectrometer combined with central (forward) proportional (mini) drift chambers and scintillation counters provide muon identification and additional muon tracking information.

Although the detector is highly compact, the full assembly is large and the hardware associated with the different subsystems is quite complex. The entire assembly approximates to about 13 m-hight $\times$ 12 m-wide $\times$ 20 m-long and weights roughly 5500 tons. The inner

tracking system alone consists of approximately 1 million channels, distributed among its individual sub-detectors. Many of these channels are read out via customized electronics located in rack spaces below the detector's support platform, see Fig. 3.2. The detector and its platform are mounted on mechanical rollers that allow the detector to move from the assembly area (*i.e.* detector construction and installation stage) to the collision hall (*i.e.* detector operation and data acquisition stage).

The following sections provide a brief overview of each of the elements in the Run II DØ detector. For a much more complete treatment, the reader is referred to the many existing write-ups, design reports, and publications on the individual systems (see Ref. [24]).

3.3.1 The Silicon Microstrip Tracker

The innermost tracking subsystem and the component closest to the Tevatron's beryllium beam pipe is the Silicon Microstrip Tracker (SMT)(see Ref. [25]), illustrated in Fig. 3.3. The primary function of the SMT is to provide precision tracking and vertex information from the interaction point (IP) in $p\overline{p}$ collisions as well as to identify and reconstruct vertices displaced from the primary interaction (Fig. 3.4). Secondary vertices are characteristic signatures of relatively long-lived decaying particles containing b and c quarks.

The tracker consists of two parts symmetric with respect to $z = 0$: the north-SMT ($z > 0$) and the south-SMT ($z < 0$). The primary vertices are distributed along z over an extended interaction region which is approximately distributed according to a Gaussian centered at $z = 0$ with $\sigma_z = 25$ cm. This defines the length of the SMT detector and motivates a hybrid design of interspersed disk and barrel modules, as shown in Fig. 3.3. In this configuration, the barrel detectors measure primarily the $r - \phi$ coordinate while the disk assemblies provide $r - z$ as well as $r - \phi$ track information. Consequently, the SMT is capable of three-dimensional track reconstruction allowing particles at small (high) values of η to be identified in the barrels (disks). Additionally, the detector must be capable of providing z-vertex and transverse impact parameter resolutions to better than 30 μm and, concurrently, be radiation hard to operate efficiently in the high luminosity environment of Run II[3].

[3]The silicon detector described here is expected to survive ~ 2 fb^{-1} and operate in Run IIa. For extended operation in Run IIb, a new layer 0 will be added next to the beam pipe. This dissertation was written during RunIIa

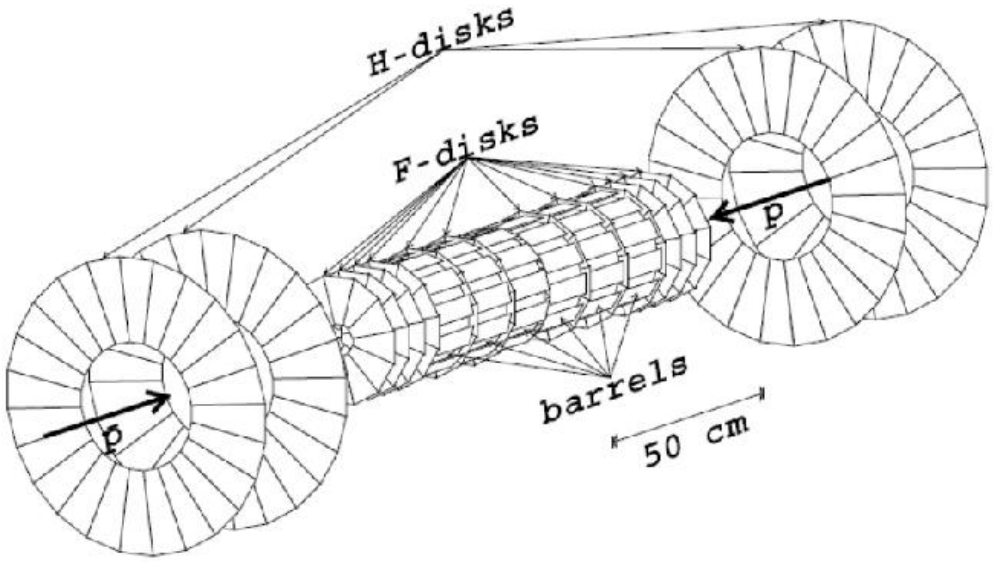

Figure 3.3: Three-dimensional view of the DØ silicon microstrip tracker.

The main volume of the SMT is formed by six barrel units 12.4 cm-long in z, consisting of four concentric layers of silicon ladder detectors each. The layers extend radially from 2.7 to 9.4 cm. A ladder consist of two 300 μm-thick wafers at 6.0 $\times$ 2.1 cm, positioned end-to-end, with electrical micro-wire bond contacts. All barrel modules have double-sided small-angle (2^o) stereo detectors in Layers 2 and 4. The central four barrels at low $|z|$ have double-sided large-angle (90^o) stereo in Layers 1 and 3. Interspersed within the barrels are twelve 8 mm-thick disks (*i.e.* six disks symmetrically located on each side of $z = 0$, known as F-Disks), each consisting of overlapping $r - \phi$ wedges to help improve tracking up to large η. The wedges of these central disks are double-sided with $\pm 15^o$ stereo strips. Additionally, in the forward region (at high $|\eta|$), four H-Disk assemblies (*i.e.* two symmetrically located on each side of $z = 0$) extend tracking about to $|\eta| = 3$. These forward disks have back-to-back single-sided wedge detectors with an effective $\pm 7.5^o$ stereo strips. Signals from the detector are read out by radiation-hard custom integrated circuits, called SVXIIe chips, which perform signal pipelining and digitization. The chips are optimized for the Run II bunch crossing intervals.

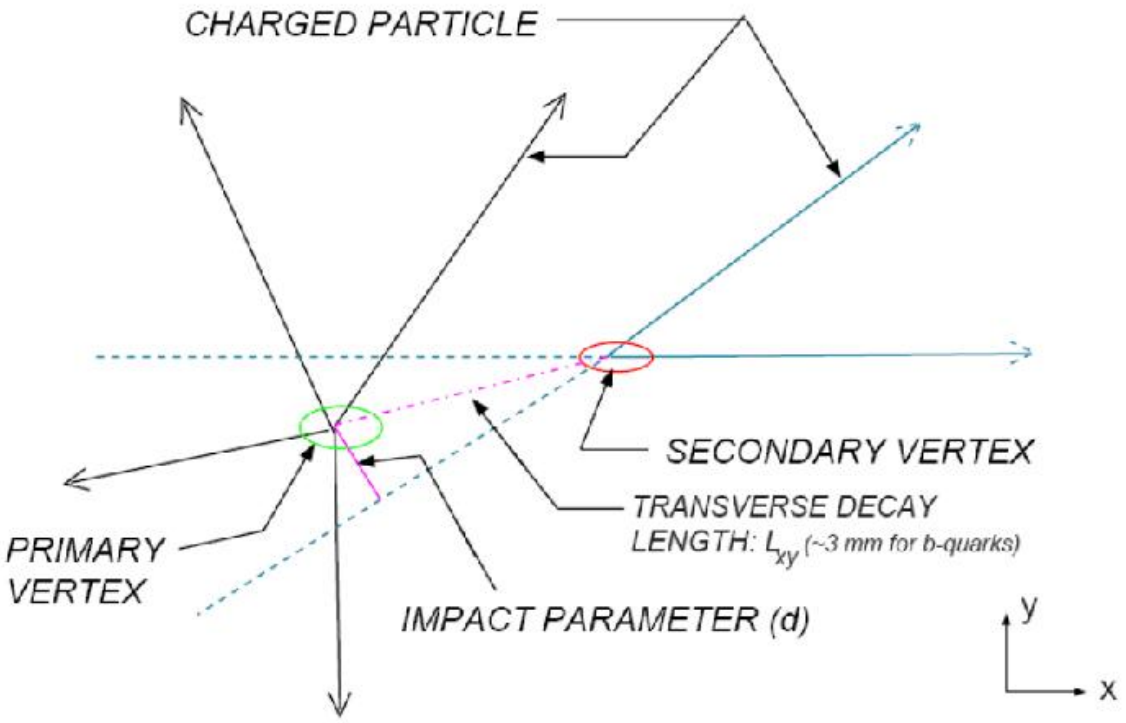

Figure 3.4: Schematic of an observed displaced vertex originating form b or c quarks in a silicon microstrip detector.

3.3.2 The Central Fiber Tracker

The Central Fiber Tracker (CFT) is the next detector that charged particles encounter as they move away from the interaction point. It surrounds the SMT [26] and it complements the SMT in track reconstruction. The CFT is enclosed within the 2 T solenoid magnet, therefore it also measures the transverse momentum of charged particles. Simulations done before Run II showed that a CFT momentum resolution, $\delta p_T/p_T \simeq 8\%$, can be obtained for normally incident electrons of relatively high-p_T ($\simeq$ 50 GeV), as shown in Fig. 3.5. Such resolutions can be of importance during E/p calibrations between the tracker and calorimeter as well as allowing CFT information to be used in situations that require charged sign determinations. Furthermore, the CFT is an integral element of the DØ trigger system which will be discussed in a later section. The signal collection time from the CFT during an interaction is within the Run II bunch crossing interval. The CFT can thus, effectively

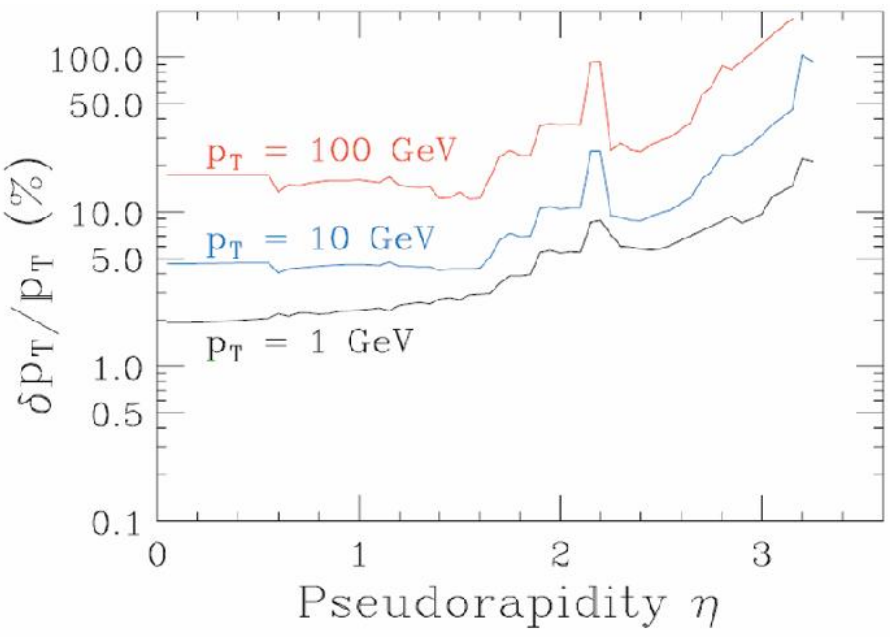

Figure 3.5: Simulation results for the momentum resolution with the Fiber Tracker as a function of pseudo-rapidity for three different p_T values.

coordinate with other subsystems to form first-level electron and muon triggers with minimal dead time. Figure 3.6 is an schematic cross section view of the CFT. The detector is made of closely packed ribbon layers of scintillation fibers mounted on eight concentric carbon-fiber support cylinders extending radially from 20 to 51 cm and providing full coverage in the central region up to $|\eta| < 1.7$. The inner two cylinders are 1.7 m long. The outer six are 2.5 m long in order to accommodate the silicon H-disk detectors at high-η. A barrel supports alternate scintillating-fiber doublet layers, these are two rows of interlocking fibers, as shown from the $r - \phi$ end-views in Figs. 3.6 and 3.7. The fist layer of doublet fibers are parallel to the beam line while the second layer is at a constant pitch of $\pm 3^o$ stereo. Each fiber is 835 μm in diameter and of Kuraray multi-clad S-type comprised of a polystyrene core doped with 1% by weight of paraterphenyl (pT) and 1500 ppm 3HF [27]. The CFT has 76,800 channels. The fibers from a ribbon are routed to optical connectors that transfer light from the scintillating fiber into 8 to 11 m-long clear fibers. The clear fibers are grouped into 256-channel light guides and transport the optical signal to highly sensitive arsenic-doped silicon avalanche photo-diodes, known as visible light photon counters (VLPC). Here, the

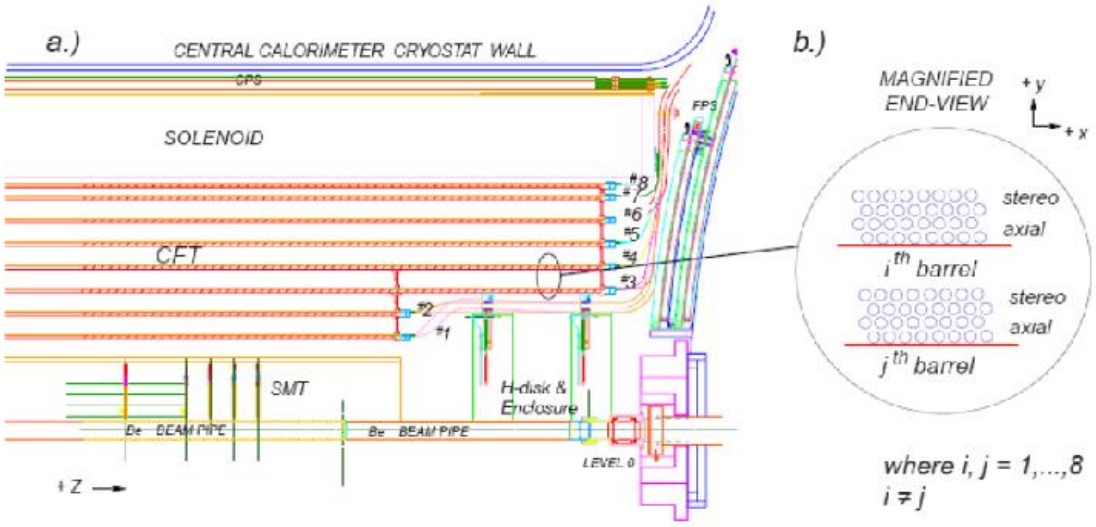

Figure 3.6: Quarter $r - z$ view of the CFT detector at DØ , Shown is a) the nested eight barrel configuration, b) a magnified $r - \phi$ end-view of the two ribbon doublet layers per barrel.

signal is converted into electrical charge and pipelined to an SVX-He chip for digitization. The front-end electronics of the VLPCs are all situated below the DØ detector, on the readout platform. Test done with the CFT read out through VLPCs and SVX-II chips have measured doublet light yields of about 14 photoelectrons for a minimum ionizing particle (MIP) traversing the detector. These responses are more ($\sim \times$ 3-4 higher) than that needed for efficient tracking[27].

3.3.3 The Preshower Detector

The preshower detector is divided onto two parts, the Central Preshower (CPS) and the Forward Preshower (FPS). Their main purpose is to enhance electron and photon identification, but it will also be used to improve the calorimeter measurements. This will be done by sampling the shower multiplicity after the material of the solenoid, tracking system and the support structure. The CPS covers an area of $|\eta| < 1.3$ and the FPS covers $1.5 < |\eta| < 2.5$. Both detectors are made of layers of triangular shaped scintillators. Wavelength shifting fibers embedded in the center of the triangles pass the signals to VLPCs, following

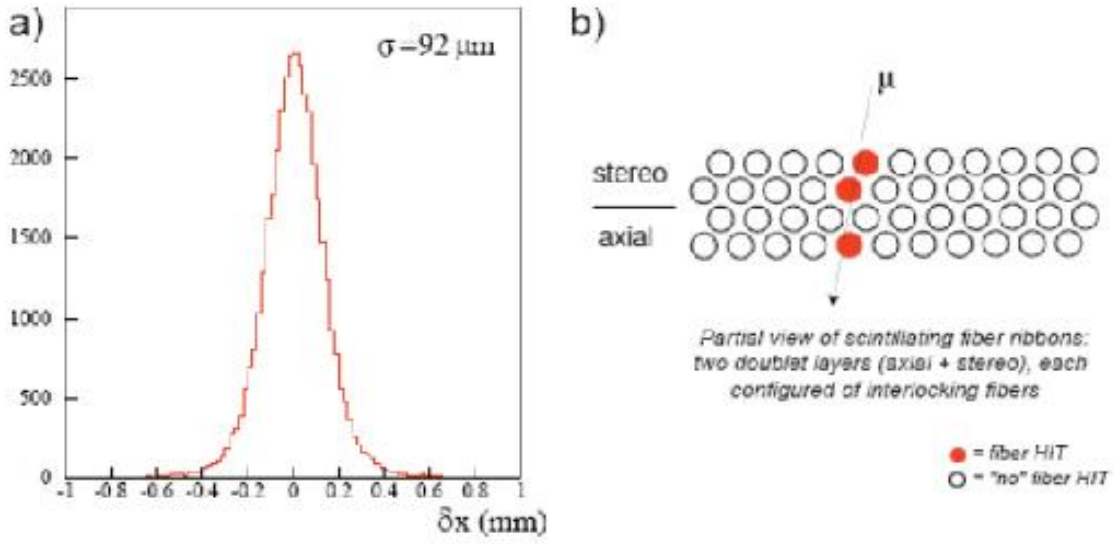

Figure 3.7: a) Distributions for the position resolution measured in the Fiber Tracker for single muons traversing an interlocking ribbon doublet configuration. The fiber ribbons are pictured in b).

the same readout chain as in the CFT. Figure 3.8 shows a cross section schematic of the PS detectors along with their coverage and structure. The CPS consists of three layers of scintillators: an inner axial layer and two layers at a stereo angle of $\pm 22.5^o$. The FPS has two stereo layers over the full coverage and an additional inner doublet layer following a 2 radiation length (X_0) lead absorber for $|\eta| > 1.65$ [28]. The the stereo layers labeled asμ and ν layers have an angle of 22.5^o. The inner layer acts as a detector for MIPs (minimum ionizing particle). Due to the triangular shape of the fibers, the distance traversed in a strip has a linear dependence to the incident position. This is convenient for the calculation of the cluster position using a charge weighted mean of the strip centers. The position resolution of a doublet (two layers are a hit) for MIP particles has been measured in a cosmic ray setup to be 550 μm [29].

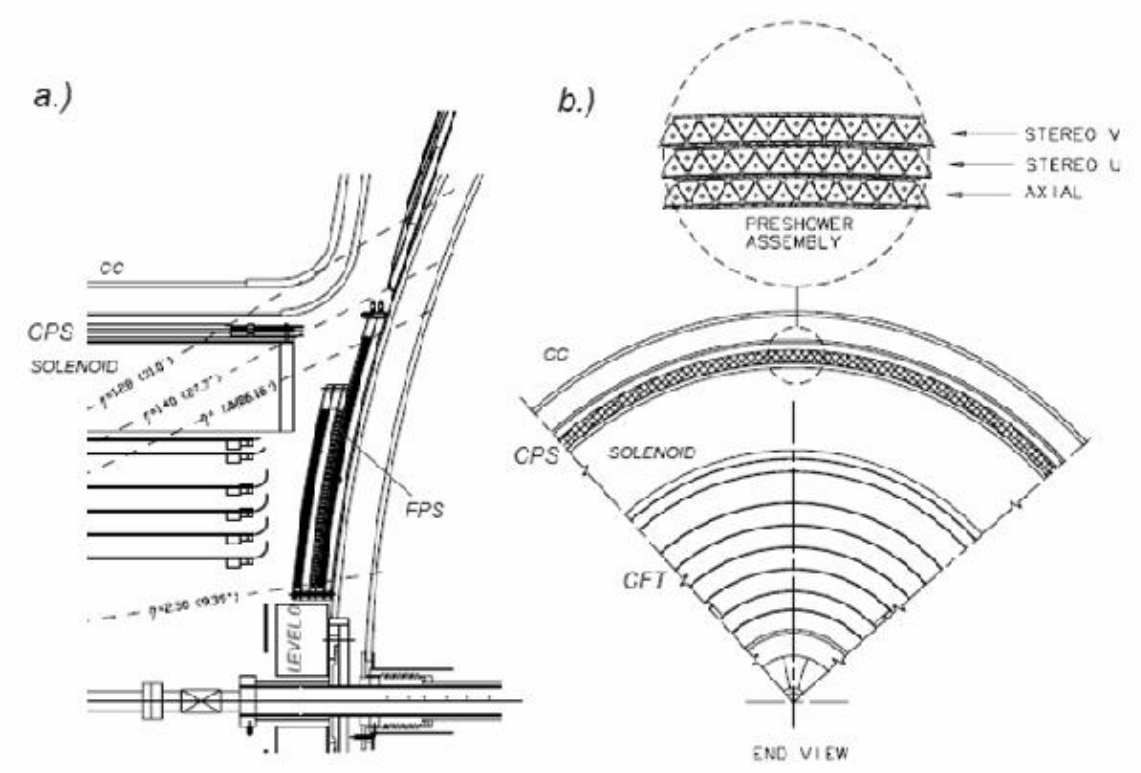

Figure 3.8: a) The location of the preshower detectors CPS and FPS with their coverage in η in $r-z$ view. b) An $r-\phi$ view of the CPS with a close-up showing the three layers of triangular shaped scintillating fibers.

3.3.4 The DØ Calorimeter

The DØ calorimeter is a sampling detector that uses liquid argon as the active medium and depleted uranium as the absorber with a thickness of 3-4 mm per layer. This thickness gives the calorimeter a total of 20 X_0 to the Electromagnetic (EM) part. It has hermetic coverage up to $|\eta| < 4$. It consists of three cryostats of nearly equal size, the central calorimeter (CC) and the two endcap calorimeter (EC). The EM part is made up of the innermost layers of the calorimeter. The following layers form the Fine Hadronic (FH) calorimeter. It is made of three layer of depleted uranium in the central cryostat and four in the endcaps. The outermost layers form the Coarse Hadronic (CH) calorimeter, which uses stainless steel and copper as the absorber. The CC has only one CH layer while there are up to three layers in the EC. Figure 3.9 depicts the layer structure of the calorimeter. The material of the

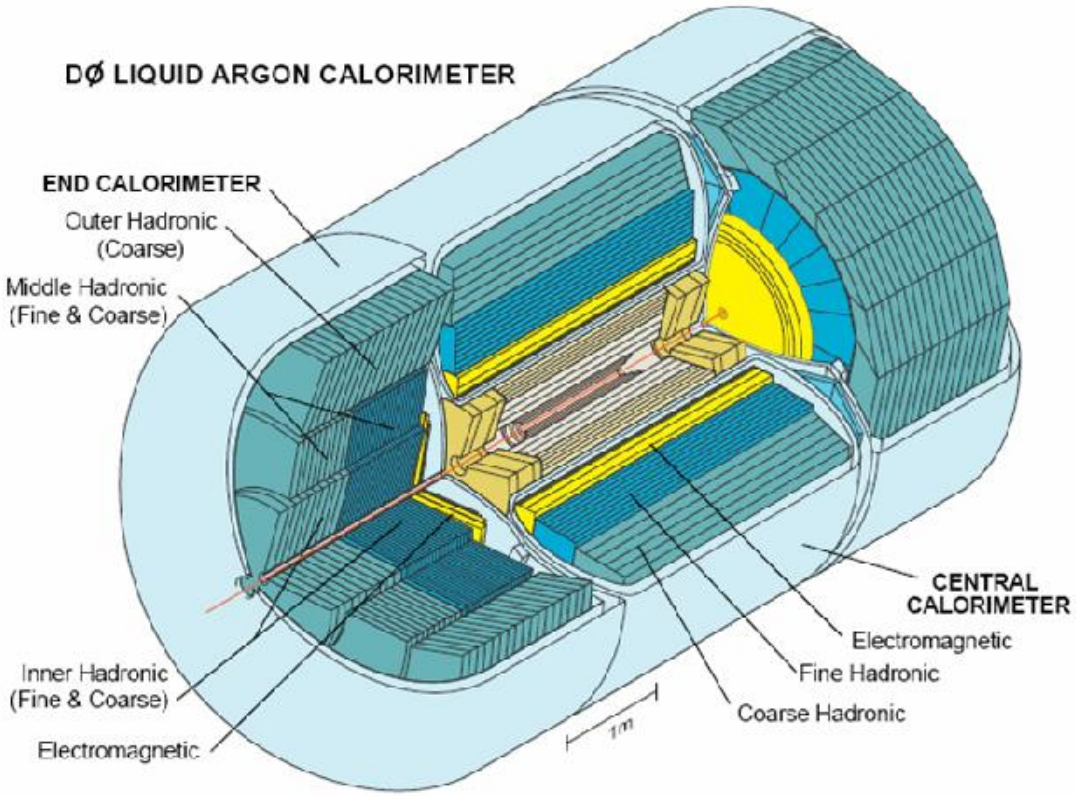

Figure 3.9: A cut-away view of the DØ calorimeter.

calorimeter corresponds to 2 nuclear interaction lengths (λ) in the FH section, and 5-7 λ for the CH part. The segmentation into single readout cells is shown in Figs. 3.10 and 3.11. The resolution that can be achieved with the calorimeter depends on the size of the cells. Most layers are segmented into readout cells of 0.1 in η and ϕ. The third EM layer has a segmentation four times as fine as the other layers (0.05×0.05 in $\eta \times \phi$) and it is located where the shower maximum for electrons and photons is expected. Cells for $|\eta| > 2.7$ have a size of 0.1×0.1 and it increases to 0.2×0.2 for all layers that $|\eta| > 3.2$.

3.3.5 The Calorimeter Readout

The main components in the calorimeter readout chain are depicted in Figure 3.12 The readout contains 55,296 calorimeter electronic channels to be read out; 47,032 correspond to

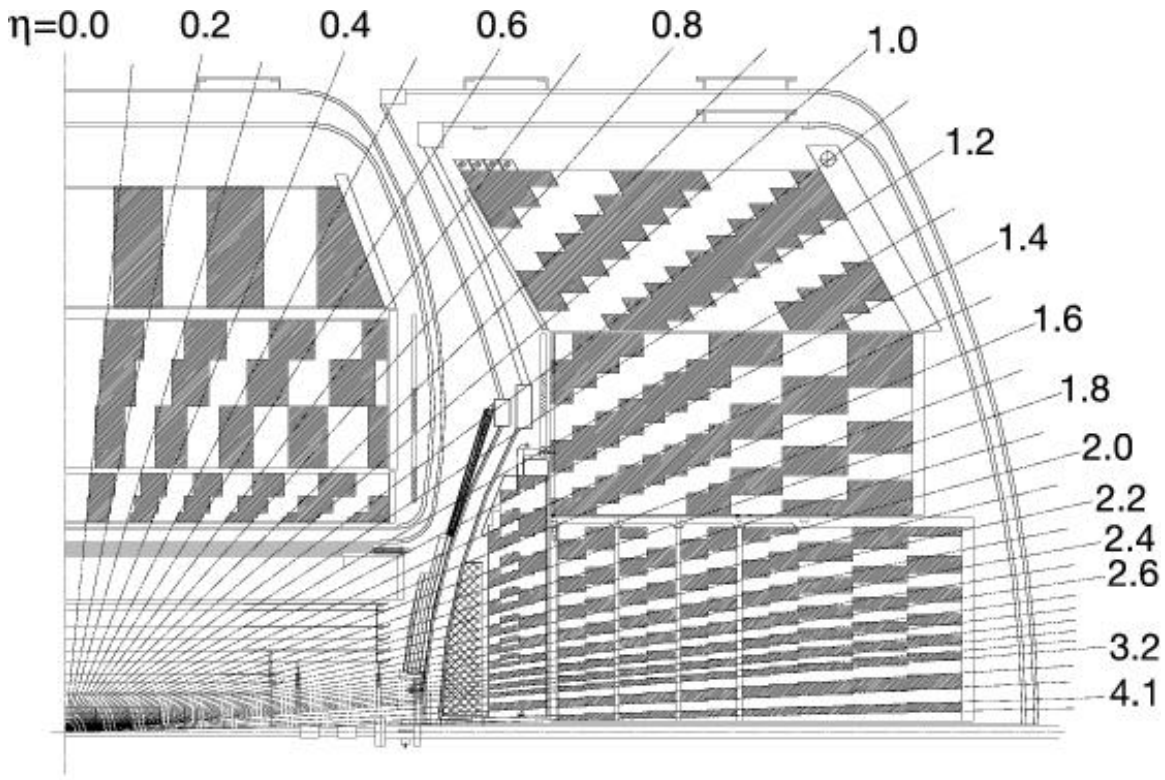

Figure 3.10: Schematic view of a portion of the DØ calorimeters showing the transverse and longitudinal segmentation pattern. The shading pattern indicates groups of cells ganged together for signal readout, called a tower readout. The rays indicate η intervals from the center of the detector.

channels connected to physical readout modules in the cryostats. The remaining electronics channels are not connected to the detector. The readout is made in three principal stages:

- First, signals from the detector are transported to charge preamplifiers located on the cryostats via low impedance coaxial cables.
- Second, signals from the preamplifiers are transported on twisted-pair cables to the analog signal shaping and storage circuits on baseline subtracter (BLS) boards.
- Finally, the precision signals from the BLSs are transmitted on an analog bus and driven by analog drivers over 130 m of twisted-pair cables to ADCs.

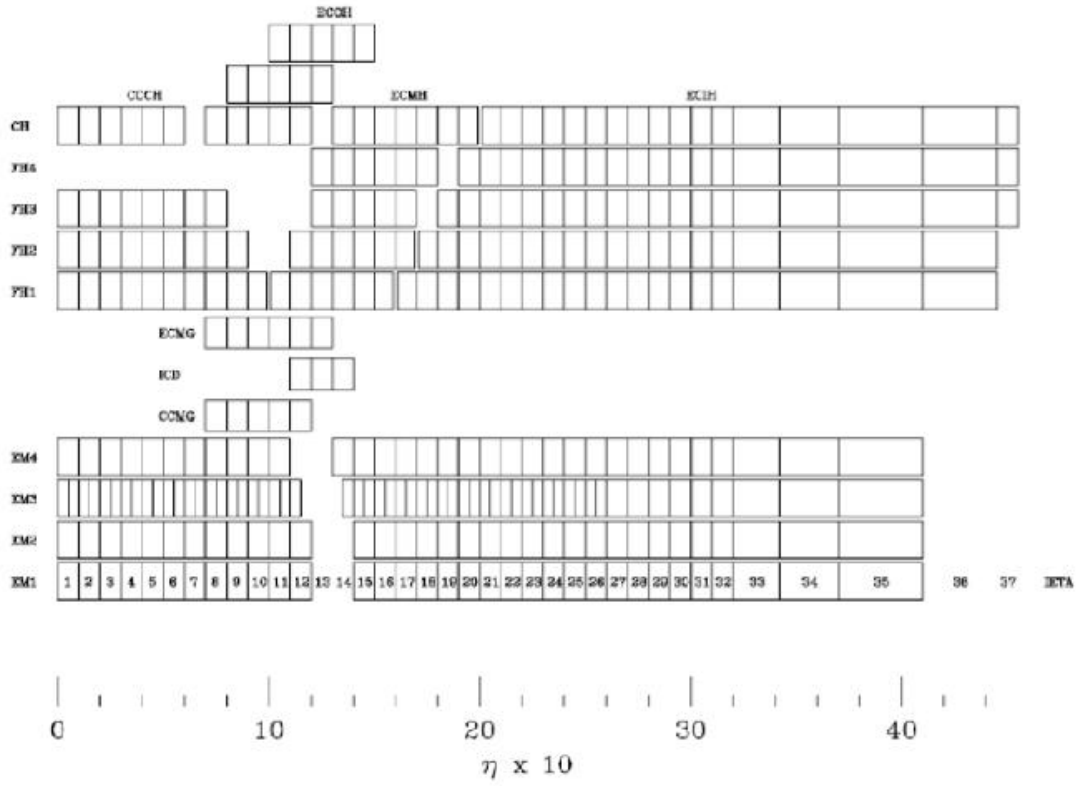

Figure 3.11: Calorimeter channel configuration in terms of depth and η.

These signals are then sent to the data acquisition system for the Level 3 trigger decision and storage to tape. The preamplifiers and BLSs are completely new for Run II, and were necessary to accommodate the significant reduction in the Tevatron's bunch spacing [27].

3.3.6 The Inter-Cryostat Detector

The regions in between the CC and EC, from $1.1 < |\eta| < 1.4$ in Figure 3.10, contain a large amount of uninstrumented material, such as the cryostat walls and support structures. This is a dead region with minimal energy sampling capability. An Inner-Cryostat Detector (ICD) is mounted on each face of an end-cryostat wall. The detector is made of scintillating tiles that measure the hadronic jet energy and allows for the sampling of particles exiting the solenoid and CC cryostats walls. The IDC is also used to calculate the missing transverse

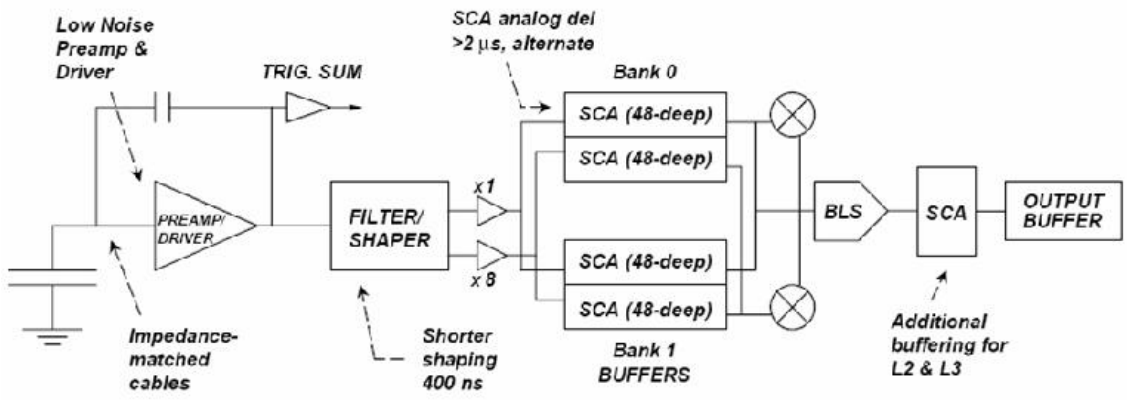

Figure 3.12: Readout chain of the calorimeter in Run II indicating the three major components: preamplifiers, baseline subtracter and storage circuitry (BLS), and the ADCs.

energy ($\not\!\!E_T$). Each ICD, north and south, is made of 16 trapezoidal-wedges[4], 22.5^o in ϕ. A groove within a scintillating tile carries a wavelength shifting (WLS) fiber, which transmits light via optical connectors to clear fibers exiting the outer edge of a tile module. These clear fiber ribbons transport the light to photomultiplier tubes (PMT) that are read out from crates mounted outside the endcap calorimeter walls. The readout electronics for the ICD is done is a similar way to the DØ calorimeter.

3.3.7 The Muon System

Muons are observable particles produced in collisions at DØ . They can penetrate several layers of matter, depositing only ionization energy in the process. Therefore, identifying a muon and measuring its momentum can be made by matching a CFT tracks with a separate tracks in the muon system. The muon detector is situated furthest from the DØ interaction region and, therefore, is the largest physical sub-detector. The following will be a brief description of the muon detector and only the major components will be highlighted. The reader is referred to [27, 30] for a thorough description. The DØ muon system is composed of the central and forward sub-detectors. Figure 3.13 depicts a cross section schematic of

[4]The solenoid magnet requires truncation of the ICD array to only 15 ϕ-wedges on the south-EC for mechanical clearance.

half of the system and Figures 3.14 and 3.15 depict the wire drift chambers and scintillators, respectively, in more detail.

The sub-detectors are separated into three detection layers, increasing radially outward and labeled A, B, and C. A-layer is separated from the B- and C-layers by a 2 T toroidal iron magnet which is divided into three magnetized regions: a central iron (CF) magnet covering the regions from $|\eta| < 1$, and two end-iron (EF) magnets covering the region from $|\eta| = 1$ to about $|\eta| = 2.5$. The magnetic field generated by the toroid causes deflections in the $r - z$ plane which is used to determine the muons trajectory and momentum. This is done by measuring how much a B- and C-layer's track bends with respect to the matching A-layer track. The resolution of the muon system is improved through a global fit of the A-layer track and a matching track in the CFT and preshowers. An associated MIP track in the calorimeter may be used for muon confirmation.

The central muon region consists of the three layers (A, B, and C) that make up the Wide Angle MUon System (WAMUS) and cosmic ray scintillation counters implemented for timing. The WAMUS includes the proportional drift tube (PDT) chambers and it covers $|\eta| < 1$ of the central region. The WAMUS PDTs, which are filled with a 80% Argon, 10% CF_4, and 10% CH_4 gas mixture, provide a coordinate determination by producing, for each hit, the:

- Drift time perpendicular to the anode sensing wire.
- Difference in the arrival time of the hit at the two ends of the sensing wire approximating the distance along the wire.
- Charge deposition on the chevron shaped vernier pads for a more accurate measurement of the distance along the wire in combination with the coarse measurements from timing.

The cosmic ray scintillating counters, known as the "Cosmic Cap", are mounted outside of the WAMUS C-layer PDTs as shown in Figure 3.15. The Cosmic Cap is extended to the underside of the DØ detector to assist in trigger and track matching with the CFT which will be discussed in Sec. 3.4. For each PDT chamber in the Cosmic Caps, eight counters, each composed of scintillators sheets with embedded WLS fibers, are read out by two 1.5 inch-diameter photo-tubes [30]. In order to find a match with the central tracking system in

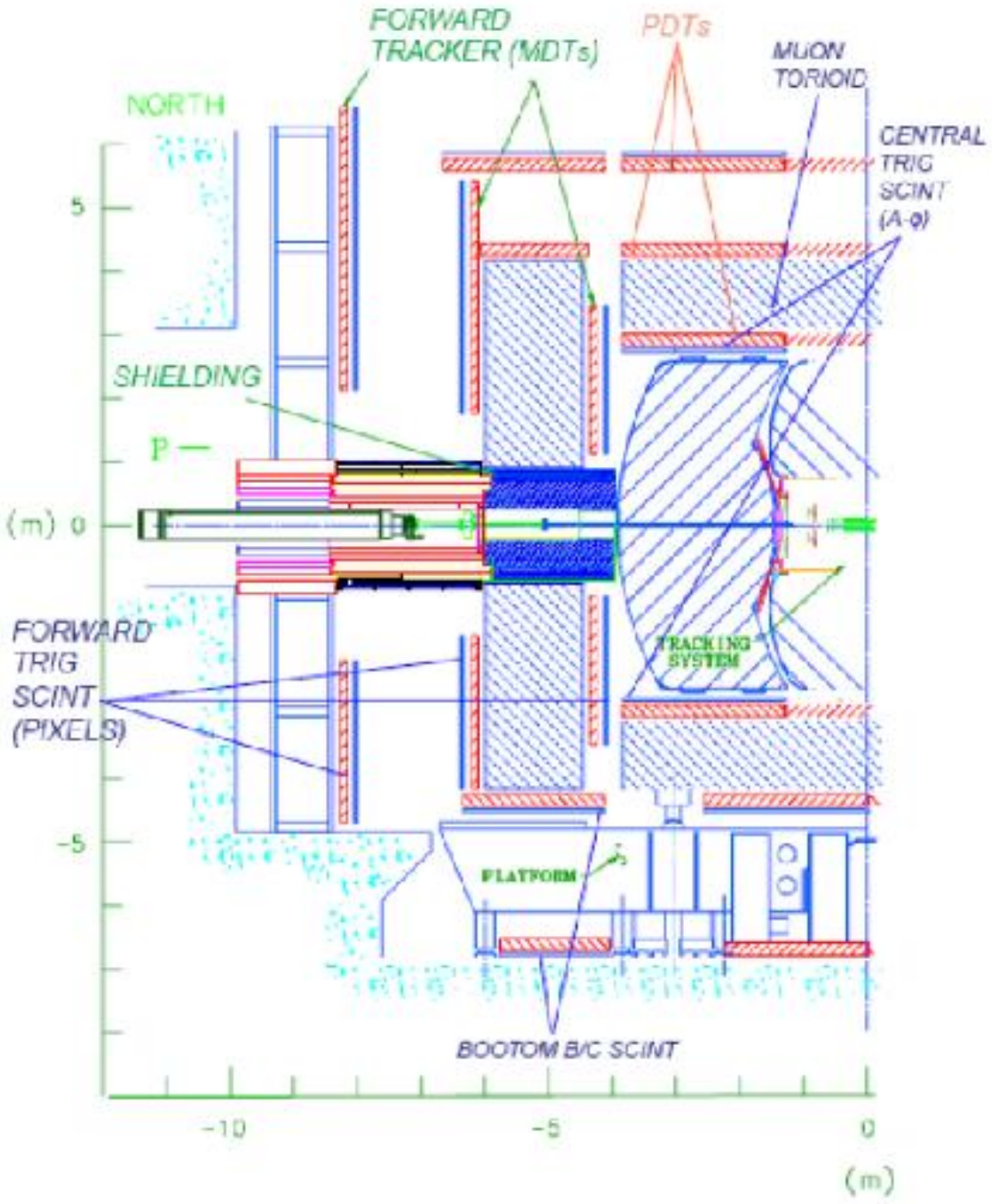

Figure 3.13: $r - z$ half-view of the Muon System. Components of both the Forward and Central systems are shown.

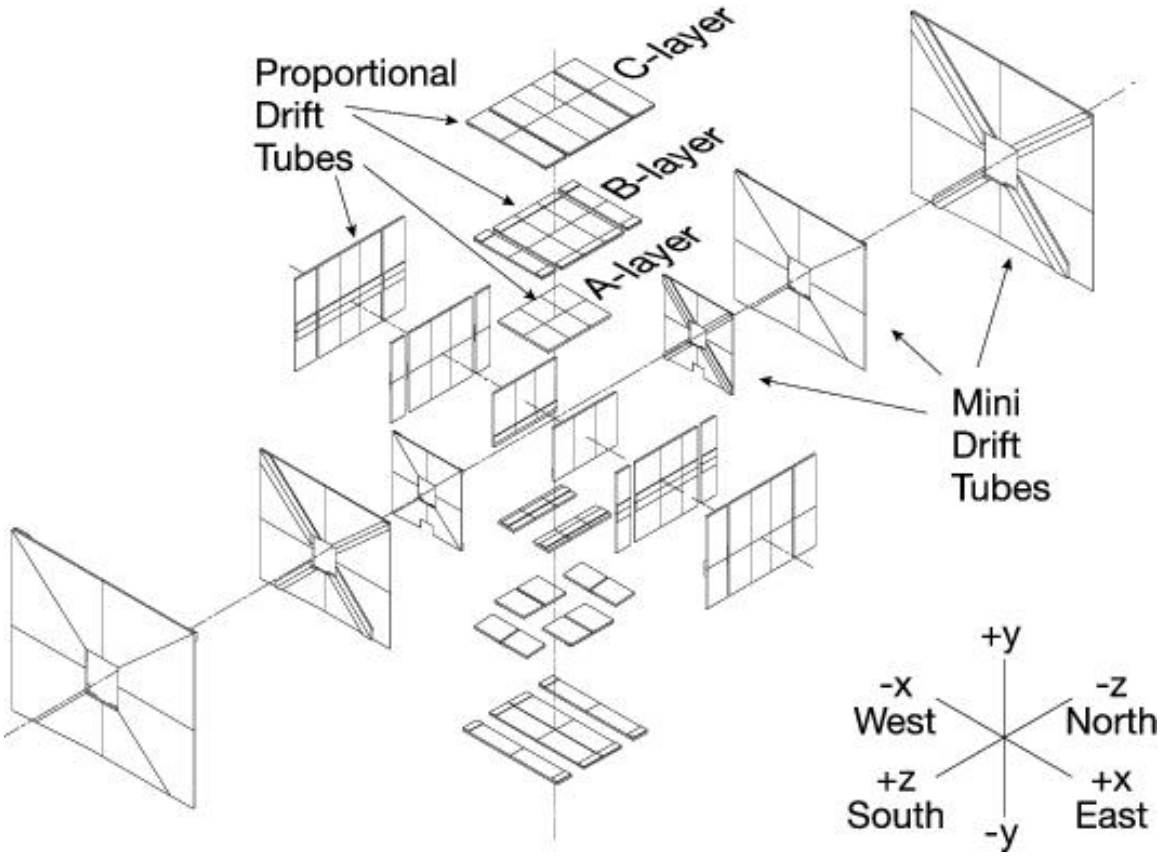

Figure 3.14: Exploded view of the muon wire chambers.

ϕ, a layer of "A-ϕ" scintillation counters are placed between the CC outer wall and WAMUS central A-layer PDT. The counters are also used to reject out-of-time backgrounds at the calorimeter's exit. The counters use scintillator and PMT technology [27, 30].

The forward muon system extends the detection coverage from $1.0 < |\eta| < 2.0$. Rather them using PDTs, the forward muon system uses Iarocci mini-drift tube chambers that are arranged in three planes, labeled A, B, and C. Each plane has 4, 3, 3, layers of tubes respectively. The tubes are oriented in a $r - \phi$ geometry and contain square 1 cm-wide (internal) cross-sectional cells, as shown in Fig. 3.16. A 50 μm anode wire is strung at the center of each cell to provide coordinate information of forward muons using drift times. There are three layers of scintillator counters, which are in a $r - \phi$ geometry, that make up the pixelation. They are segmented in $\Delta\eta \times \Delta\phi = 0.1 \times 0.0785$ and reinstalled to optimize

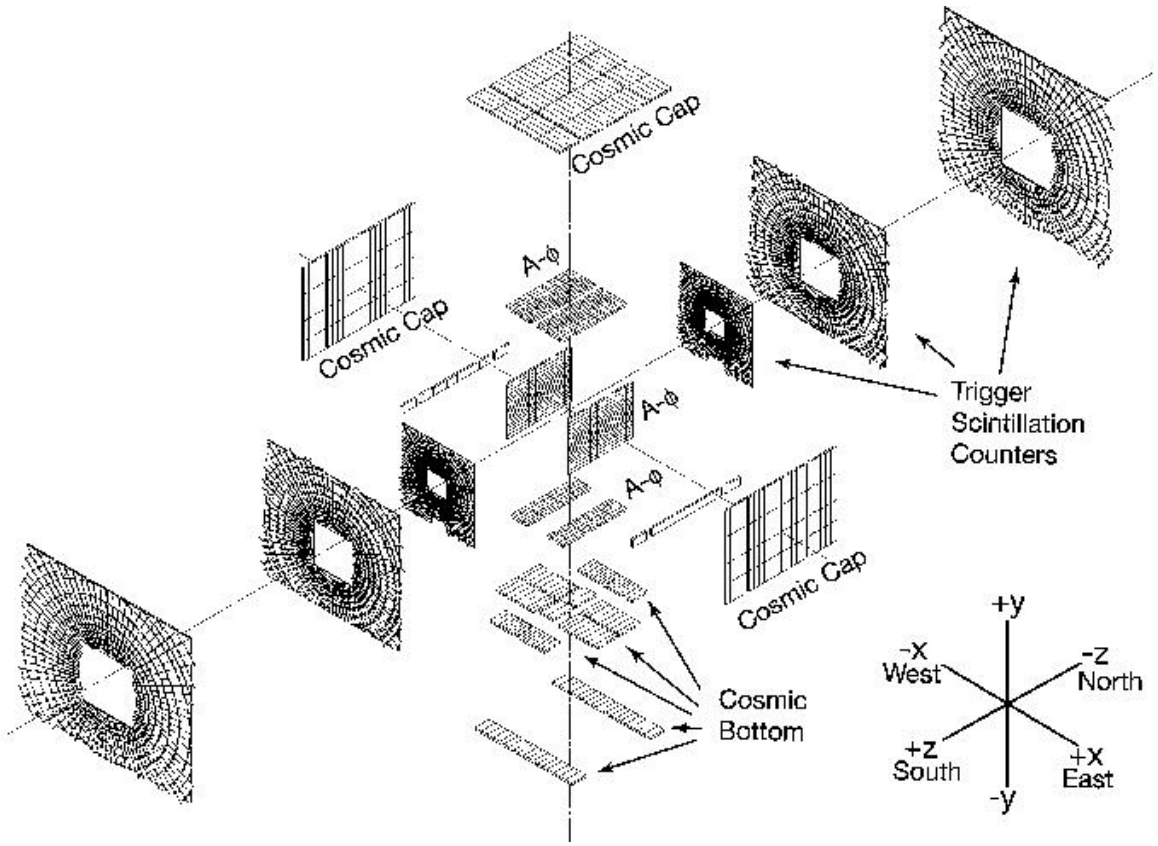

Figure 3.15: Exploded view of the muon scintillation detectors.

tracking. It is also optimized to detect low-p_T muons, $\simeq$ 3 GeV, which is characteristic of a number of physics signals. The arrangement is shown in Fig. 3.17. Each counter provides a coincident hit in all three pixel layers in conjunction with a CFT/FPS forward trigger-track match.

The muon system also contains a series of iron and polyethylene shielding, each 50 and 15 cm-thick respectively, with a lead skin, 5 cm-thick, that surround the accelerator beam pipe in the forward direction, as shown in Fig. 3.13. The shield reduces background fluxes interaction in the quads and beam pipe and from beam halo by a factor of 2 to 4 [30].

The muon momentum is measured by reconstructing the particles trajectory before and after it passes the iron toroid. The hit information in the A-layer, before the magnet, is matched to tracks in the inner tracking volume and to MIP traces in the calorimeter in order to help improve the measurements. The momentum resolution depends on the quality

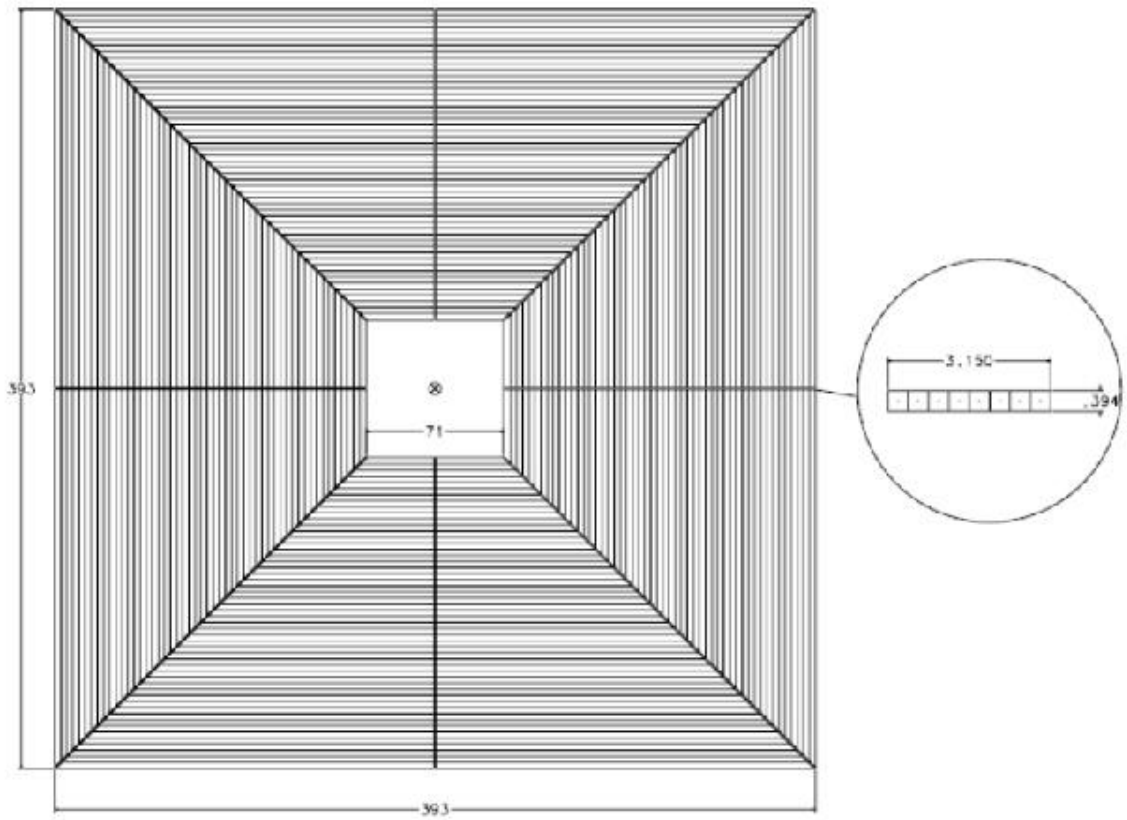

Figure 3.16: Illustration view of one $r-\phi$ plane in the muon mini-drift tube. The insert shows the cross section of a single Iarocci tube, which consists of eight 1×1 cm^2 cells.

of information available from the inner tracker as well as on the position resolution of the muon system and multiple scattering in the toroid. These latter effects limit the resolution to 18% of the momentum. In general, the resolution is parameterized in terms of the inverse momentum, $k = 1/P$, and is about [30]:

$$\sigma\left(\frac{1}{P}\right) = 0.18(P - 2GeV/c)/P^2 \oplus 0.005. \tag{3.7}$$

3.4 The DØ Trigger System

Run II requires an advance data acquisition system to cope with the high luminosity and high bunch crossing rate. The expected maximum luminosity is; $\mathcal{L} = 2 \times 10^{32}$ cm^{-2}s^{-1}. It is impossible to record every event from every crossing, so only the events that show

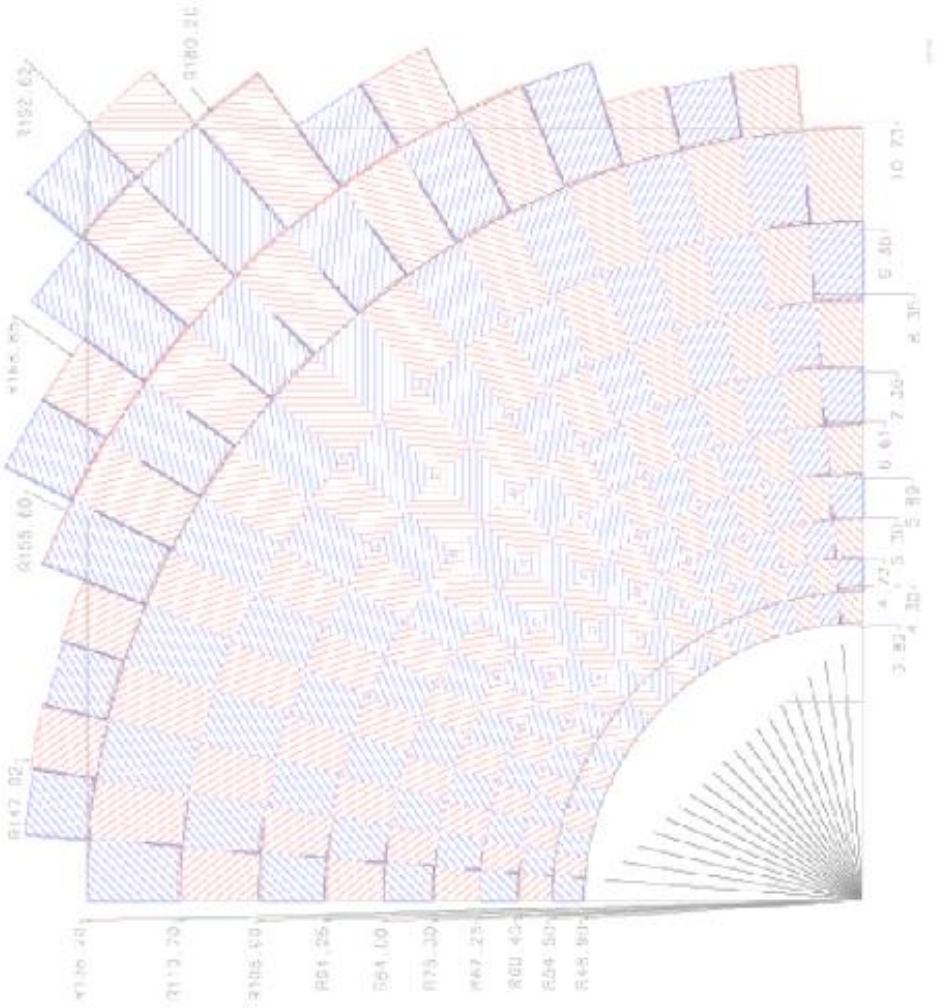

Figure 3.17: $r - \phi$ segmentation of the muon scintillator pixel counters.

signs of interesting physics are selected for storage. A trigger system has been designed and implemented to make decisions as to which events are save and which are discarded. Figure 3.18 depicts the trigger system which is implemented as a hierarchy of three selection stages referenced to simply as Level 1 (L1), Level 2 (L2), and Level 3 (L3). In levels L1 and L2, a decision is made with hardware instrumentation and simple algorithms in Field Programmable Gate Arrays (FPGAs), while L3 uses software filtering algorithms running on a set of high performance commercial processors. A Level 0 (L0) trigger is also implemented and it detects interactions from colliding beam crossings. L0 monitors the small angle

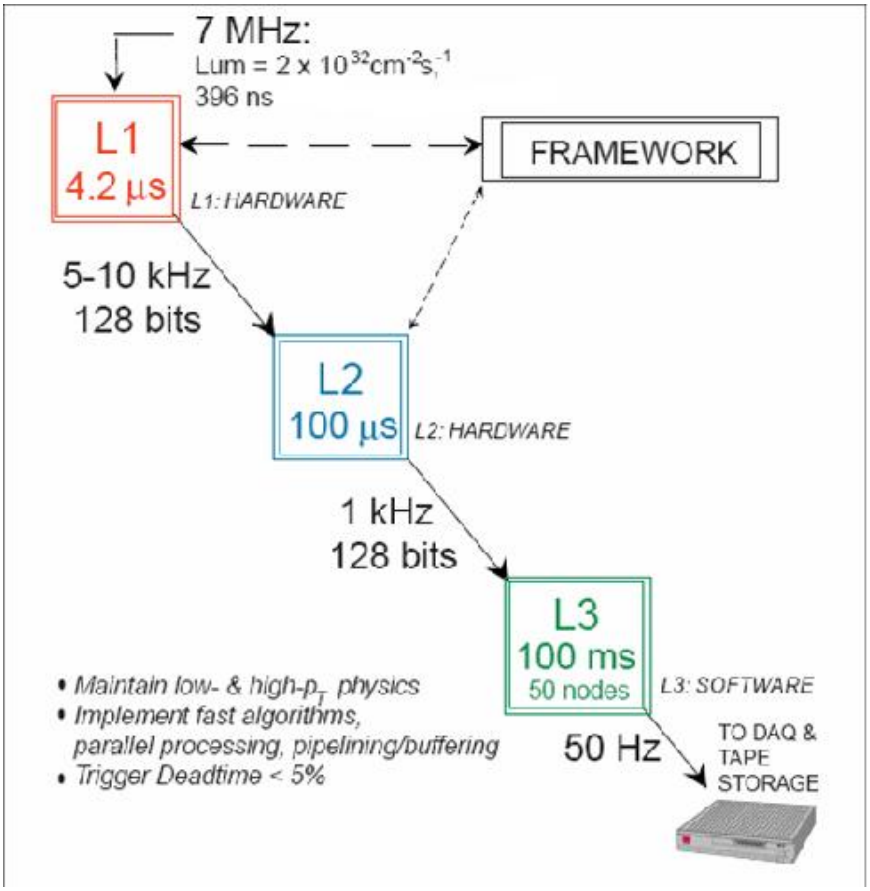

Figure 3.18: Summary of the three-level DØ Trigger System for Run II with the decision time and bandwidth allocated to each level.

inelastic collision rate that also monitors luminosity. This particular measurement is available from two Luminosity Monitor (LM) counters that are composed of plastic scintillator WLS fiber array that is read out by PMTs. The counters are mounted in between the beam pipe and the FPS detector covering an area of size $2.7 < |\eta| < 4.4$ [31]. See Figure 3.6 for L0 placement. Measurements of time-of-flight of charged particles particle incident on the LM is also used to determine the primary vertex z position for crossings containing a single $p\overline{p}$ interaction. The single trigger term is passed to L1 from LM.

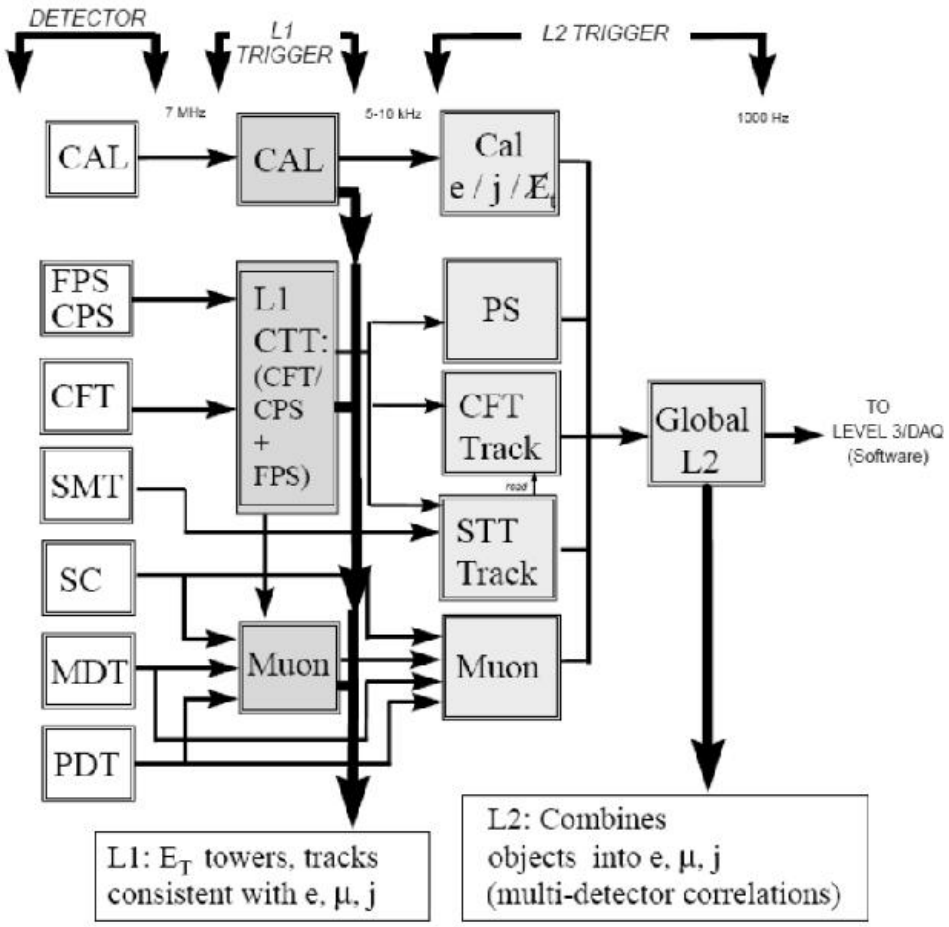

Figure 3.19: L1 and L2 trigger data pathway. The arrow indicates the direction of data flow. Multiple arrows from a particular subsystem are present for a parallel processing information thus permitting fast trigger decisions and sophisticated physics filters.

3.4.1 The Level 1 Trigger

The L1 trigger is a hardware system that compiles a list of candidate events using information from the CFT, preshower detectors, calorimeters, and muon scintillator counters. Figure 3.19 shows the information pathway for the L1 and L2 triggers. The CFT, preshowers and calorimeters provide electron identification and triggering for $|\eta| < 2.5$. Muon triggering is done by matching tracks from the CFT axial layers and muon chambers within a fiducial $|\eta| < 2.0$ volume. The L1 processors examine information from its corresponding sub-detector on the basis of trigger terms. For a $W \rightarrow e\nu$ event, for example, the detector-specific triggers

include the following:

- Trigger tower E_T above a preset threshold, total energy, and $\not\!\!E_T$ in the calorimeter.
- Hit pattern consistent with track momentum above a threshold, charge, and azimuth in the last axial layer for the CFT.
- Energy deposition above threshold, track isolation and match using the forward and central preshowers.

Each term indicates a specific condition has been met for the given event. The L1 decisions are sent to a L1 Framework (L1FW) capable of supporting 128 unique L1 triggers. The L1FW is programmed to require a specific combination of trigger terms in order to form global L1 decisions. The list of terms collected from each L1 trigger subsystem is processed through a series of FPGAs located on VME cards to determine if a specific L1 bit has been satisfied. A L1FW logical "accept" digitizes the event and the trigger is pipelined to 16 event buffers for temporary storage to reduce dead-time arising form pileup. The L1 provides a trigger decision in 3.5 μs or less with an accept rate of 5-10 kHz [27].

3.4.2 The Level 2 Trigger

The L2 trigger correlates the information from different sub-detectors as shown in Figure 3.20. It creates physics object candidates such as muons and electrons. There are two stages at L2: the preprocessor and the global processor (see Fig 3.20). At the preprocessor stage, each subsystem uses correlation algorithms to build a list of trigger objects available from the L1 trigger. Correlations include the energy of clusters in the calorimeter or the azimuth or rapidity of an electron or muon candidate in the central tracker. The time allotted for the decision making for preprocessor objects is less than 50 μs and is limited to a few hundred to a thousand bytes of information for each trigger type. The list is then fed to the global processor via a serial data highways of 128-bit wide data buses, known as "Magical bus or MBus", located on the backplane of the L2 VME crate [32]. The data is transmitted with a nominal input/output of 320 Mbytes/s in order to make a global processor decision. The total combined allotted time for both, the preprocessor and the global processor, is 75 μs. The output from the global processor is feed to a L2 Framework (L2FW) which coordinates trigger decisions to L3. The L2FW uses a similar FPGA logic as discussed for the L1FW.

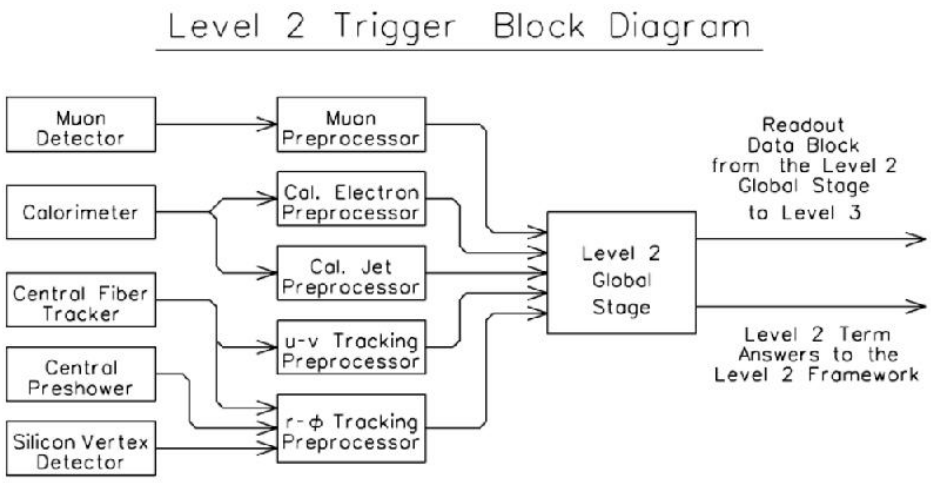

Figure 3.20: Configuration of L2 trigger components.

The overall L2 system is designed to operate with minimal dead-time ($< 1\%$), providing a rejection factor of 10. It is required to make a trigger decision in 100 μs at an accept rate of 1 kHz [27].

3.4.3 The Level 3 Trigger and the Data Acquisition System

The L3 trigger and the data acquisition (DAQ) system uses a cluster of high-performance processors operating under a joint Windows NT/Linux environment. Each processor runs event filtering software using physics tools that search for physical objects such as electrons, muons, and jet candidates. It also searches for relations between them such as event topologies or the invariant or transverse mass distribution. The system relies on a number of parallel processors in order to manage the high event rate as well as to provide a high degree of reliability. Figure 3.21 depicts the DAQ pathway. The pathway consists of a number of parallel paths that use VME buffer drivers to feed the L2 data via high-speed data cables to an Event Tag Generator (ETG) where a link is made between the lower level trigger, the DAQ, and L3 nodes. The ETG routes the data on the basis of a specific event class and assigns the data block to an available L3 processor node for single event reconstruction. Each L3 node output goes to another VBD and data cable system consisting of a host interface node that transfers the data to data-logging and monitoring cluster nodes using standard

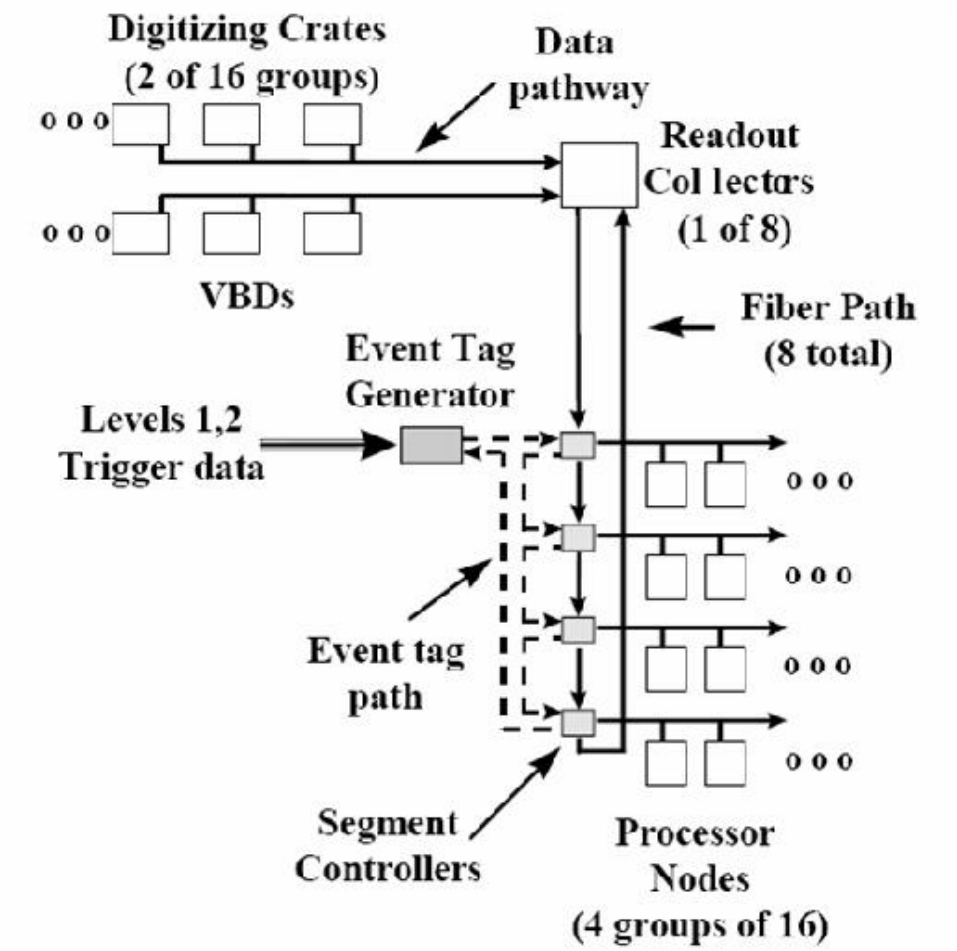

Figure 3.21: L3 trigger framework. Data flow is indicated by the direction of the arrow.

Ethernet connections. The filtered events passed by L3 are stored to tape which is accessible for offline event reconstruction and data analysis. L3 makes a decision in 100 ms with an accept rate of 50 Hz [27].

CHAPTER 4

Event Reconstruction

What follows is an overview of the software used at DØ to reconstruct physics objects from raw data. The topic of event reconstruction is a complex one and can be a lengthy one if described in detail. Therefore, only the parts relevant to the analysis in this dissertation are summarized here. However, references containing full descriptions are cited throught this chapter for the interested reader. In particular, the production version 14 of the reconstruction (DØ RECO) software is described.

4.1 Electromagnetic Object Reconstruction

The primary mechanisms that causes photons and electrons to create electromagnetic showers are e^+e^- pair production and bremsstrahlung respectively. Therefore, photons and electrons that enter the calorimeter create showers of electromagnetic particles. These showers terminate when the final particles that are produced no longer have enough energy to continue showering. The depth of the EM part of the calorimeter was designed so that almost all of the EM showers will be completely contained with in, see Section 3.3.4. Hadronic showers, however, in general will deposit energy in both, the EM and Hadronic, parts of the calorimeter with most of its energy deposited in the Hadronic part. Hadronic showers are also wider then EM showers, as shown is Figure 4.1. The latter is true unless the Hadronic shower develops early into multiple $\pi^0 \rightarrow \gamma\gamma$ which would give rise to a stronger electromagnetic signature. However, this signal would have a wider shower shape due to multiple photons.

4.1.1 Simple Cone Algorithm

Electromagnetic objects are identified by first considering quantities within the EM layers of the calorimeter, *i.e.* EM showers should be tightly clustered. The simple cone (Scone)

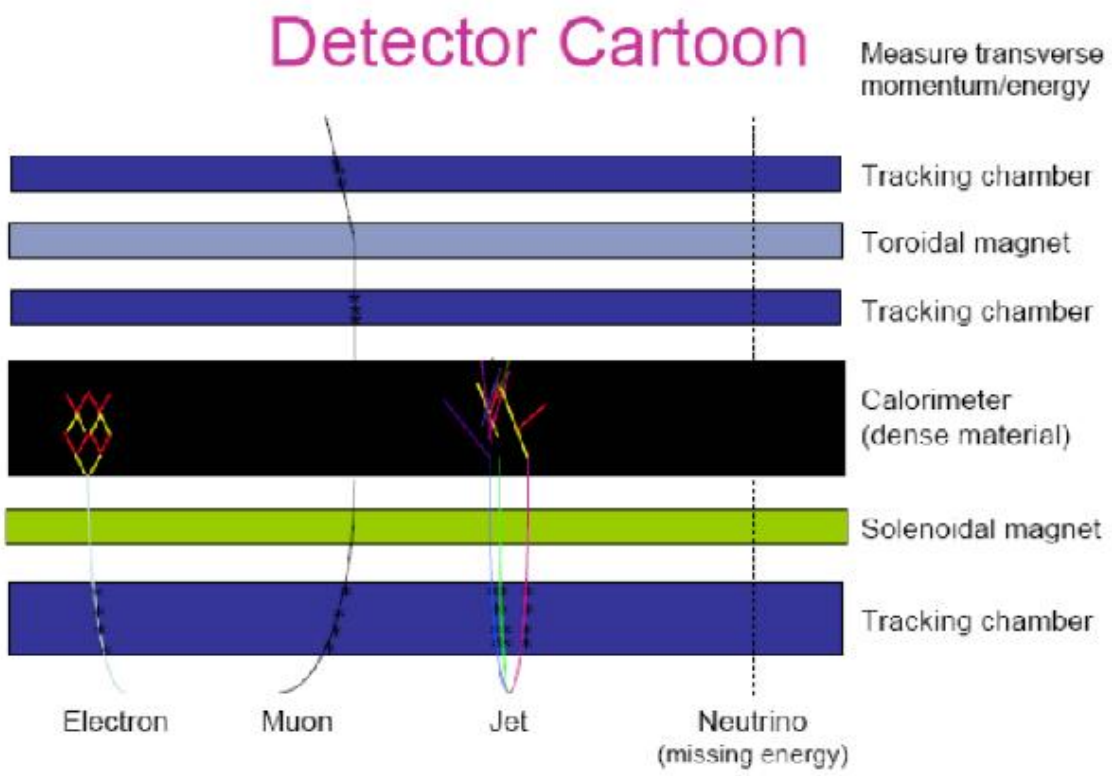

Figure 4.1: Shower shape for electrons, muons, jets and neutrinos in the Calorimeter.

algorithm receives a list of all the EM towers of non-zero energy, which are ordered in decreasing energy. Then a search of towers above the threshold of 500 MeV is done on the list. If a tower containing a cell in the Coarse Hadronic (CH) layer of the calorimeter is found, the cell's energy is discarded and the tower energy recomputed[1][34]. This was done because of noise in the CH. When a tower above threshold is identified, the Scone algorithm does the following:

- A cone is drawn of dR = 0.5 about the seed[2] tower in $\eta - \phi$ space, where:

$$dR = \sqrt{d\eta^2 + d\phi^2} \tag{4.1}$$

- Other towers within the cone are then looped over.

[1]Most of the information being presented in this section can be found in Reference [33]. However, some was found by reading the algorithms code and from the reconstruction parameters.

[2]The seed tower is the energy tower with the highest energy content.

- If another tower is found within the cone, the tower is added to the cluster and the $\eta - \phi$ position is recalculated.
- The dR = 0.4 circle is redrawn around the new position and the remaining towers are looped over.
- The process in the latter continues until all possible towers have been added.
- Completed clusters are required to have at least two good towers and a total E_T greater than 1 GeV.
- The list of 'simple cone' clusters is then sent for processing to the electromagnetic reconstruction program.

More stringent requirements are made on the new list of of EM clusters, which are:

- The minimum energy within the cluster must be 1.5 GeV.
- The ratio of energy deposited in the EM part of the calorimeter to the total cluster energy must be at least 0.9. This is called the EM fraction.
- Then a large window, 4 calorimeter towers in radius, about the highest energy tower is taken. Figure 4.2 shows an example of what a tower looks like.

Then a new list of towers is made. The total energy in the towers in the large window is first computed. Then the sum of just the EM energy deposited in a cone of $\Delta R = 0.2$ is computed. From these two energy measurements, the isolation is calculated which is define as:

$$isolation = \frac{E_{TOTAL}(0.4) - E_{EM}(0.2)}{E_{EM}(0.2)} \tag{4.2}$$

where $E_{TOTAL}(0.4)$ is the total energy, including hadronic, in a cone of radius 0.4 and E_{EM} is the total EM energy in a cone of radius 0.2. Figure 4.3 shows a graphical representation of the EM isolation. In order to tightly constrain the width of the cluster, the isolation must be small. For the candidate cluster to be selected as an electromagnetic object by the reconstruction algorithm, the isolation must be less than 0.2. This helps discriminate between clusters which are formed by hadronic showers and clusters which originate from single photons or electrons[34].

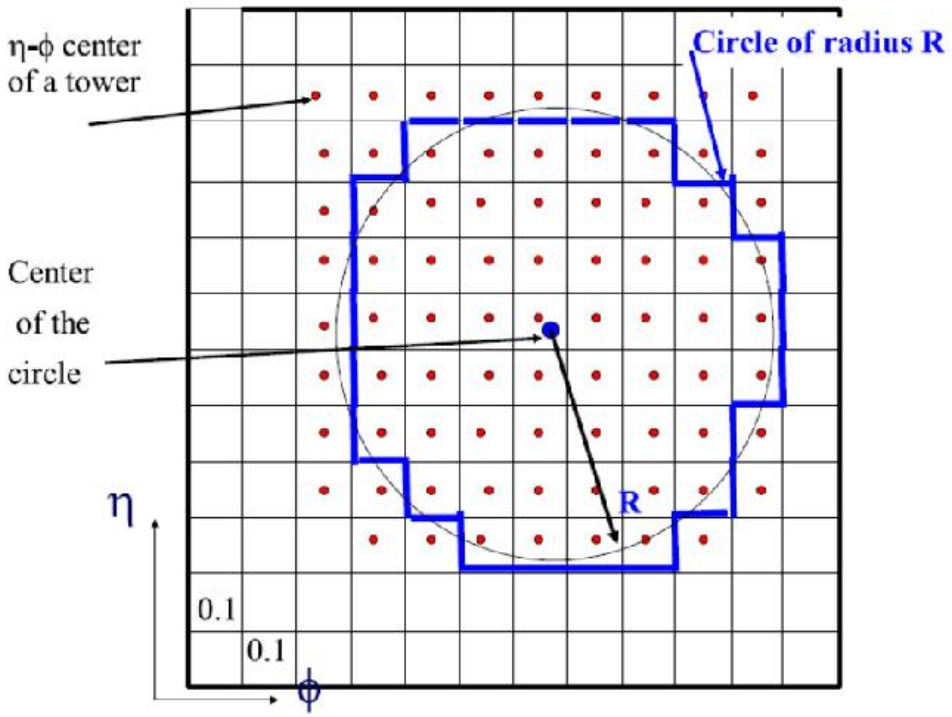

Figure 4.2: A circle of towers in $\eta - \phi$ space.

4.1.2 Electromagnetic Energy Scale

For the EM part of the calorimeter, the energy scale is refined using data from reconstructed $Z \rightarrow ee$ events, where Z is the neutral intermediate vector boson (see Section 2.1). Individual layer weights for the EM calorimeter are developed using DØ GEANT Monte Carlo events by minimizing the following χ^2 equation:

$$\chi^2 = \sum_{events} (E_{true} - \sum_{i=1}^{4} a_i L_i)^2 \tag{4.3}$$

where L_i is the energy deposited in the liquid argon in layer i, and a_i is the sampling weight for that layer. The absolute scale for the calorimeter is set using the known mass of $Z \rightarrow ee$ in data. Figure 4.4 shows the $Z \rightarrow ee$ invariant mass distribution in data events. The resolution for the EM calorimeter has been parametrized from the width and position of the peak in Figure 4.4. For the data being used in this analysis, the CPS and FPS detectors are not integrated into this energy measurement. They are used in data reconstructed in later

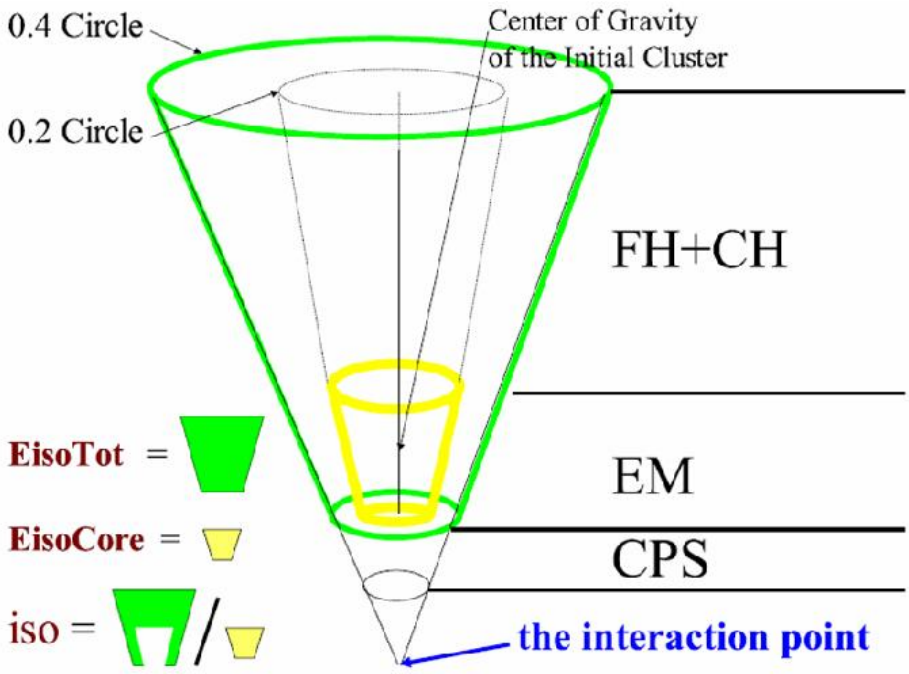

Figure 4.3: Schematic of Isolation for the Scone algorithm.

releases. The exclusion of the preshower detectors results in a larger weight for the first layer of the EM calorimeter. The weight is due to the fact that EM showers will begin earlier with respect to the first calorimeter layer because of the additional material of the tracker, solenoid, and lead of the preshower.

4.1.3 Electromagnetic Identification Quantities

The decay of mesons like the π^0, or $\pi^{\pm}$ that undergo charge exchange, can fake the calorimeter signal of electrons and photons. Several quantities are used to discriminate between signal and background. The isolation and EM fraction, as described in section 4.1.1, are two of the quantities used. Additional variables that make requirements on the shower shape also provide background discrimination. The width of an electromagnetic shower in ϕ is defined as:

$$\phi_{r\phi} = \sum_{i=0}^{N} \frac{E_i \times R^2 \times sin^2(\phi_C - \phi_i)}{E_C} \tag{4.4}$$

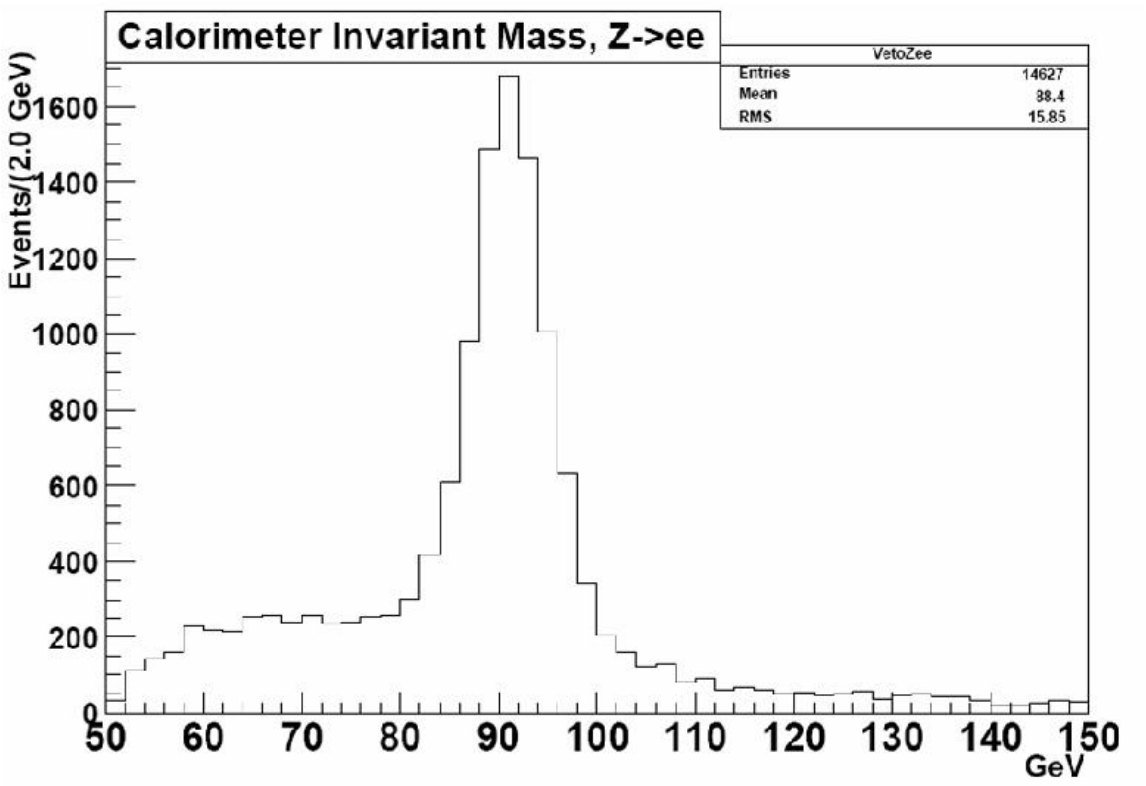

Figure 4.4: Invariant mass for $Z \rightarrow ee$ from calorimeter.

where E_C is the clusters energy, R is the clusters radius, E_i and ϕ_i are individual cell quantities. ϕ_C is the energy weight of the cluster which is defined as:

$$\phi_C = \frac{\sum_{i=0}^{N} E_i \phi_i}{\sum_{i=0}^{N} E_i} \tag{4.5}$$

where the sum is over the cells in the cluster. A similar quantity is available for the width in z. The ϕ-width is shown to be modeled well in Monte Carlo (MC) comparisons to data for electrons while the z-width is not well modeled[34].

The HMatrix χ^2 is an additional variable that is very useful. It is a discriminant variable based on the electron's shower profile in MC events. Eight variable are used to construct a covariance matrix in a large energy range. First the covariant matrix is constructed in the

following way:

$$M_{ij} = \frac{1}{N}\sum_{n=1}^{N}(x_i^n - \overline{x}_i)(x_j^n - \overline{x}_j) \tag{4.6}$$

where N is the sum over the reference MC electrons, x_i is the value of variable x, and $\overline{x}_i$ is the mean of the x_i variables. The χ^2 of the HMatrix is then constructed in the following way:

$$\chi^2_{HM} = \sum_{i,j=1}^{8}(x_i^{'} - \overline{x}_i)H_{ij}(x_j^{'} - \overline{x}_j) \tag{4.7}$$

where $x_i^{'}$ is the data value of variable x_i, $\overline{x}_i$ is the mean of the variable x_i from MC, and the matrix H is the inverse of the covariant matrix M_{ij} as defined in equation 4.6. A shower that closely resembles one of the electromagnetic showers from MC events will have a low χ^2. The eight correlated observables used for shower shape analysis are [35, 34]:

- The four energy fractions deposited in each of the layers of the EM part of the calorimeter.
- The logarithm of the total EM energy.
- The primary z vertex position distribution.
- The energy weighted transverse shower width in z and ϕ.

The HMatrix is constructed using MC electrons so it is not used for photon selection. The ϕ-width of the cluster at the third layer which is more finely segmented than the other EM layers of the calorimeter, as define in Equation 4.4, is used because it shows both, the best agreement with MC in data and the most discrimination between photons and background. Track match is a very useful variable for identifying electrons and photons. For electrons, the better the match of a single track to the electromagnetic cluster, the less likely the EM object is to have originated from a QCD jet, since jets commonly have many tracks associated with them. For photons, in contrast, isolation of the EM clusters from surrounding tracks deceases the probability that the object originated from either QCD or electrons.

There are two different χ^2 match probabilities for track matching to electrons:

- The fist one takes into account the position of a track with respect to the cluster in the calorimeter. Because no comparison is made between the momentum of the track

and the energy in the calorimeter, this method locks a substantial mis-association rate but it has a high efficiency.

- The second combines the non-gaussian energy to momentum ratio (E/p) with the spatial match of the track-cluster pair for the match χ^2. This yields a substantial lower fake rate, but is also substantially lower in efficiency due to both, bremsstrahlung photons[3], and tracker resolution.

A track isolation is constructed for photons by requiring the sum of the momentum of tracks in a "hollow cone" of dR(0.05-0.4) to be smaller than a certain threshold. This allows discrimination between jets and photons, but allows for the possibility that photon conversion might provide tracks in the center of the cone.

4.2 Jet Reconstruction

4.2.1 Run II Cone Algorithm

The cone reconstruction algorithm for jets used at DØ is similar to the simple cone algorithm described in Section 4.1.1. All electromagnetic showers share some similar characteristics, but there are several differences that need to be noted. The transverse development of an EM shower from electrons or photons, for example, scales with the Moliere Radius defined as [5]:

$$R_M = X^0 \times \frac{E_S}{E_C} \tag{4.8}$$

where χ^0 is the radiation length of the material, E_S is the energy scale, which is of order 21 MeV, and E_C is the critical energy, which depends on the atomic number of the material. About 99% of the energy in an EM shower is contained within 3.5 R_M [5]. There is no such restriction on jets, however, because the width of the shower will strongly depend on how the quarks hadronize. In order to deal with these differences, and still find stable jets, additional support in the algorithm is needed. Reference [36] contains a detailed discussion of such support.

The cone algorithm is designed to find jets that can be compared with what is predicted from theoretical models, *i.e.* reconstructed jets consisting of many constituent particles that

[3]For Bremsstrahlung photons, the energy of the cluster would be correctly measured as the photon would likely be included by the Scone algorithm. However, the momentum of the electron track would be different from the energy of the colorimeter cluster.

should possess the same energy as the initially produced quarks. The algorithm begins with a cone of radius 0.5. A list of seed towers, with minimum energy of XXX GeV, in the calorimeter is used to limit the amount of processing time spent on the reconstruction. A 'proto-jet' is created for each seed tower in the list. This is done using an iterative algorithm about the tower. If the final stable cone from this iteration is not already reconstructed, then this cluster is sent on to determine if it is part of another, larger jet, or is already too large and must be split into two jets. The 'split-merge' algorithm, as is called, is used in the case where 'proto-jets' share towers. An E_T ordered list is made of the cone jets found in the clustering, then the algorithm works down the list. If a 'proto-jet' shares no towers with any other cluster, then it becomes a jet. If the candidate does share towers with other jets, then each is considered separately. The two jets are merged if the energy shared with the lower E_T jet is greater than half the energy of the other jet. The algorithm assumes that the two 'proto-jets' are made of energy originating from a single real jet. If the energy if less than half, however, the jets are split apart with the shared cells being assigned to the nearest jet. In this case the algorithm assumes that there were initially two real jets nearby. Then the energy of the two jets is recalculated and the list of jets is remade. This is done because the E_T ordering may have changed. This process continues until no further towers are shared [36, 34].

4.2.2 Jet Energy Scale

The jet energy scale (JES) calibrates the reconstructed energy of the jets to the energy of the jets at the particle or hadron level, which is, the energy of the produced particles before they enter the detector. The subject is lengthy and complex which is beyond the scope of this dissertation. The interested reader is pointed to Reference [37] for a complete discussion the Run II JES algorithms.

Depending on the jet p_T and jet η, the JES applies a calibration factor to obtain the particle level jet energy ($E_{jet}^{particle}$) from the measured jet energy ($E_{jet}^{calorimeter}$) according to the following expression:

$$E_{jet}^{particle} = \frac{E_{jet}^{calorimeter} - E_{offset}}{R_{jet} \cdot R_{cone}} \tag{4.9}$$

where E_{offset} is the $offset\ energy$ within a jet, R_{jet} is the $jet\ response$ correction, and R_{cone} is the $out\ of\ cone\ showering$ correction. The terms in italic font are defined as:

- **Offset Energy:** Energy contributions that are not related to the physics processes that create a jet are subtracted from the measured jet energy. These contributions come from multiple interactions, underlying event energy, electronic noise, uranium noise, and pileup from previous bunch crossings.
- **Jet Response:** The energy deposited in the calorimeter is not equal to the measured energy. This is due to the fact that the calorimeter is not completely compensating, there is dead material in from of, and within the calorimeter, there are respose fluctuations between calorimeter modules, etc.
- **Out of Cone Showering:** This parameter corrects for energy losses or gains due to calorimeter showering effects from particles located inside or outside of the particle jet.

Figure 4.5 shows what the energy scale correction factors look like as a function of uncorrected jet energy and as function of η [37]. The bump in the offset energy density data comes from large weighting factors used for the inter-cryostat detector and coarse hadronic layers.

4.2.3 Jet Identification Quantities

The following quantities are used to separate real quarks and gluon jets from noise:

- **JetEMF:** The fraction of energy within the jet which is deposited in the EM part of the calorimeter.
- **JetCHF:** The fraction of energy within the jet which is deposited in the coarse hadronic layer of the calorimeter.
- **JetHOTF:** The ratio of the highest E_T cell in the jet to the second highest E_T cell in the jet.
- **Jetn90:** The number of towers which contain 90% of the jets's energy.
- **Jetf90:** The fraction of the number of towers containing 90% of the energy in the jet to the total number of towers in the jet.

Requirements are made on these variables so that the jet reconstruction algorithm will not re-find objects that were selected by the electromagnetic reconstruction. They are also used to limit the number of false jets. The latter are caused by cells with large pedestal variations, drift of pedestals, and mis-calibrations [34].

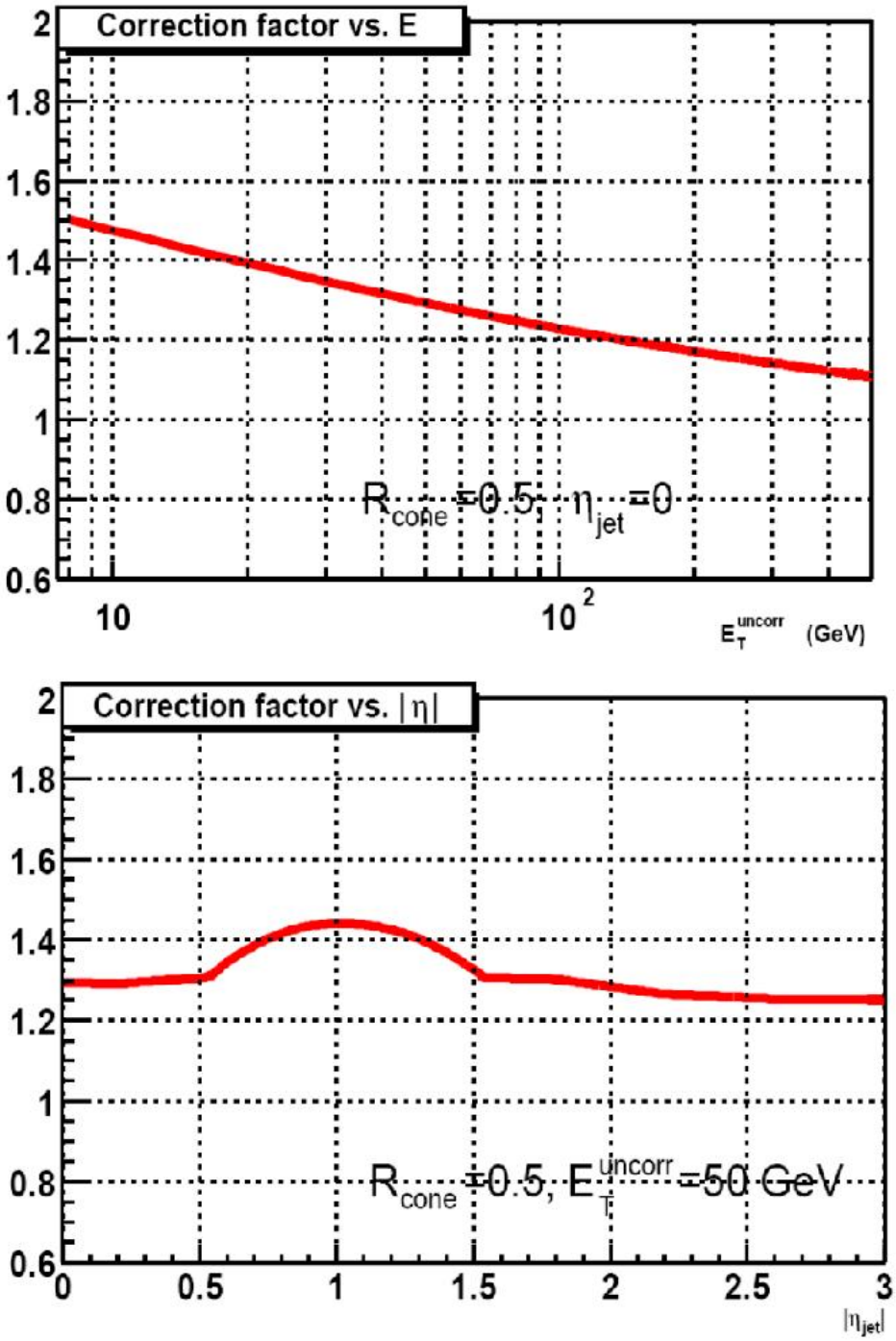

Figure 4.5: Data JES correction as a function of jet uncorrected energy (top) and pseudo-rapidity (bottom). Results are shown for $R = 0.5$ cone jet in events with one reconstructed primary vertex and T42 algorithm is applied (see [37] for T42 details). The jet η and physics η are set to the same value.

4.3 Muon Reconstruction

There are three detector components used for muon reconstruction:

- The muon system which reconstructs local muon tracks.
- The central tracker which measures the muon track parameters more precisely.
- The calorimeter where the muon deposits energy consistent with a minimum ionizing particle (MIP).

The hybrid system of proportional drift tubes and scintillators serves a dual purpose.

- To ensure the proper measurement of the position of the particle before and after the toroid.
- To ensure that the particle is 'in time' with the beam crossing. This helps to discriminate muon signals from real muon noise (descrived bellow), detector noise, or cosmic backgrounds.

Local muons are reconstructed from hits in the muon chambers. The muon reconstruction algorithms have to deal with backgrounds arising from physics processes and instrumentation. Real muon noise can originate from the scattering of protons in the beam pipe or magnets further down the particle beam, *i.e.* they are not coming from the detectors interaction region. The calorimeter is made of depleted uranium, which is decaying and giving off secondary particles that give rise to a background in the innermost chambers resulting in detector noise. Also, the ceiling of the collision hall has been exposed to beam losses from the Tevatron and has become radioactive. This results in additional detector noise in the outer chambers. The timing information from the scintillators reduces both of these backgrounds by a large fraction.

Hits in the muon system that occur within the crossing time of the beam are first associated into what are called "segments" at each layer. What follows is a brief discussion on how muon segments are formed since a full description is beyond the scope of this thesis. However, the interested reader is pointed to Reference [38] for a complete description. Muon segments are first constructed by considering hits in each plane of the wire chambers. Each hit in a proportional drift tube is effectively a circle, since the actual particle track may have

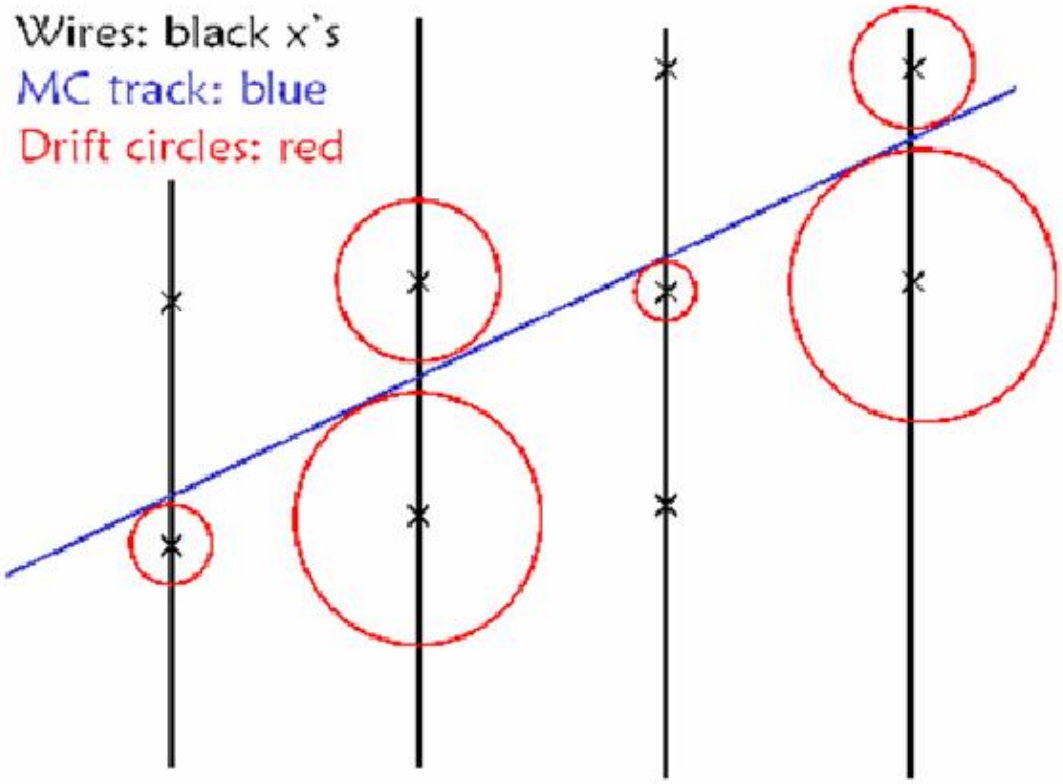

Figure 4.6: Example of Segment construction from Drift Tube Hits.

passed anywhere in the plane about the hit with the proper time. The latter is depicted in Figure 4.6. In the figure, the black lines are the wire planes and the wires are depicted by the black crosses, they are running perpendicular to the plane of the picture. The particle track is represented by the blue (diagonal) line, and the red circles are the drift circles. In reality, the equi-drift time lines of the drift tubes are not circles but look more like ovals. Each segment hit is placed on top or on the bottom of each of these circles. The hits are transformed into a local Cartesian coordinate system in which the wire direction lies along the z-axis, with the plane in which the wires are located is parallel to the y-axis. This is done so that the same algorithm can be used regardless of the orientation in the global coordinate system. At this point, the hits are grouped by wire chamber and their location on the detector is shown in Figure 3.14. Then the following criteria is used to construct local

segments from two hit connections.

- Ensure that the separation between both hits in the y-direction is not be more than 20 cm.
- The two hits must not be on the same drift circle, they must be two separate hits.
- The two hits are not on the same plane unless they come from two neighboring hits. In this case, one must be at the top of a drift circle and the other at the bottom.

Once the hit combinations have been made, the local segments are looped over and combined with other local segments to create new segments with three or more hits. Each set of hits is fitted to a line in the x-y dimensions after all possible segments are matched. The χ^2 of this fit, along with the number of hits, is used to filter down to the four best segments. Here, the better segment is the one with more hits, or if two segments have the same number of hits, the one with the smaller χ^2 is chosen. Then scintillator hits are associated with the constructed segments and a new fit is calculated. The new segments are then looped over in a list and the best matches between segments at the A-layer, and segments in the B- or C-layers are re-fitted into tracks. See Reference [39] for complete details of the muon track matching algorithms. These tracks give a measurement of the p_T of the muon.

4.3.1 Muon Track Association

The next step is to associate tracks from the CFT with the muon tracks reconstructed with the muon system. If the muon system fails to reconstructs a complete track, the CFT can also be matched to muon segments. Depending on the quality of the muon in the muon system, tracks may be associated in one of two ways.

Muon to Central Matching

The Muon-to-Central, or 'Saclay', match is done if two or more segments have been successfully fitted to a muon track. This means that the fit to segments inside and outside of the toroid has converged. Using the position, momentum, and associated errors on each, the error matrix for the measured muon track may be calculated as follows:

$$E_{6x6} = \begin{pmatrix} E_{3x3}^{PP} & E_{3x3}^{PX} \\ E_{3x3}^{XP} & E_{3x3}^{XX} \end{pmatrix}. \tag{4.10}$$

Table 4.1: Muon quality definitions for data reconstructed with production release p14.

Muon Quality	tight	medium	loose
A-layer wire hits	≥ 2	≥ 2	≥ 2
BC layer wire hits	≥ 3	≥ 2	≥ 2
A layer scintillator hits	≥ 1	≥ 1	≥ 1
BC layer scintillator hits	≥ 1	≥ 1	≥ 1
	Local track fit converged		Two of the above, A-layer conditions treated as one

Here E^{PP} is the error matrix for the momentum defined as:

$$E^{PP} =< \delta p^T(\delta p) > \tag{4.11}$$

where δp stands for the difference with respect to the mean value defined as:

$$\delta p = p - < p > . \tag{4.12}$$

The final combined muon-to-central tracker parameters and errors may be found by using the errors from the muon system track and the like errors from the CFT parameters.

Central to Muon Matching

Tracks from the CFT are propagated to the A-layer of the muon system if the muon reconstruction program fails to produce a converged fit to the track. Only tracks with momentum greater than 2 GeV are used in this propagation. All tracks within $\Delta\phi < 1$ and $\Delta\theta < 1$ are associated with the muon, but only the closest is selected as the proper track for association. Using the same method used for Muon-to-Central matching, the parameters are propagated to the A-layer of the muon system. However, beginning with the central track instead of from the muon. Here, no attempt is made to merge the local track fit from the central track, and thus the central tracker momentum is used.

4.3.2 Muon Candidates

To define muon candidates, information from all parts of muon reconstruction is used. Additionally, isolation variables are calculated using the multiplicity and transverse momenta of tracks as well as the calorimetric energy in cones around the muon's direction. There are

three muon types that are defined based upon the local muon information [40] which are shown is Table 4.1. As additional requirements, muons failing timing cuts on the scintillator hits are rejected. The time window to reject a muon candidate as a cosmic muon is ± 10 ns for A-layer scintillator hits, and -15 to 10 ns for the outer layers.

4.4 Track Reconstruction

There are two algorithms used to reconstruct tracks in the DØ detector. They are called Alternative Algorithm (AA) and Histograming Track Finder (HTF). These will be briefly discussed here but the interested reader is pointed to the listed references for a full discussion and description of both of the track reconstruction algorithms [41].

The scheme used to reconstruct tracks with the AA Tracking algorithms is as follows [42]:

- **Track Hypothesis:** Construct all possible track hypotheses by first considering as many parameters as possible. Then all of the constructed hypotheses are saved in a list called 'Pool of track hypotheses'. This pool is saved for further consideration but no decisions are made at this stage.

- **Filter:** The filter selects the final tracks from the pool of tracks. First it orders them according to a predetermine criteria. It starts the selection process form the 'best' hypothesis.

- **Final Tracks:** The filter eliminates all overlapping hypotheses and it continues through this cycle until no more tracks remain in the pool. The hypothesis is declared the AATrack if it satisfies the 'Number of Shared Hits' criteria.

This method starts from any combination of tree hits in the SMT barrels or disks. Then it extrapolates the sequence of hits to the next SMT or CFT layer, this in done by moving out-wards from the interaction region. For every track found, a χ^2, of the track fit, test is performed to ensure that the track is below a certain χ^2 value. If hits are not found, a miss is recorded. A track candidate is completed when the last layer of the CFT is fitted, or when three misses are recorded.

The HTF algorithm is based on the Hough transform mechanism and is described in full in Ref. [43]. This algorithm only uses $r - \phi$ information. A pair of $x - y$ coordinates

corresponds to a line or a region in the ρ, ϕ plane, where ρ is defined as

$$\rho = \frac{qB}{p_T}, \tag{4.13}$$

where q is the particle charge and B is magnetic field. The content of a bin of a 2D histogram in the $\rho - \phi$ plane is incremented for each pair of hits. Furthermore, the incrementation is done if the histogram contents intersect the region corresponding to a pair of hits. Bins corresponding to a track will have $n(n-1)/2$ entries, where n is the number of hits on the track. Combinations of hits from two different tracks contribute to a randomly distributed background. After the histogram is filled, cells with too few hits are discarded. If two cells share all their entries, the candidate with the lower number of entries is disregarded. The remaining cells form a track template that is subjected to Kalman[46] filtering, where the three parameters of the $r-\phi$ trajectory are fitted and the material effects are properly taken into account. Another histogram in the parameter space $z_o - C$ plane if filled in order to use the z information, where $C = \mathrm{d}r/\mathrm{d}z$. The $r - z$ measurements of the hits is used and, once again, all hits combinations are considered. Then, a Kalman filtering step removes fake templates, wrong hits and determines the track parameters accurately. This method is valid with the condition that only tracks with modest impact parameters are considered. The algorithm uses two strategies that complement each other, these are:

- To find track templates with SMT hits only and extrapolate the tracks to the CFT.
- to find tracks using CFT hits and extrapolate them into the SMT.

Finally, tracks found by both algorithms are combined.

4.5 Vertex Reconstruction

To properly calculate the transverse momentum of particles in the calorimeter and the event's $\not\!\!E_T$, the vertex position along the z-axis must be accurately reconstructed. The vertex is computed in a 'two pass' method which is described in full detail in Reference [45]. What follows is an overview.

The first pass loops over all tracks with $p_T > 0.5$ GeV in the event and it groups them in a list of candidate. The coordinates of the track parameters for each of the associated tracks are used in a fit to better determine the vertex position. The goal is to calculate the vertex

position vector, $\mathbf{x} = (\mathrm{x}, \mathrm{y}, \mathrm{z})$, by using the group of tracks, and to make a better calculation of their momentum by constraining them to this vertex. The fitting is done by using a modified Kalman Filter algorithm, similar to the ones used in earlier tracking algorithms [46], which relies on a least squares fit approach. The following variable are used for the fitting algorithm:

$$\mathbf{d}^m = \begin{pmatrix} \mathbf{m}_1 \\ \\ \mathbf{m}_2 \end{pmatrix} \tag{4.14}$$

where $\mathbf{m}_k$ is the vector of track parameters[4],

$$V = \begin{pmatrix} V_1 & 0 \\ \\ 0 & V_2 \end{pmatrix} \tag{4.15}$$

which is the covariance matrix,

$$W = \begin{pmatrix} W_1 & 0 \\ \\ 0 & W_2 \end{pmatrix} \tag{4.16}$$

which is the weight matrix where $W_i = V_i^{-1}$, and

$$\mathbf{q}^m = \begin{pmatrix} \mathbf{x} \\ \\ \mathbf{q}_1 \\ \\ \mathbf{q}_2 \end{pmatrix} \tag{4.17}$$

which is the vector of vertex parameters and momentum tracks associated with the vertex. Then the χ^2 fit is done and minimized. The χ^2 equation is constructed as follows:

$$\chi^2 = (\mathbf{d}^m - \mathbf{d}(\mathbf{q})^T W (\mathbf{d}^m - \mathbf{d}(\mathbf{q})). \tag{4.18}$$

The interested reader is pointed to Ref. [45] for full details on the minimization of equation 4.18. Candidate tracks must pass a loose selection cut of $\frac{dca}{\sigma} < 100$ [5] with respect to the detector in $x - y$ in order to be associated with the vertices. In the second pass, the requirements on the selected tracks for vertexing is tightened to $\frac{dca}{\sigma} < 3$. Here, the position of the beam spot, found in the first pass, is used.

[4] Tracks are given as a function of five parameters: z, ϕ, $\tan(\lambda)$, distance of closest approach to the origin, and the curvature, $\frac{q}{p_T}$.

[5] Here, σ is the error on the position. Also, $\frac{dca}{\sigma}$ is sometimes called the DCA significance

This two-pass method gives a clean list of candidate vertices for each event. However, some of these vertices will not point back to the vertex that caused a particular trigger to fire. Vertices from additional interactions in the crossing may also be reconstructed, this are called minimum bias (MB)[6] interactions. For every selected vertex, nearby tracks are used to compute the probability that the vertex does not come from a MB interaction. This probability is based on the assumption that tracks coming from MB interaction will have a smaller transverse momentum compared to tracks from coming from hard scatting. Finally, the vertex with the smallest MB probability is chosen as the primary vertex of the interaction.

4.6 $\not{E}_T$ Computation

The transverse momentum (p_T) at the interaction point is zero, which implies that the transverse momentum of the particles produced in an interaction must sum to zero. This is from conservation of momentum. The magnitude of the vector sum of the x and y components from the measured energy can be calculated with the following equations:

$$E_{Tx} = \sum_{i=0}^{Ncells} E_i \times cos\theta_i \tag{4.19}$$

and

$$E_{Ty} = \sum_{i=0}^{Ncells} E_i \times sin\theta_i \tag{4.20}$$

where θ is the polar angle and it is calculated with respect to the primary vertex for each cell individually. The sum includes all of the calorimeter cells above threshold, excluding the coarse hadronic section. The coarse hadronic is not used due to a distortion effect caused by noise from this region [47]. By definition, the transverse energy calculations are balanced by the missing transverse energy ($\not{E}_T$), as shown in the following equations:

$$\not{E}_{Tx} = -E_{Tx} \tag{4.21}$$

and

$$\not{E}_{Ty} = -E_{Ty}. \tag{4.22}$$

[6]For every event, hits may be required in the luminosity system, which requires there to have been at least some activity in the interaction region, without biasing the event by requiring other detector quantities. These are known as minimum bias events.

Table 4.2: Luminosity block selection cuts.

Cut	Value
$< \not\!\!E_T >$	< 4 GeV
$\mathrm{RMS}_{\not\!\!E_T}$	< 22 GeV
Scalar E_T	> 80 GeV
Events	> 500 GeV

The $\not\!\!E_T$ is calculated with:

$$\not\!\!E_T = \sqrt{\not\!\!E_T{}_x^2 + \not\!\!E_T{}_y^2}. \tag{4.23}$$

Due to momentum errors from the various detector components, the missing energy is rarely zero. However, most events that do not include non-interacting particles have a small quantity of $\not\!\!E_T$. The $\not\!\!E_T$ is computed by first considering the energy depositions in the calorimeter on a cell by cell basis, with respect to the primary vertex. The momentum of any muons that are matched to central tracks is subtracted from the $\not\!\!E_T$ calculation, giving the final quantity used in analysis.

The $\not\!\!E_T$ distribution in minimum bias events is used as a check on the functionality of the calorimeter. If the distribution in a given run shows an excess of high $\not\!\!E_T$ events, this may be an indication that either the calorimeter is not correctly reading out, or some problem in the electronics is present. Problems such as a 'hot' cell, or a 'warm region' that would indicate pedestal drift. These problems are assessed on a 'luminosity block' [7] basis. If the distribution is shifted, or widened by an increase of high $\not\!\!E_T$ events, then the block will be marked bad and the integrated luminosity from that data is excluded from analysis[34]. Table 4.2 summarizes the cuts used for marking a luminosity block bad. These cuts eliminate approximately 5% of recorded luminosity.

[7] A luminosity block is a unit of time used by the luminosity system to measure the number of interactions that have occurred. It corresponds to approximately one minute of data taking. Since luminosity blocks are used to calculate the integrated luminosity, they correspond to the smallest amount of data one may exclude and still have a sample that may be properly normalized.

CHAPTER 5

The Analysis

This chapter describes the data selection and analysis for the search for large extra dimensions (LED). It details the data set used and the requirements imposed in order to obtain as pure a sample as possible of events containing a single photon and a large imbalance in transverse energy.

5.1 Data and Event Selection

For this analysis, the data used was collected by the DØ detector in the 2002-2003 running period (runs 152148-180956). We used the sample containing one electromagnetic (EM) object of loose[1] quality selected by the DØ Common Sample group (CS) [49]. This data skim is called 1EMloose by the CS group. To avoid unnecessary reduction in statistics, only runs marked as 'bad' by the calorimeter group have been excluded.

5.1.1 The Triggers

The triggering at DØ is a multi-stage system as described in Section 3.4. Trigger selection was done with two unprescaled single EM object triggers. The trigger definitions are as follows:

- **E1_SH30:** This trigger is from trigger list v12. At L1, it requires one calorimeter EM object with $p_T > 11$ GeV/c and NOT Calorimeter unsuppressed readout. At L3, it requires one electron, or photon, with loose shower shape requirements with $p_T > 30$ GeV/c. The luminosity collected with this trigger is 44 pb^{-1}.

[1] A loose EM object is one that passes the selection criteria listed in Sect. 4.1.3

- **EM_MX:** This trigger is from trigger lists v8-11. At L1, it requires NOT Cal unsuppressed readout and one EM trigger tower having $p_T > 15$ GeV/c. At L3, it sets the trigger bit true if an EM object with $|\eta| < 3$ and with $p_T > 30$ GeV/c meeting loose criteria is found. The luminosity collected with this trigger is 153 pb^{-1}.

The data collected with the mentioned triggers sums to 197 $\pm$ 13 pb^{-1}, as computed by the DØ Luminosity group. Both triggers have been measured to be fully efficient for EM objects in the central region for $p_T > 40$ GeV/c [48]. The above sample is processed by the application of the photon event selection criteria to the 1EMloose skim.

5.1.2 Event Selection Requirements

The goal of the event selection requirements is to select as many signal events as possible while rejecting as much background as possible. The 1EMloose sample is enormous and has about 10×10^6 events. To focus on extra dimensions, we required the events to have 2 or less jets, and $\not\!\!E_T > 12.5$ GeV. With this requirements, the data set was reduced to 807,118 events. The thumbnail[2] root-trees[3] were made with d0correct version 6[4].

First we applied the DØ standard photon ID requirements as described is Section 4.1.3. These are:

- In CC: Events must be in the central region of the calorimeter, *i.e.* $|\eta| < 1.1$.
- No additional jets: Make sure that the event does not have any additional jets other than the photon.
- Scone algorithm: Make sure that the photon candidate passes the simple cone algorithm with $R = 0.5$.
- EM object type 10 and 11: The difference between types 10 and 11 is a track match, which is applied to type 11. This is a loose track match, meaning that a track is projected to be near the EM candidate.

[2] A thumbnail is the format in which the data is arranged after reconstruction by the DØ Reco program, *i.e.* this is the Reco output format.

[3] Root-trees, or TMBTrees, is the format in which analysis is done.

[4] The d0correct algorithm is a program that applies correction factors to the thumbnails while making root-trees.

- EM Fraction > 0.90: Make sure that at least 90% of the energy has been deposited in the EM part of the calorimeter.

- EM Isolation < 0.15: Make sure that the EM energy tower is isolated from other towers, as described in Section 4.1.1.

- EM candidate is in fiducial: Make sure that the EM object is within the $\eta - \phi$ fiducial to avoid cracks in the detector.

- Track match requirement: Make sure that the probability that a track is matched to the EM object is less then 0.001. That cut ensures that the object is not an electron.

- Shower shape requirement: To discriminate between real photons and energy depositions in the EMCal that fake photons, the variable HMx7, as described in Reference [51] and presented in Section 4.1.3, was used. The cut is HMx7 < 15.

The efficiency of the above requirements was measured for all the requirements together, rather than individually (see Section 22).

To further reduce backgrounds and to get rid of events that should not be part of the single photon and $\not\!\!E_T$ data, such as events with muons, the following additional requirements were made:

- $p_T^\gamma \geq 55$ GeV/c: This cut is used because this value maximizes the signal to background ratio, see Section 2.3 and Figure 2.3.

- Muon veto: Events with reconstructed muons of any quality, as described in Section 4.3, are rejected.

- Isolated tracks veto: An isolated track is defined as any track with $p_T > 10$ GeV/c, p_T sum of tracks in $dR < 0.4$ (see Equation 4.1 for dR definition) about the candidate track to be < 2 GeV, and $dz_{dca} < 1.0$ cm [5].

- $\not\!\!E_T > 45$ GeV: This cut is used to minimize the QCD and electroweak background contribution.

[5] dz_{dca} is the distance of closest approach to the z coordinate of the primary vertex.

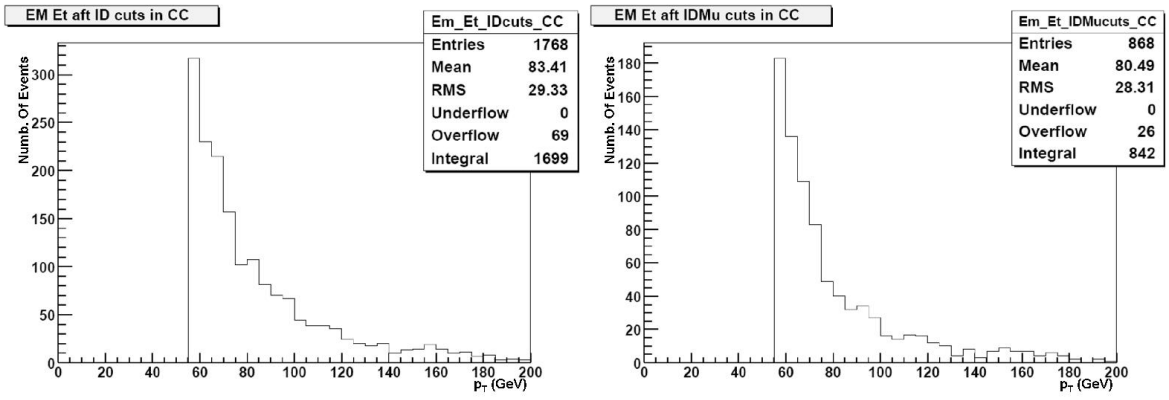

Figure 5.1: On the left is the p_T distribution for events that pass all the EM ID requirements including HMx7. On the right is the distribution after making the muon veto.

- Veto on cosmic bremsstrahlung events. See Appendix A for the details of cosmic bremsstrahlung event identification and removal.
- Primary vertex requirement: The event's primary vertex is required to have at least three tracks. This is required to make sure that the event is the result of a $p\bar{p}$ collision. This cut removes events with leftover energy from a previous crossing or from a cosmic event.
- Preshower requirement: To use only those events that contain central preshower information.

The primary vertex and preshower requirements are made to ensure that the event is the product of a $p\bar{p}$ interaction and that there is enough information in the events to correctly reconstruct the energies, respectively. To determine the number of signal events that would be removed by the vertex and preshower requirements, a sample of $W \rightarrow e\nu$ events in data was used which is the same data sample used to study the bremsstrahlung veto. The details of the data selection are presented in Appendix A. The study showed that the combined requirements remove 3% of $W \rightarrow e\nu$ signal events. Figures 5.1 to 5.4 contains the p_T distribution for the events remaining after every requirement. The left histogram in Figure 5.1 contains all the events with photon ID requirements including the HMx7 cut and the histogram on the right is for events that pass the Muon veto. Figure 5.2 shows the remaining

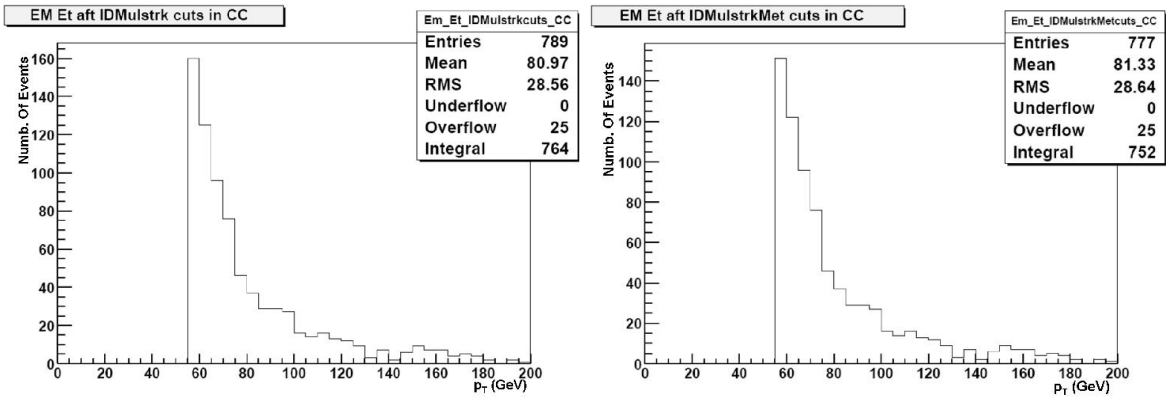

Figure 5.2: p_T distributions for events passing the following additional requirements: No isolated tracks (left) and the $\not\!\!E_T$ requirement (right).

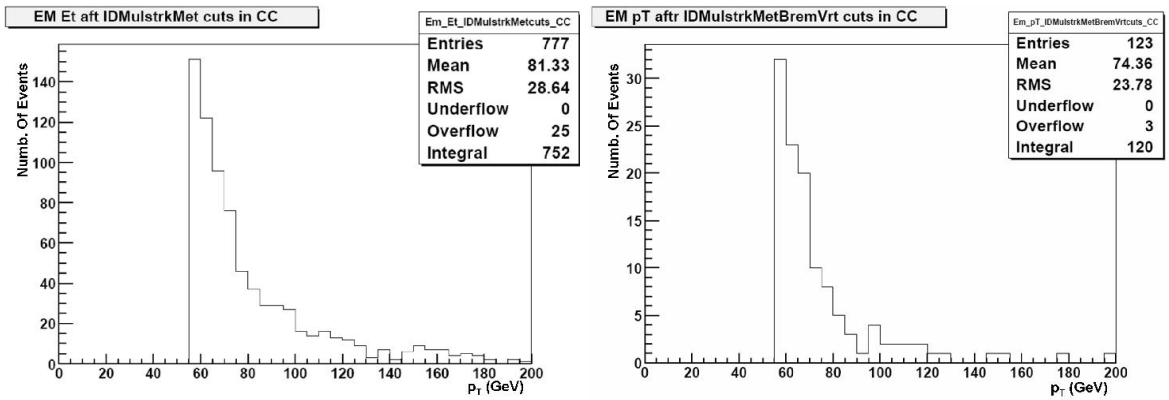

Figure 5.3: p_T distributions for events passing the following additional requirements: Veto on bremsstrahlung events (left) and the vertex requirement (right).

events after the isolated track veto (left) and the $\not\!\!E_T$ requirement (right). Figure 5.3 shows the remaining events after the bremsstrahlung veto (left) and the vertex requirement (right). Figure 5.4 contains the remaining events after requiring that the events contain preshower information (left) and the figure on the right shows the last 70 events superimposed with the events that pass the photon ID cuts. Table 5.1 contains the event count after every requirement or veto. The cosmic muon background is enormous. Even after all the cuts, still some will pass and cause the background events.

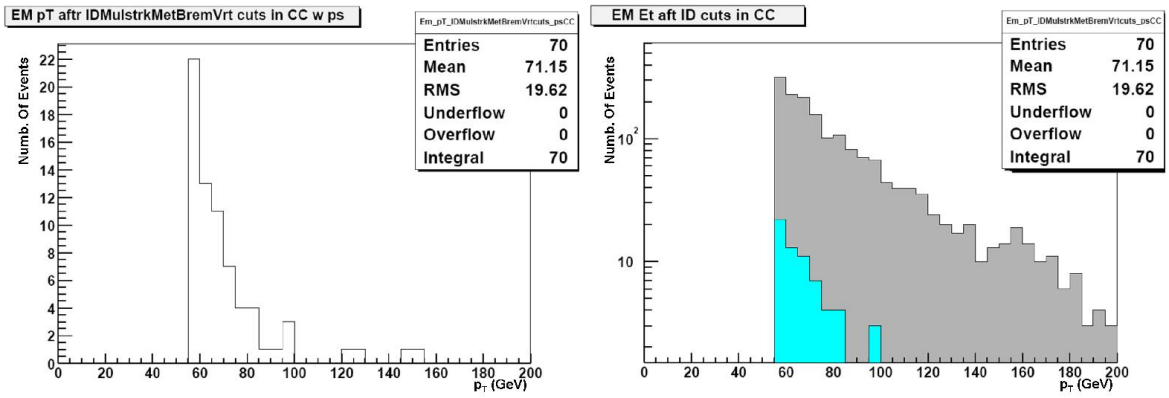

Figure 5.4: p_T distributions for events passing the vertex requirement (left) and the final 70 events (right) superimposed on the p_T distribution of the events passing the photon ID requirements.

Table 5.1: Event count after every cut. The photon ID contains all of the cuts as described in the first set of bullets in Section 5.1.2

Requirement or Veto	Events remaining
Photon ID cuts	1768
Muon Veto	868
Isolated Track veto	789
Missing E_T	777
Bremsstrahlung veto	245
Primary Vertex requirement	123
Preshower requirement	70

Photon ID Requirements Efficiency

The estimation of the EM ID requirements efficiency has to be done with MC events since there is no clean resonance in data to yield a source of photons in the appropriate energy range. Therefore, there are a few options for gaining an understanding on photons directly from the data. In the case of electrons, the resonance peak for $Z \rightarrow ee$ can be used employing the tag and probe method.

For the efficiency calculation, a sample of $Z\gamma \rightarrow \nu\nu\gamma$ MC events was used, see Section 5.2.2 for the event generation details. The calculations procedure is as follows:

- Identify the generated photons using PDGID = 22[6] that does not have a parent[7].
- Require the generated photon to be in $|\eta| < 1.1$.
- Match the generated photon to a calorimeter cluster.
- The next step is to identify the photon using the reconstructed EM cluster as done for data events, see Section 5.1.2 above.
- Require the reconstructed photon to be isolated from any other particles.
- Calculate the efficiency.

The efficiency is simply the number of photons passing all of the reconstruction requirements divided by the number of generated photons that satisfy the photon ID requirements. The EMID efficiency was measured to be 83.0 $\pm$ 2.5 (stat)%. Figure 5.5 show the efficiency as function of p_T and Figure 5.6 shows it as function of $\eta_{detector}$.

Several attempts to further identify and reduce the number of background events were made. In particular, a tool called photon pointing was used. This tool uses EMCal tower information to extrapolate the photon's point of origin, or the event's primary vertex. The pointing extrapolations turned out to be inconclusive for the data set used for this analysis. Figure 5.7 shows the difference between the z-coordinate of the primary vertex and z-coordinate from the pointing extrapolation for W events. For the pointing study, $W \rightarrow e\nu$ events in data were used to determine the pointing shape for signal events. To generate the plot in Figure 5.7 the track attached to the electron candidate was removed and the event revertexed. The absence of the track gives us an EM object that passes all of the photon ID requirements. The fit in the plot is a triple Gaussian function which was needed because there are three distinct shapes in the distribution. A sample of events that have been identified with muons undergoing bremsstrahlung in the EMCal was used to determine what the shape of this particular background was. Figure 5.8 shows the distribution for the bremsstrahlung sample. As shown with the Gaussian fit, the distribution is not significantly different to be useful as a background discriminant. Figure 5.9 shows the distribution in

[6]PDGID is the Particle Data Group Identification numbering convention. This convention is used by the PYTHIA event generation to number the generated particles.

[7]A parent particle is the particle that decayed to create a photon plus other particles. Here, the interest is in photons coming from initial state radiation

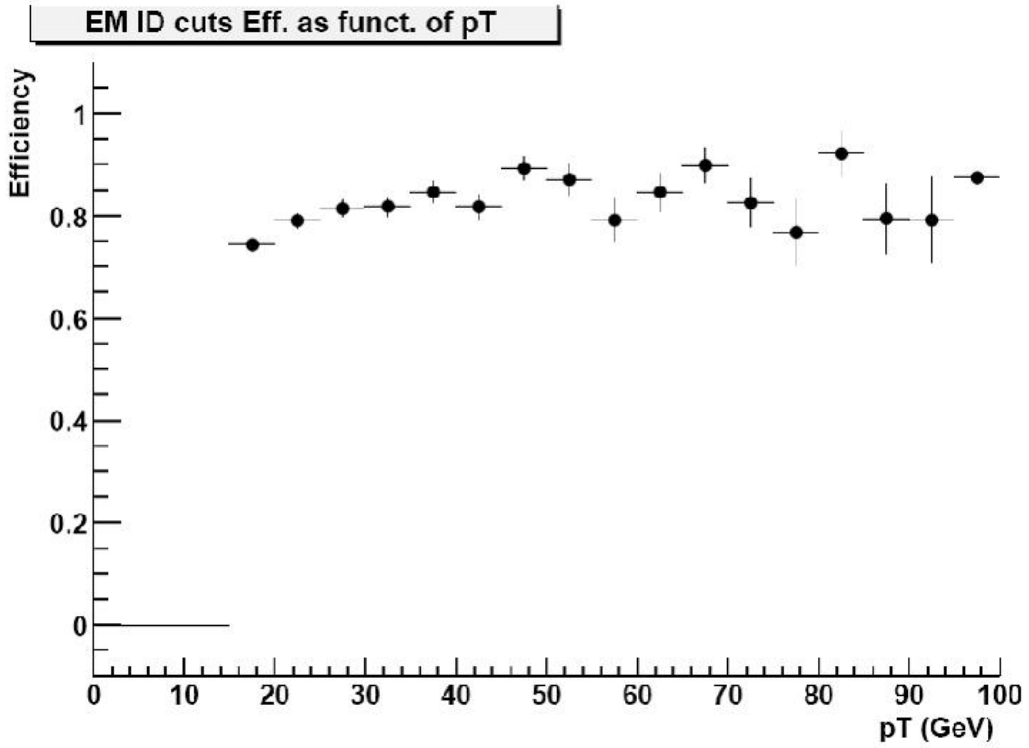

Figure 5.5: EM ID requirements for efficiency as function of the p_T for central photons.

data fitted with the combination of the fits for the W and the bremsstrahlung samples. It was decided that the pointing program did not produced a usable discriminant.

5.2 Backgrounds

There are three types of backgrounds to the LED signature, these are:

- Events with $\not\!\!E_T$ due to one or more neutrinos being produced.
- Events with $\not\!\!E_T$ from purely instrumental effects.
- Cosmic muons that undergo bremsstrahlung in the EMCal.

This section describes the backgrounds present in the single photon and $\not\!\!E_T$ data set. The methods used to estimate the different background are also presented.

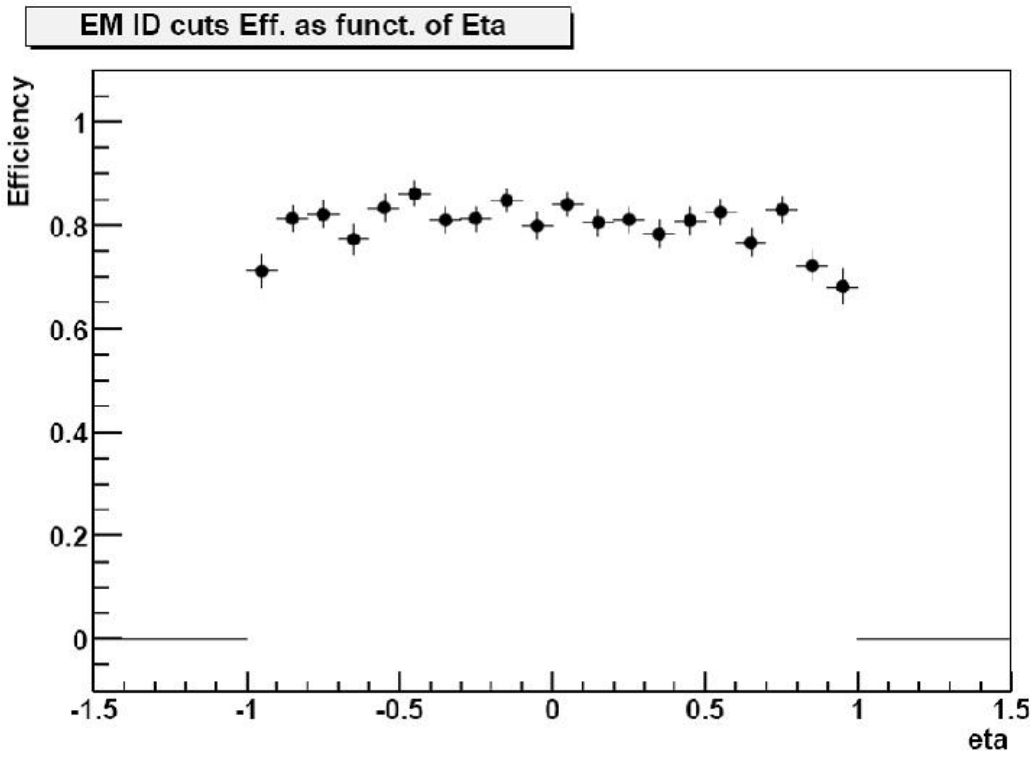

Figure 5.6: EM ID requirements for efficiency as function of the detector η for central photons.

5.2.1 Sources of backgrounds

All major sources of background to LED signal are considered in this section. After applying the selection cuts, most had negligible contribution. The background processes are now discussed:

- $W \rightarrow e\nu$ production: When the electron is misidentified as a photon. The Feynman diagrams for the production and decay of this process are shown in Fig. 5.10.
- $W\gamma \rightarrow l^{\pm}\nu\gamma$ production: Where the lepton is lost (see Fig. 5.11 for an example).
- Prompt $\gamma\gamma$ production: Where one of the photons is lost (see Fig. 5.12 for an example).
- Dijet production: Where one of the jets is lost and the other is misidentified as a photon (see Fig. 5.13 for an example).

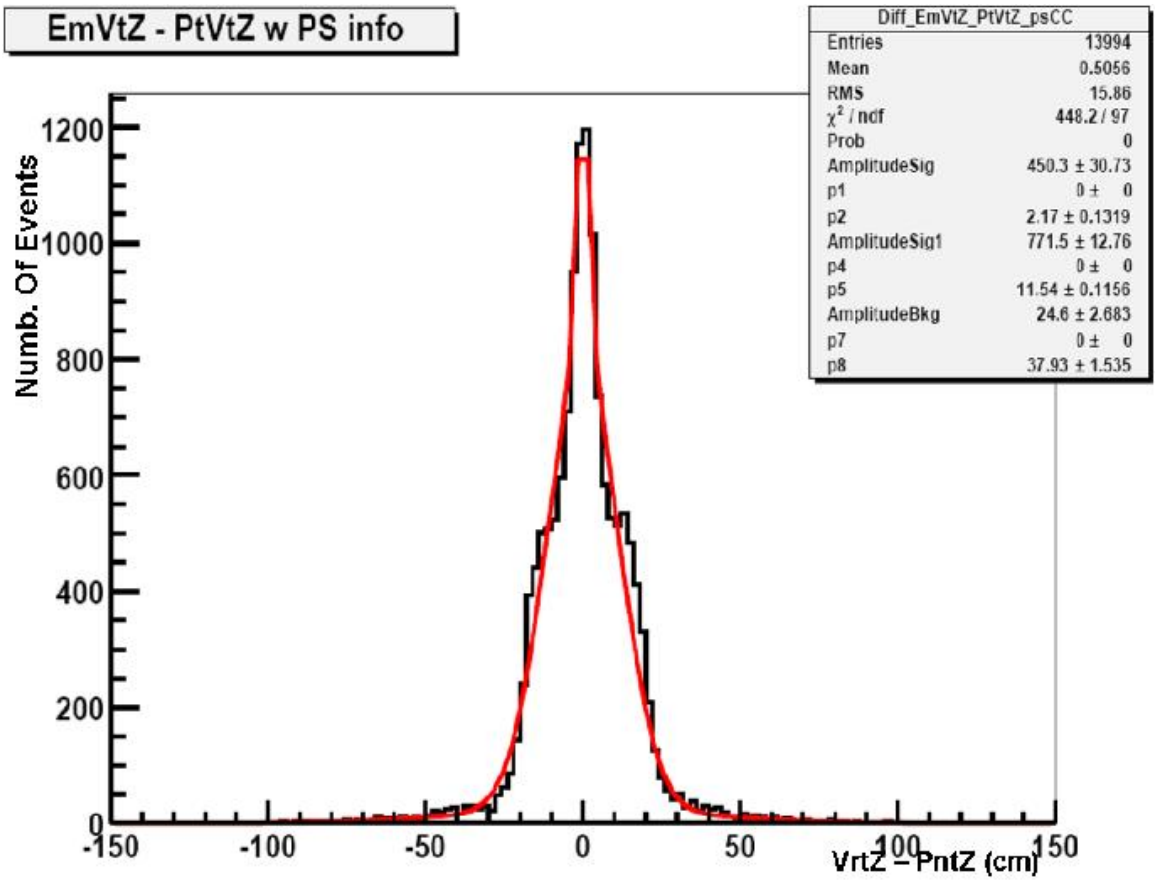

Figure 5.7: Distribution of the difference between the z-coordinate from the primary vertex and z-coordinate returned by the pointing program. The data plotted is for $W \rightarrow e\nu$ events in data. The triple Gaussian fit was needed because there are three distinct shapes in the distribution.

- $\gamma+$ jet events: Where the jet is lost (see Fig. 5.14 for an example).
- $q\bar{q} \rightarrow Z\gamma \rightarrow \nu\nu\gamma$: This is the only irreducible physics background in this particular channel (see Fig. 5.15).
- Cosmic events: When a cosmic muon traverses the detector and deposits energy, through bremsstrahlung, faking a photon coming from the interaction region.

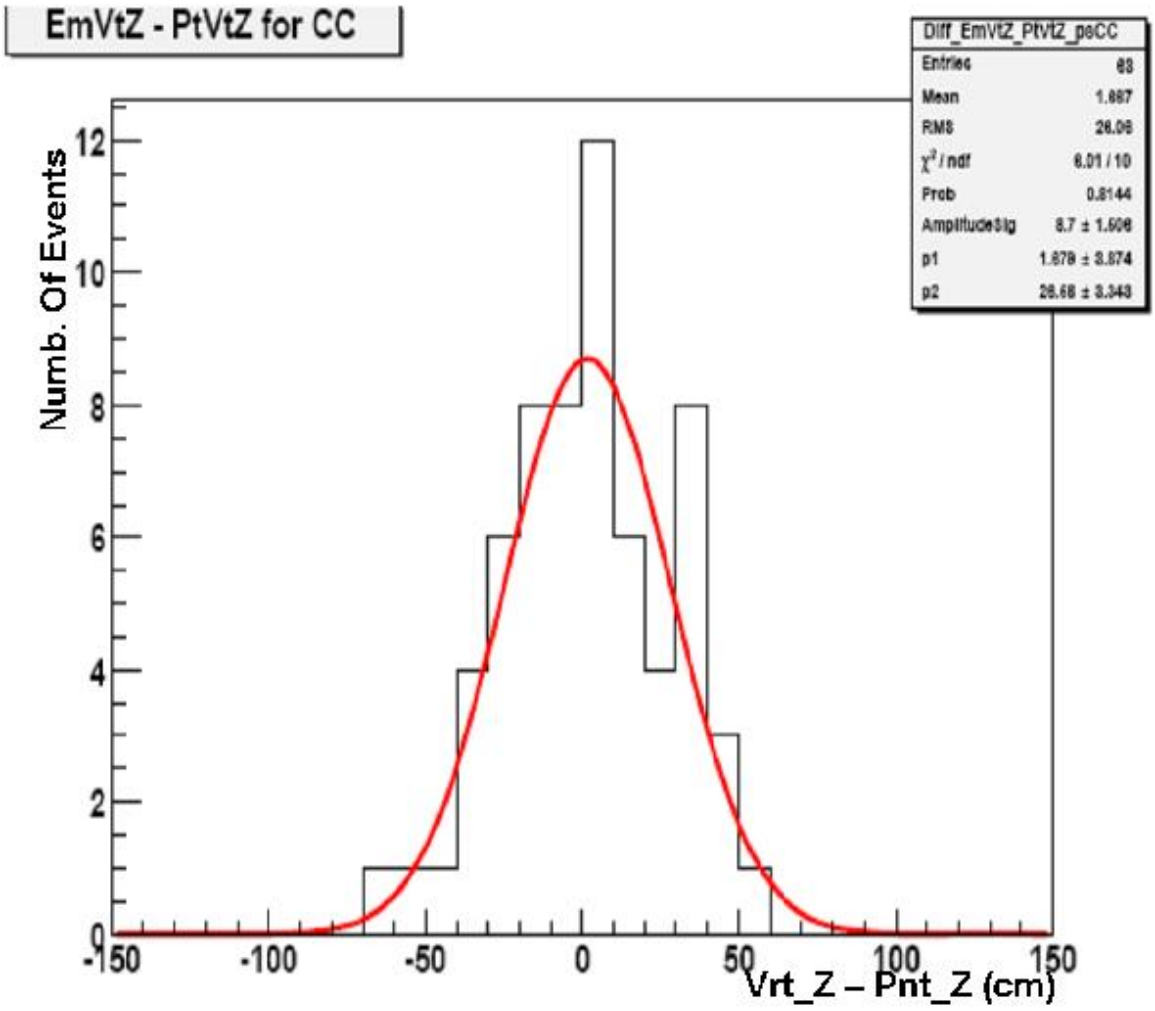

Figure 5.8: Distribution of the difference between the z-coordinate from the primary vertex and z-coordinate returned by the pointing program for a sample of bremsstrahlung events. The fitting function is a single Gaussian.

5.2.2 Estimation of backgrounds

With the exception of the $W(jet) \rightarrow e\nu(jet)$ and the cosmic backgrounds, all of the backgrounds were studied with MC events. The samples were normalized to data using the cross sections (σ), the acceptance (A), and the integrated luminosity ($\mathcal{L}_{int}$),

$$N = \mathcal{L}_{int} \times \sigma \times A. \tag{5.1}$$

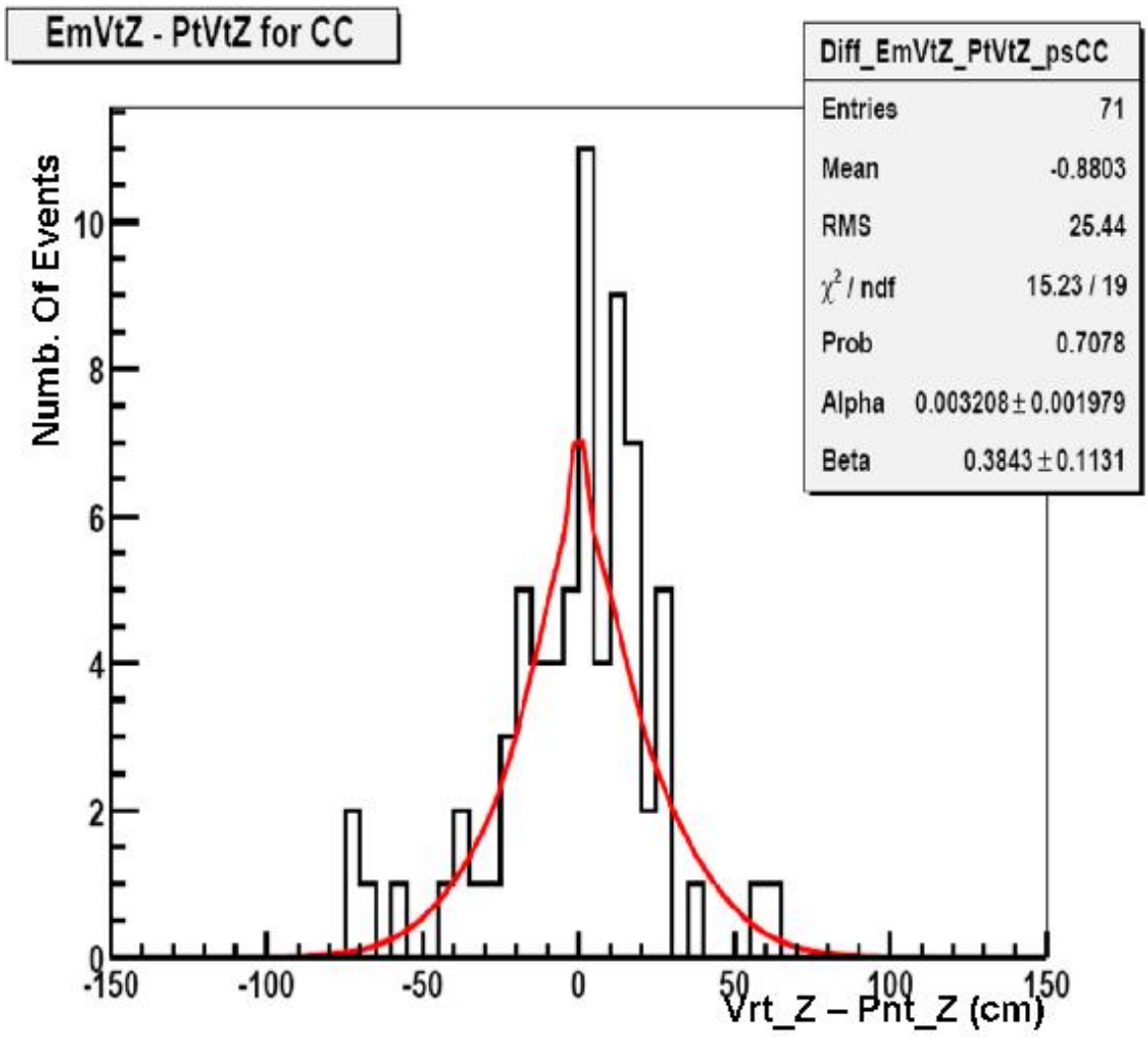

Figure 5.9: Distribution of the difference between the z-coordinate from the primary vertex and z-coordinate returned by the pointing program for the data events. The fitting function is a combination of the fit functions used to fit the bremsstrahlung and W samples.

This equation agrees with equation 3.6. The published cross sections were used in this study. The results are summarized in Table 5.2 at the end of this section.

Estimating the Electroweak Background

The first two items in the list of backgrounds, $W \rightarrow e\nu$ and $W\gamma \rightarrow l^{\pm}\nu\gamma$, are the electroweak instrumental background contribution to the signal. The process $W \rightarrow e\nu$

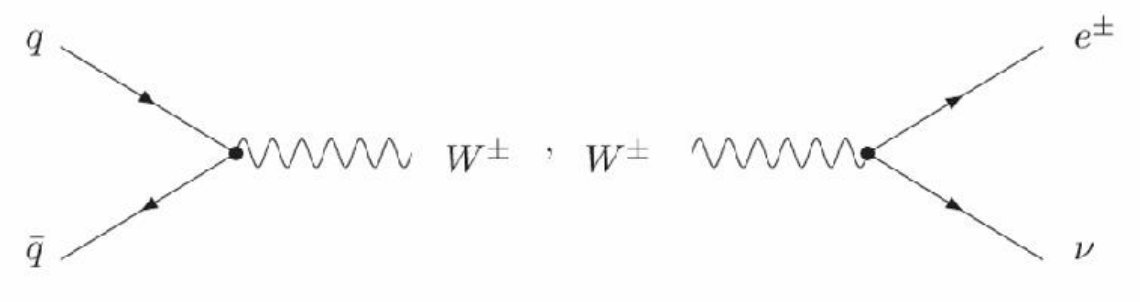

Figure 5.10: Feynman Diagrams for $q\overline{q} \rightarrow W^{\pm} \rightarrow e^{\pm}\nu$.

was calculated from the 1EMloose sample by relating photons to electrons via Tracking Efficiency. Derivation of the final expression is as follows: The number of electrons faking a photon in events coming from $W \rightarrow e\nu$ is given by

$$N_W(e) = \sigma(p\overline{p} \rightarrow W + X) \times Br(W \rightarrow e\nu) \times \mathcal{L}_{int} \times A \times \epsilon(trigger) \times \epsilon(EM) \times (1 - \epsilon(track)), \tag{5.2}$$

where $\sigma(p\overline{p} \rightarrow W + X)$ is the production cross-section, $Br(W \rightarrow e\nu)$ is the electron ν branching fraction, $\mathcal{L}_{int}$ is the integrated luminosity, A is the combined geometric and kinematic acceptance, $\epsilon(trigger)$ is the trigger efficiency [48], $\epsilon(EM)$ is the EM object identification efficiency, and $\epsilon(track)$ is the tracking efficiency. The tracking efficiency has been measured, in Reference [50], to be $72.7 \pm 0.9(stat) \pm 2.0(syst)\%$. A subset of the tracking efficiency is the track matching efficiency which has been calculated and presented in Appendix B.

The contribution from the $W\gamma \rightarrow e\nu\gamma$ is suppressed by the explicit requirement, in data, that the events must have one EM object and nothing else. This would be events for which the lepton has failed detection due to cracks in the detector, or the lepton traversed to a region of the detector not used in this analysis. For events that pass all the EM ID requirements, this background is further suppressed by requiring the $\not\!\!E_T > 45$ GeV. The background from this process is 1.2 ± 1.1 events.

The contribution from $W(\gamma) \rightarrow \mu\nu(\gamma)$ was studied using Monte Carlo (MC) events. The sample was generated with PYTHIA v6.202 [52] using the CTEQ4L parton distribution functions (PDF) table. The event simulation was ran through the standard DØ detector

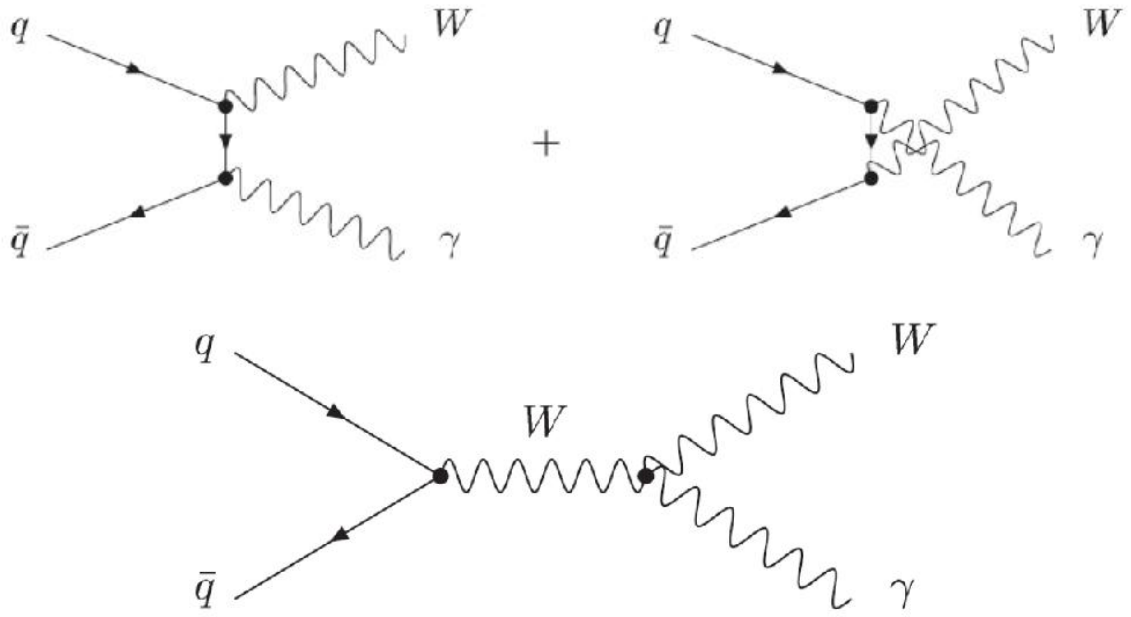

Figure 5.11: Feynman Diagrams for $q\bar{q} \rightarrow W^{\pm}\gamma$ production.

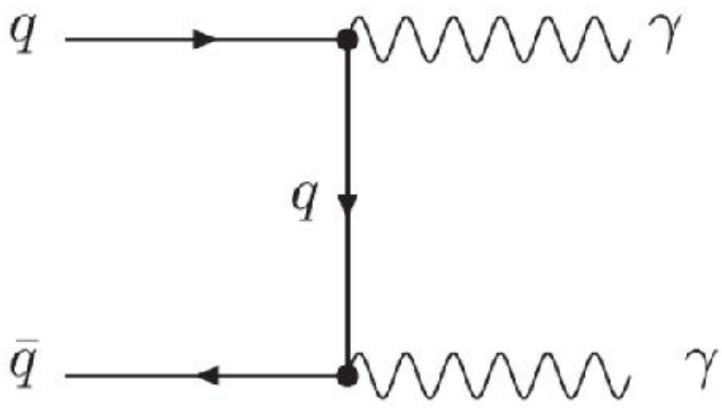

Figure 5.12: Feynman Diagrams for direct $\gamma\gamma$ production.

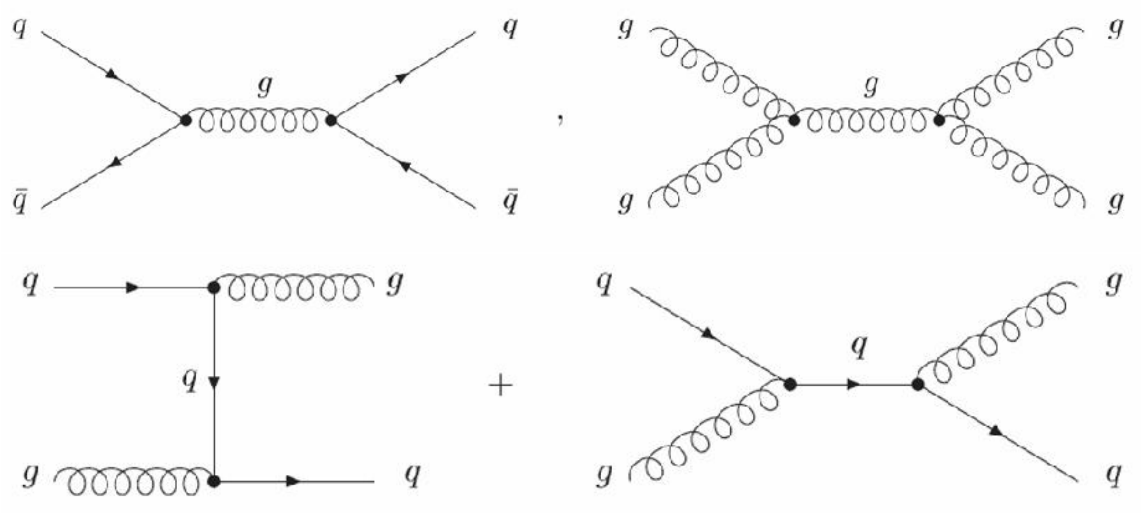

Figure 5.13: Examples of dijet production Feynman Diagrams.

simulation and reconstruction (Reco) software. The sample of 10,000 events was requested by the New Phenomena (NP) group [53] (request # 8306) and reconstructed with DØ Reco release p14.02.00, as described in Chapter 4. This background becomes statistically small, but non-zero, after making the explicit requirement for the events not to have any reconstructed muons of any quality, as defined in Section 4.3.

Estimating the QCD Background

The QCD backgrounds relevant to this analysis are the direct photon events (γ+ jet), prompt $\gamma\gamma$ production, and dijet production. Figures 5.12 to 5.14 depict the Feynman diagrams of these processes. The requirements that the event must have only one EM object reduces the $\gamma\gamma$ contribution to a negligible level. The additional requirement that the EM energy tower must contain at least 90% of the energy in the calorimeter also reduces the dijet contribution to a negligible level and was ignored. These requirements also reduce the direct photon contribution to a very small, but nonzero, number. This is due to the size of the direct photon cross section. All of the above contributions to the background were studied with MC data. The details are as follows:

- The direct photon sample was generated with PYTHIA v6.202 [52] using the CTEQ5L PDF table. The simulation was ran through the standard DØ simulation and Reco

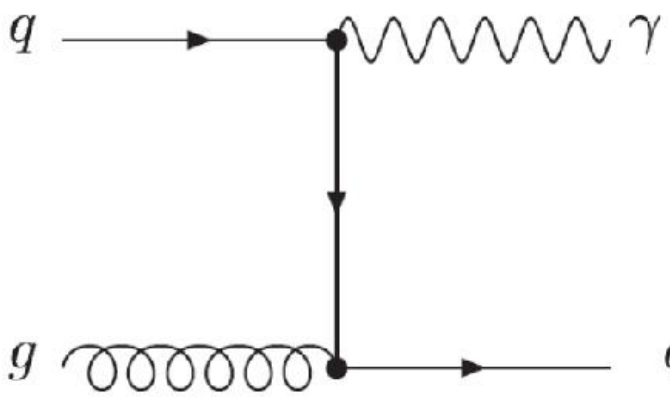

Figure 5.14: Example of Gamma+Jet production Feynman Diagram.

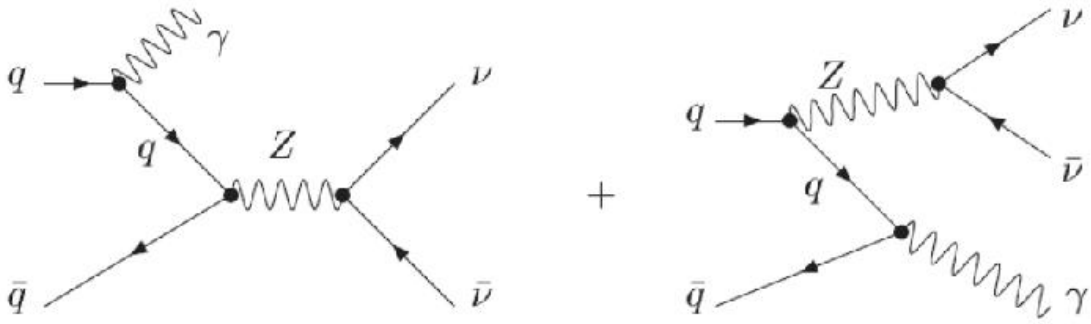

Figure 5.15: Feynman Diagram of the electroweak process $Z\gamma \rightarrow \nu\nu\gamma$. This is the only irreducible background of the single photon and $\not\!\!E_T$ data set.

software. The sample of 300,000 events was requested by the NP group in three different requests (request numbers 11638-11640). Each request generated 100,000 events in photon p_T bins 40-80 GeV, 80-160 GeV, and 160-320 GeV respectively. They were reconstructed with DØ Reco release p14.05.01, as described in Chapter 4.

- The $\gamma\gamma$ sample was generated with PYTHIA v6.202 using the CTEQ5L PDF table. The simulation was ran through the standard DØ simulation and Reco software. The sample of 56,500 events was requested by the NP group (request number 11253). It

was reconstructed with DØ Reco release p14.05.02.

Estimating the $Z\gamma \to \nu\nu\gamma$ Background

The electroweak process $Z\gamma \to \nu\nu\gamma$ is the only background that has identical signal as the single photon and $\not\!\!E_T$ data set, also referred to as the irreducible background. Figure 5.15 shows the Feynman diagram of this process. It was studied using MC data generated with PYTHIA v6.202 using the CTEQ5L PDF table. A sample of 9,250 events was generated and ran through the standard DØ simulation and Reco software. The data was reconstructed with release p16.04.00. This release was chosen because it contained updated detector correction factors for the EM part of the calorimeter in the calculation of the EM energy scale and $\not\!\!E_T$, as described in Sections 4.1.2 and 4.6 respectively. The contribution of these events to the background is 10 ± 1.0 events.

The Cosmic Ray Background

Most cosmic events are identified and tagged by the muon reconstruction (MuReco) algorithms, as outlined in Section 4.3. Cosmic muons that do not traverse through the interaction region of the detector are much harder to identify and the MuReco algorithms do not 'catch' them. Such events often leave a trace, or track, through the muon system which can be used in their identification and removal. These cosmic muons are not worrisome unless they deposit energy in the EM part of the calorimeter through bremsstrahlung. It turns out that this is a significant background in events with single photon and $\not\!\!E_T$. To identify and remove them, an algorithm was developed that uses the muons path and matches it to the location of the photon candidate in the EM part of the calorimeter. If the muons path interpolates to the photon, the event is tagged as a cosmic event and removed. Appendix A has a detailed presentation of the algorithm and the removal efficiency.

5.3 Signal Analysis

5.3.1 Signal Monte Carlo

For the simulation for the LED in the single photon and $\not\!\!E_T$ channel, the PYTHIA v6.2 generator was used. It was modified by Dr. Alexander Belyaev [54] to include this particular process. We generated 1000 events for each number of extra dimensions (n) ranging from 2 to

Table 5.2: Background estimates for the single photon and $\not\!\!E_T$ data sample corresponding to the 196 pb^{-1} dataset.

Background	N	σ (pb)
$W(jet) \rightarrow e\nu(jet)$	1.2 $\pm$ 1.1	1943 $\pm$ 39
$W\gamma \rightarrow \mu\nu\gamma$	0.7 $\pm$ 0.15	15.03 $\pm$ 1.94
γ + jet	2 $\pm$ 0.2	970 $\pm$ 14
Prompt $\gamma\gamma$	0	6.8 $\times 10^5 \pm$ 125
$Z\gamma \rightarrow \nu\nu\gamma$	10 $\pm$ 1.0	2 $\pm$ 0.4
Total	14 $\pm$ 1.5	

8. The fundamental mass scale (M_D) was varied from 200 to 1400 GeV in intervals of 100 GeV for cross section calculations, and from 600 GeV to 800 GeV for signal studies. The dataset used is not sensitive to signal events for $M_D > 800$ GeV and the case for $M_D < 600$ GeV has been previously studied. The number of expected signal events was calculated with Equation 5.1 using the cross section predicted by the MC program. To add the detector simulation to the signal MC samples, the PMCS (Parametrization Monte Carlo Simulation)[55] fast MC was used. PMCS is a Monte Carlo software package that parametrizes detector effects to the MC generated events. The resolution of the subdetectors is parametrized from data. The resolution functions of the calorimeter are functions of E_T and p_T of the measurements respectively. As mentioned, these parameters are determined from data, so each has an associated error which contributes to the uncertainty in the acceptance. Each parameter in the simulation is varied by one sigma from its central value to gauge the effects of these uncertainties and the acceptance is recalculated.

The energy from the parametrization for the calorimeter smearing is given by:

$$E_{smeared} = E' + x * \sigma_E, \tag{5.3}$$

where

$$E' = A + B \times E_{generated} \tag{5.4}$$

is due to the uncertainty in the energy scale. In Equation 5.4, A is an offset parameter and B is a scale factor. In Equation 5.3, x is a Gaussian distributed random number and σ_E is

the energy resolution defined as:

$$\left(\frac{\sigma_E}{E}\right)^2 = C^2 + \frac{S^2}{E} + \frac{N^2}{E^2}, \tag{5.5}$$

where C represents calibration errors[8], S represents the sampling fluctuations[9], and N represents the 'noise'[10]. From $Z \rightarrow ee$ events in the central region, the constant term (C) was determined to be $3.73 \pm 0.28\%$. The sampling term (S) is taken to be the same as from Run I which was determined to be 0.15 $\text{GeV}^{1/2}$. The noise term is also taken to be the same as in Run I, since the physical construction of the calorimeter has not changed, and it was determined to be 0.29 GeV. The scale factor (B) was determined to be 1.0060 ± 0.0017. The offset (A) was determined to be 0.095 ± 0.079 GeV. All of the valued quoted above are for the central region of the calorimeter. A detail discussion on the determination of all the terms can be found in reference [56].

PMCS Acceptance for the Signal MC

The acceptance of the DØ detector for single photons and $\not\!\!E_T$ events may be roughly divided into two separate parts, geometric and kinematic. Geometric acceptance is defined as the fraction of the events accepted by the various fiducial cuts. Kinematic acceptance is the efficiency with which these events will be reconstructed with the proper kinematic properties, such as photon E_T and p_T. The kinematic acceptance also takes into account photons which were produced with lower E_T, but due to finite resolution effects were reconstructed with high enough E_T to pass the selection criteria. These efficiencies are correlated through the transverse momentum of the system, therefore they are calculated together. As mentioned in various previous sections, this analysis uses the central region of the detector (detector $|\eta| < 1.1$). This area contains the best tracking efficiency, and so the best photon reconstruction. The photon is required to be reconstructed within the calorimeter module boundaries, so the energy of the photon may be determined with the best resolution. The governing equation is as follows:

$$A = \frac{N(|\eta_{\gamma CAL}| < 1.1; \phi_{fiducial}; p_{T_{\gamma S}} > 55GeV)}{N(p_{T_{\gamma G}} > 55GeV)} \tag{5.6}$$

[8]Meaning the amount to which any given energy measurement is wrong due to pedestals, gains, non-linearity, etc.

[9]Meaning the error due to the amount of shower sampled.

[10]This noise in mainly due to the natural radioactivity of the uranium which contributes energy to the calorimeter.

Table 5.3: Results of acceptance calculation for signal events processed with PMCS for different values of M_D and number of extra dimensions.

M_D (GeV)	No. of extra dimensions (n)	Accp. (%)	Stat. Err (%)	Syst Err (%)
600	2	86.2	± 0.7	± 0.9
600	3	88.2	± 0.8	± 0.9
600	4	86.2	± 0.7	± 0.8
600	5	86.1	± 0.7	± 0.8
600	6	84.2	± 0.7	± 0.8
600	7	86.2	± 0.7	± 0.8
600	8	86.3	± 0.7	± 0.8
700	2	88.7	± 0.8	± 0.9
700	3	88.2	± 0.8	± 0.9
700	4	86.2	± 0.7	± 0.8
700	5	86.1	± 0.7	± 0.8
700	6	84.2	± 0.7	± 0.8
700	7	86.2	± 0.7	± 0.8
700	8	86.3	± 0.7	± 0.8
800	2	88.7	± 0.8	± 0.9
800	3	88.2	± 0.8	± 0.9
800	4	86.2	± 0.7	± 0.8
800	5	86.1	± 0.7	± 0.8
800	6	84.2	± 0.7	± 0.8
800	7	86.2	± 0.7	± 0.8
800	8	86.3	± 0.7	± 0.8

where the numerator contains the number (N) of events within the η range in the EM part of the calorimeter (EM Cal), the ϕ fiducial in the EM Cal, and the p_T cut for the smeared photons ($p_{T_{\gamma S}}$). The denominator has the number of generated events that pass the p_T cut for the photon ($p_{T_{\gamma G}}$).

The acceptance ranges from about 84% to about 88% depending on the parameters number of extra dimensions and the fundamental mass scale of the generated events. Table 5.3 contain the calculated acceptance for the different parameter values. Every parameter in PMCS has an error associated with them which quantifies exactly how certain one can be of the detectors performance. One can get a handle of the systematic error by varying these parameters within these errors. There are three parameters that matter most for the

acceptance in single photon events. These parameters are: N (the noise), C (the constant) and B (the scale factor) as listed in Section 5.3.1. They were varied by the maximum of the error and the simulation was done once again. The difference between the two results was taken to be the systematic error which are listed in Table 5.3.

5.3.2 Calculation of the Limits

With the excess of events over the Standard Model assumed to be backgrounds, the lower limits on the number of extra dimensions (n) and M_D for the production of LED are calculated from the predicted cross sections. After imposing all of the data selection, photon ID, and data quality cuts to the data set, a final sample of 70 events remain. Out of the 70 events, about 21% are identifiable background events. The rest are most likely cosmic background and instrumental background events that can not be further reduced. To make a conservative estimate on M_D mass limits for various number of extra dimensions, we treat these remaining events as signal. Since the remaining events are relatively large, we are using a Gaussian distribution in the estimation of mass limits. What follows is a brief discussion of Gaussian distributed measurements. However, the reader is pointed to many publication on the subject, in particular Reference [5].

The governing equation is

$$1 - \alpha = \frac{1}{\sigma\sqrt{2\pi}} \int_{\mu-\delta}^{\mu+\delta} e^{-(x-\mu)^2/2\sigma^2} dx, \tag{5.7}$$

is the probability that the measured value, in this case x, will fall within $\pm\delta$ of the true value μ. It can also be interpreted as the probability for the interval $x \pm \delta$ to include μ. Figure 5.16 shows a $\delta = 1.64\sigma$ confidence interval unshaded. One can set a one-sided (upper or lower) limit by excluding above $x + \delta$ (or below $x - \delta$). Values of α for frequently used choices of δ are given in Table 5.4.

Figure 5.17 is a graph of the total cross section as function of M_D for the number of extra dimensions being studied. The black line marks the cross section for the central value of events (56 events) and the red line marks the 95% confidence level (CL). Figure 5.18 is the same plot as in Figure 5.17 but zoomed in the area where the limits are being set. The largest contribution on the systematic error comes from the uncertainty in the $\mathcal{L}_{int}$. The other error contributions that have been accounted for come from the uncertainties in the:

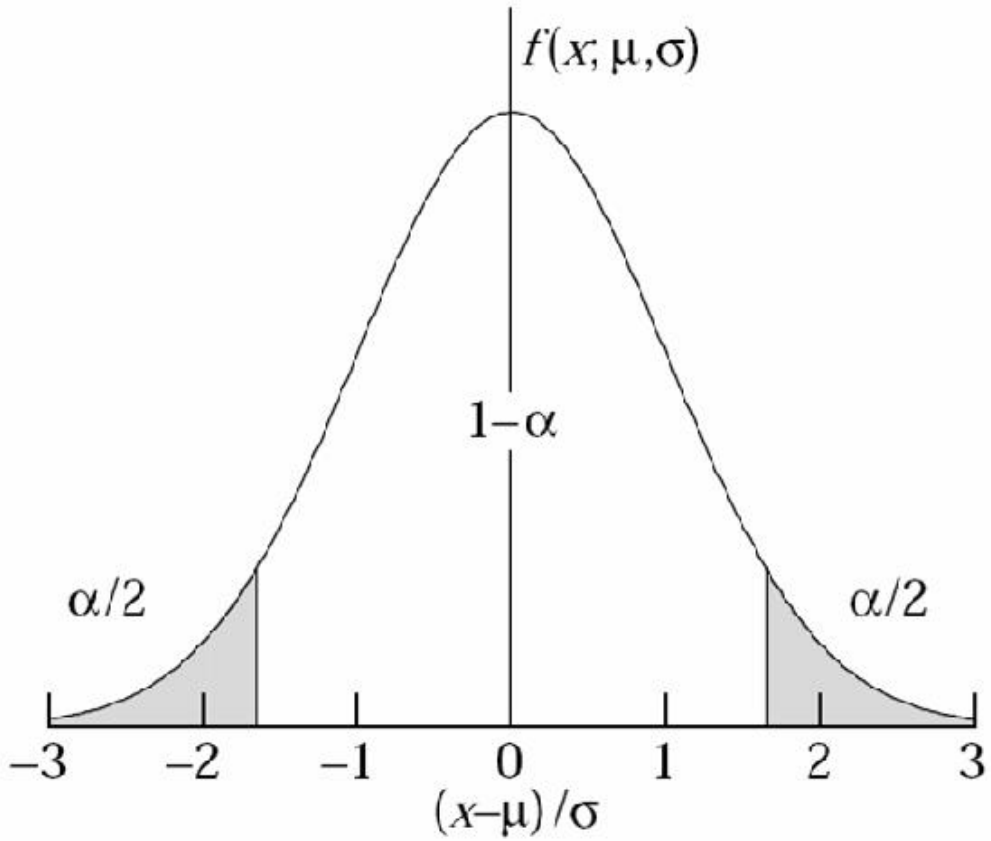

Figure 5.16: Illustration of a symmetric 90% condidence interval (unshaded) for a measurement of a single quantity with Gaussian errors. Integrated probabilities, defined by α, are shown.

Table 5.4: Area of the tails α outside $\pm\delta$ from the mean of a Gaussian distribution

α (%)	δ	α (%)	δ
31.73	1σ	20	1.28σ
4.55	2σ	10	1.64σ
0.27	3σ	5	1.96σ
6.3×10^{-3}	4σ	1	2.58σ
5.7×10^{-5}	5σ	0.1	3.29σ
2.0×10^{-7}	6σ	0.01	3.89σ

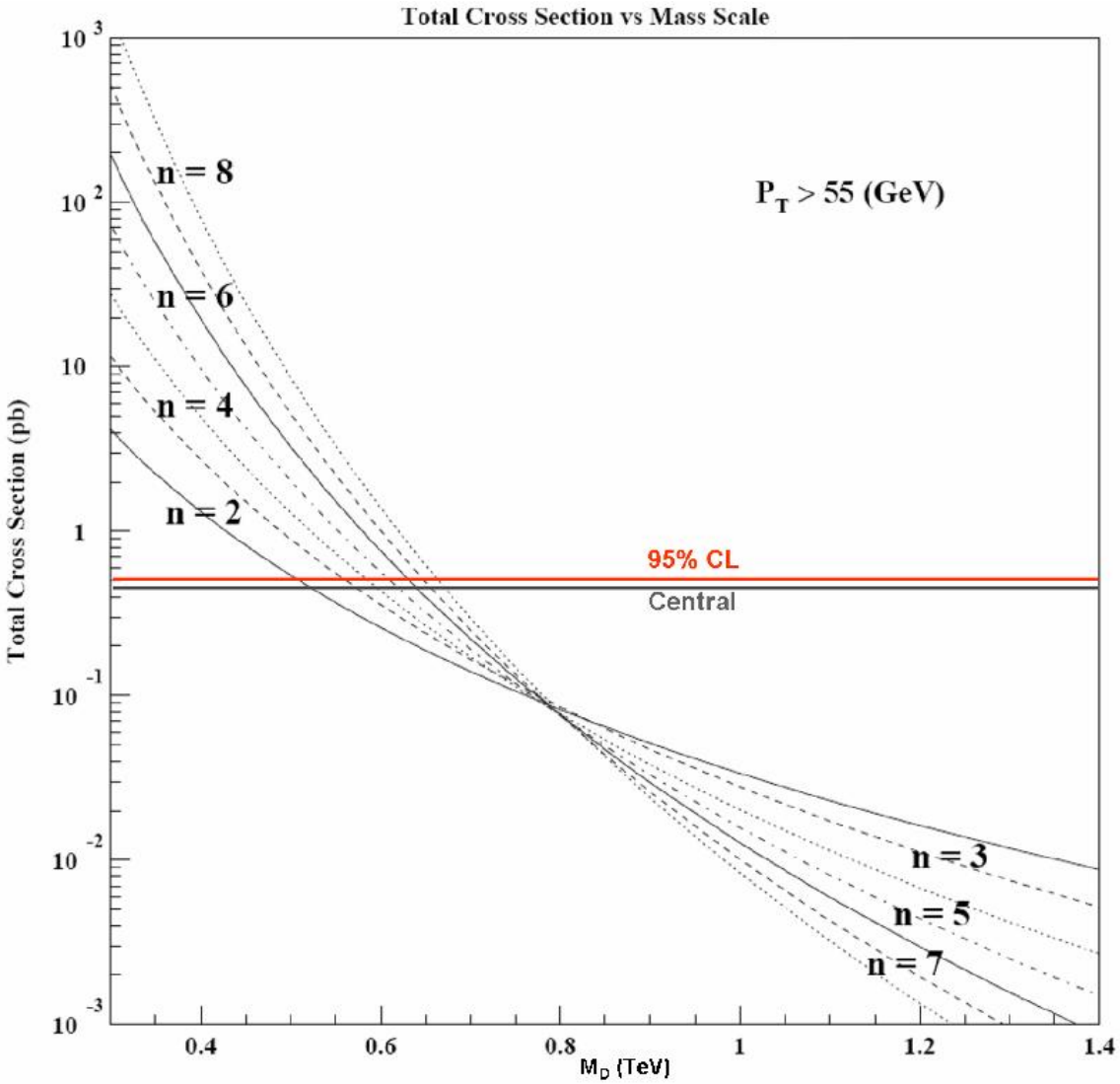

Figure 5.17: Cross section as function of M_D for n=2,3,4,5,6,7,8. The black line marks the central value based on the assumption of 56 signal events and the red line marks the 95% CL.

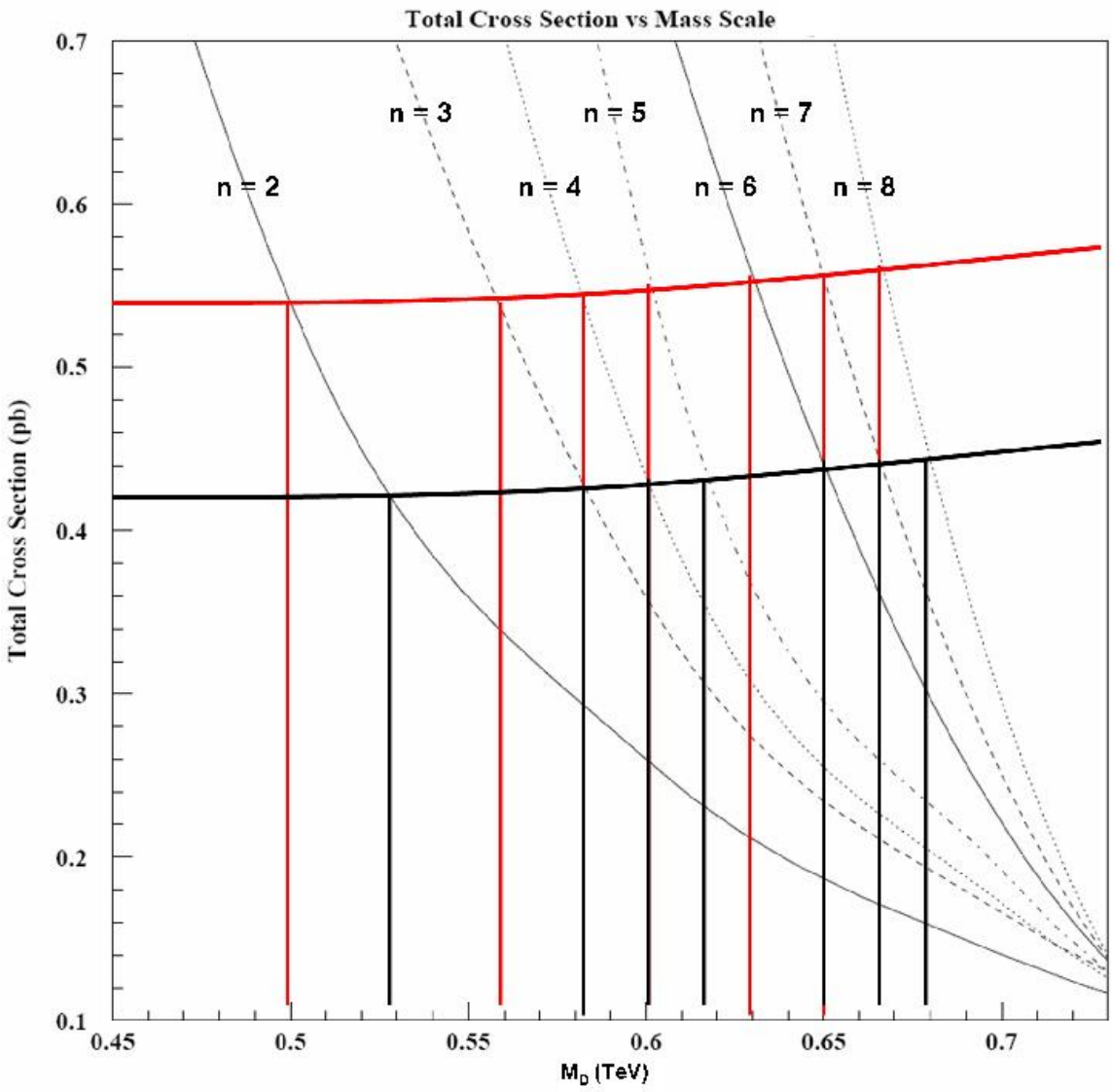

Figure 5.18: Cross section as function of M_D for n=2,3,4,5,6,7,8. The black horizontal line marks the central value and the red horizontal line marks the 95% CL. The vertical lines point down to the lower limit of the M_D.

- Trigger efficiency: $\epsilon_{trigger} = (97 \pm 2.0)\%$.
- Photon ID efficiency: $\epsilon_{\gamma ID} = (83.0 \pm 2.5(\text{stat}) \pm 2.0(\text{syst}))\%$.
- The efficiency of the vertex requirement and requiring that each event to have preshower information which is $(94.5 \pm 1.1)\%$.
- Total efficiencies: $\epsilon_{Total} = (76 \pm 6)\%$.

The systematic error in the photon ID efficiency was taken from the results that have been certified by the photon ID group at DØ , see Reference [58].

Visible Bremsstrahlung Events

As mentioned in Section 5.3.2 above, most of the final 70 events being used to set the limits are expected to be bremsstrahlung background events that can not be identified analytically. By visually examining the event displays of a sample of 40 events from the 70 remaining events, it was determined that an additional 40% were in fact bremsstrahlung events. These events are not selected by the bremsstrahlung veto because they simply do not have enough information in the muon system to be identified. As an exercise, an additional 28 events were subtracted from the data set to calculate the limits that the reduced number of events would set. Figure 5.19 shows the cross section as function of the M_D for the different number of extra dimensions. The limits in the distribution of Figure 5.19 are not used in the final results because these were not calculated using an analytical method. The limits that would be set by the 28 events are listed in Table 5.5.

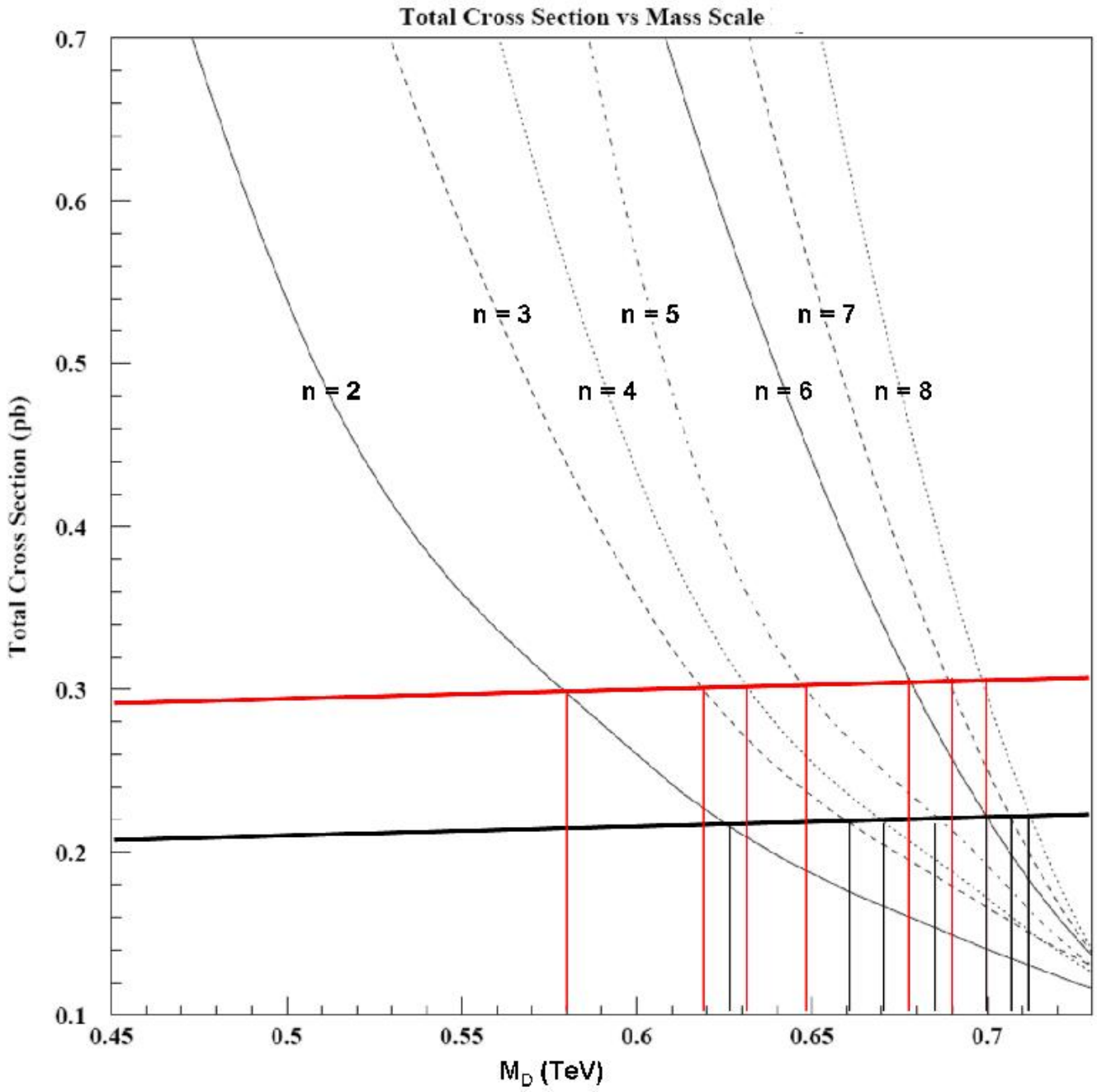

Figure 5.19: Cross section as function of M_D for n=2,3,4,5,6,7,8 after an additional removal of bremsstrahlung events. The black line marks the central value based on the assumption of 28 signal events and the red line marks the 95% CL.

Table 5.5: Lower limits of M_D for n = 2,3,4,5,6,7, and 8 assuming 28 signal events. Presented are both, the central value and the 95% CL.

Number of extra dimensions (n)	Central value of M_D (GeV)	95% CL (GeV)
2	626^{+30}_{-36}	580
3	661^{+27}_{-32}	619
4	671^{+28}_{-30}	632
5	685^{+25}_{-20}	648
6	700^{+16}_{-13}	678
7	707^{+12}_{-10}	690
8	712^{+10}_{-9}	700

CHAPTER 6

The Results and Conclusion

The 95% confidence level M_D exclusion limits and maximum sensitivities are determined by interpolating from the points just above the exclusion contour and the points just below the exclusion contour as shown in Figures 5.17 and 5.18. Table 6.1 contains the limits as read from Figure 5.18 for events in the central region ($|\eta| < 1.1$) of the DØ detector. The previously published results by the CDF collaboration at 95% CL are: $M_D \geq 549$, 581, 602 GeV for $n = 4$, 6, and 8 (see Reference [57]) for studies in the single photon and $\not\!\!E_T$ channel. The errors cited in Table 6.1 are statistical and the systematic errors combined.

The DØ collaboration conducted a search for LEDs in the monojet and $\not\!\!E_T$ channel for Run I data. Their results at 95% CL are: $M_D \geq 730$, 680, 640, 630, and 620 for $n = 3$, 4, 5, 6, and 7 respectively [59]. The higher value of their limits is due to the number of subprocesses that can produce a monojet and graviton final state. This means that a smaller cross section

Table 6.1: Lower limits of M_D for $n = 2$, 3, 4, 5, 6, 7, and 8. Presented are both the central value and the 95% CL. The errors noted in the central values are the statistical and systematic errors combined. The largest contribution to the errors comes from the uncertainty of the $\mathcal{L}_{int}$.

Number of extra dimensions (n)	Central value of M_D (GeV)	95% CL (GeV)
2	528^{+25}_{-20}	500
3	585^{+17}_{-16}	558
4	600^{+18}_{-14}	581
5	618^{+15}_{-12}	602
6	650^{+17}_{-17}	630
7	665^{+12}_{-13}	648
8	680^{+11}_{-7}	668

Table 6.2: Lower limits of M_D (GeV) for n = 3, 4, 5, 6, 7, and 8. Presented are: The central value and the 95% CL for data, 95% CL for the reduced data, 95% for the CDF Run I results, and the 95% CL for the Run I DØ Monojet search.

n	Data central	Data 95% CL	Reduced data 95% CL	CDF Run I 95% CL	Monojet 95% CL
3	585^{+17}_{-16}	580	619		730
4	600^{+18}_{-14}	581	632	549	680
5	618^{+15}_{-12}	602	648		640
6	650^{+17}_{-17}	630	678	581	630
7	665^{+12}_{-13}	648	690		620
8	680^{+11}_{-7}	668	700	602	

can be probed.

As noted in Subsection 5.3.2, the dataset still contains cosmic ray muon background which was not identified analytically. There are at least 28 events that can be visually identified as cosmic ray muons undergoing bremsstrahlung in the EMCal by use of event displays. This is a problem that future analysis in this particular channel will have to deal with. Table 6.2 contains a summary of the limits from the cited published searches, as well as the results from this study including the reduced bremsstrahlung dataset.

As noted in Section 5.1.1, this study uses 197 pb^{-1} of data which is about 17% of the data presently available at DØ for physics analysis. If we were to use the entire data set imposing the same requirements and without reducing the bremsstrahlung background, the 95% CL level curve in Figure 5.18 would be lowerd toward the central limit curve, assuming no signal events. This would result in higher limits for M_D ranging from about 20 GeV for the lower values of n to a few GeV for h igher values.

APPENDIX A

Cosmic Bremsstrahlung Events

Cosmic muons can produce photons or fake jets (plus $\not\!\!E_T$) final states in two ways: through photon radiation, and minimum ionization in the calorimeter cells. In the first case, a cosmic muon radiates a high energy photon, through bremsstrahlung, resulting in a single high E_T photon. The second case can arise when a cosmic muon travels roughly parallel to the beam line, traversing a longer distance in a given cell than a collision produced muon. The case in which jets are produced has been studied and the details can be found in Reference [60].

Analyses searching for single photon events are vulnerable to backgrounds from cosmic ray muons which undergo bremsstrahlung in the detector. Since these photons are not associated with a real event, an energy imbalance is also created. This combination can result in substantial number of fake events that have been selected using a single photon and missing energy E_T ($\not\!\!E_T$). Muons that undergo bremsstrahlung create a photon that travels essentially in the direction of the original muon. A method that uses fragments of muons information identified in the muon chambers and project these to the EMCAL was developed. If the EMCAL in these locations has a substantial amount of energy, these events are tagged as possible bremsstrahlung.

This study deals with the case in which photons are produced. To identify those events, we rely on muon information being present in at least two layers of the muon detector.

A.1 Data and EM Object Selection

For this study, the data set described in Section 5.1.2, was used. For completeness, the data selection cuts and requirements are briefly reviewed here.

The cuts are as follows:

- Events are required to have only one jet.

- Events must be in the central region of the calorimeter, *i.e.* $|\eta| < 1.1$.
- Use Scone algorithm for EM reconstruction.
- Require EM object ID 10 and 11.
- At least 90% of the energy has been deposited in the EM part of the calorimeter, *i.e.* EMFract > 0.90.
- Require that the EM cluster is isolated, *i.e.* EMIso < 0.15.
- EM candidate must be within ϕ fiducial.

Two different data sets were selected from the 1EMloose skim, a sample of $W \rightarrow e\nu$ events and a sample of single photons plus $\not\!\!E_T$ candidates. To discriminate between them, we used the spatial track match χ^2 probability. The cuts were: less than 0.001 for photon candidates, and greater than 0.001 for electrons. Furthermore, we reconstructed the W transverse mass peak and required the electron to be within 60 GeV and 90 GeV of the transverse mass distribution. The W sample was used to study the efficiency of the bremsstrahlung veto. The following additional requirements were made to increase the purity of the samples:

- HMx7 < 15.
- Muon veto: Events with reconstructed muons of any quality were removed, *i.e.* muons of loose, medium, tight, cosmic and cosmicT quality as described in in Section 4.3.2.
- For photons, we also vetoed on events with isolated tracks[1] and required $\not\!\!E_T > 45$ GeV and $p_T > 55$ GeV.
- For the $W \rightarrow e\nu$ sample, we required $\not\!\!E_T > 20$ GeV and $p_T > 25$ GeV.

Table A.1 contains the event count for the single photon plus $\not\!\!E_T$. Table A.2 contains the event count for the $W \rightarrow e\nu$ sample.

[1] An isolated track is defined as having: has $p_T > 10$ GeV, p_T sum of tracks in $dR < 0.4$ (where $dR = \sqrt{d\eta^2 + d\phi^2}$) about the candidate track to be < 2 GeV, and $dz_{dca} < 1.0$ cm

Table A.1: Summary of event count for single photon and $\not\!\!E_T$ sample.

EM object ID	1781
Muon veto	789
Isolated Track veto	781
$\not\!\!E_T$ requirement	769
Bremsstrahlung veto	242

Table A.2: Summary of event count for $W \rightarrow e\nu$ sample.

EM object ID	44712
Muon veto	41670
$\not\!\!E_T$ requirement	41670
Bremsstrahlung veto	40467

A.2 Bremsstrahlung Event Identification

The bremsstrahlung events were found while doing a data analysis in the single photon and $\not\!\!E_T$ channel. After all the data selection and quality cuts were made, a random sample of 50 candidate events was picked to make event displays. The goal was to see what these events looked like. Surprisingly, about 80% of the events apeared to have a muon traversing the detector and the path pointing, or going through, the photon candidate. Figures A.1 and A.2 are two views of an event display of one of these events. Figure A.1 explicitly shows a cosmic muon traversing the detector interacting with the BC-segment, A-segment, EM calorimeter, and the A-segment at the other side of the detector. Figure A.2 is a representation of the energy deposition in ϕ and the calculated $\not\!\!E_T$.

By viewing the displays, a simple strategy was devised: calculate the vectors from all of the muon A-segments hits to the location of the EM energy tower. Then calculate the angle between the vectors, this angle was referred to as χ. To do this, the methods xA(), yA() and zA() of the TMBMuon class were used. They return the coordinates of the A-segment hits and the projection of BC-layer hits to the A-segment. Figure A.3 is a typical event with the vectors and the angle. There are muon hits in two sides of the muon system, *i.e.* A-segment hits in the two sides. Figure A.4 shows the $cos(\chi)$ distribution. Events that have

at least one $|cos(\chi)|$ greater than 0.9 entry are vetoed. Figure A.4 also shows that most of the bremsstrahlung events do have hits in opposite sides of the muon system as would be expected from a muon that traverses the entire detector. The cut of $|cos(\chi)|$ greater than 0.9 was chosen to allow for the bending of the muons track due to the muon magnetic field and for trajectory change after the photon emission from bremsstrahlung.

A.3 Efficiencies

The $W \rightarrow e\nu$ sample, as described in Section A.1, was used to calculate the number of signal events that would be lost by the bremsstrahlung veto. The idea was to find out how often muon noise, or random muon hits in the muon system, would 'fake' a muon path that matches to the EM cluster location. The $W \rightarrow e\nu$ sample from data is the best sample to used for this purpose. Figure A.5 shows the cosine of χ distribution for the $W \rightarrow e\nu$ sample. The peak at $\cos(\chi)$ greater than 0.95 is from real electrons that happen to line up with muon A-segment or BC-segments hits. It is also possible that some of the W events are in coincidence with the muon undergoing bremsstrahlung. Figure A.6 show the ratio of the calorimeter energy (E)divided by the matched track momentum (P) which leads to the conclusion that these are electrons that are coming from the $W \rightarrow e\nu$ decay. It is also possible that these are real cosmic events that happen to have a high p_T track matched to the EM cluster. However, this is highly unlikely in this data sample since only events in a narrow range of the transverse mass of the W distribution was used. From Table A.2 it can be determined that 97% of the $W \rightarrow e\nu$ events pass the bremsstrahlung veto. Therefore, the method removes 3.0 ± 0.1(stat) % signal events. Note that the bremsstrahlung veto is being applied after the removal of all reconstructed muons from the W sample. This is done because the bremsstrahlung veto is designed to remove muons that traverse the entire detector which is not the case for real muons events originating from the interaction region. If the muon veto is removed, the bremsstrahlung veto removes an additional 1% of the W events. Both vetoes combined remove 9.5% of the W events.

A.4 Conclusion

It was determined that using muon segment information at the TMBTree level is a useful way to reduce the number of single photon events produced by cosmic bremsstrahlung events.

For the event selection of high p_T photons (p_T greater than 55 GeV) and $\not\!\!E_T$ ($\not\!\!E_T$ greater than 45 GeV), about 50% of the final sample are muons that undergo bremsstrahlung and the selection removed less then 3% of real photons. This is particularly important for studies using single photons and $\not\!\!E_T$ events.

A.5 The Code

Below is the code of the function that returns the angle between the vectors from muon A-segment hits and the EM object. The method takes in three pointers of TMBObject type, one for the EM candidate and two for the muon hits. This method should be called after all the EM ID requirements have been made on the candidate EM object. First, open the muon array and set the first pointer. Then, open a second loop over the muon array and set the second pointer ensuring that the pointer is for an other muon object. Here is an example:

```
// Open the first muon loop and set the first pointer
for( Int_t jmuon=0; jmuon<fMuon->GetLast()+1; jmuon++ ) {
   Muon = ( TMBMuon* ) fMuon->At(jmuon);

   // Open the second muon loop and set the second pointer
   // Ensure that it points to a different muon object
   for( Int_t kmuon=jmuon+1; kmuon<fMuon->GetLast()+1; kmuon++) {
      Muon1 = ( TMBMuon* ) fMuon->At(kmuon);

      // Call the fucntion and get chi
      chi = get_AngleChi(Emcl,Muon,Muon1);
      // fill the histogram
      Cosine_of_chi->Fill(cos(chi));

   }// Muon1 ////////////////////
}// Muon /////////////////////
```

The code for the get_AngleChi() function is as follows:

```
Float_t classname::get_AngleChi(TMBEmcl* Emcl,TMBMuon* Muon,TMBMuon* Muon1){
```

```
  // Declare the vectors
  TVector3 Vem; TVector3 Vmu1; TVector3 Vmu2;
  TVector3 Vme1; TVector3 Vme2;

  // Get the EM candidates coordinates
  Float_t Emcl_x = *(Emcl->floorX(3));
  Float_t Emcl_y = *(Emcl->floorY(3));
  Float_t Emcl_z = *(Emcl->floorZ(3));

  // Make the vector from the detector's origen to the EM cluster
  Vem.SetX( Emcl_x );
  Vem.SetY( Emcl_y );
  Vem.SetZ( Emcl_z );

  // Get the coordinates of the muon A-segment hits and make the vector.
  // This vector is from (0,0,0) to the muon hit location.
  Vmu1.SetX( Muon->xA() );
  Vmu1.SetY( Muon->yA() );
  Vmu1.SetZ( Muon->zA() );
  // Make vector from the Muon hit location the the EM cluster.
  Vme1 = Vem - Vmu1;
  // Make the second muon vector
  Vmu2.SetX( Muon1->xA() );
  Vmu2.SetY( Muon1->yA() );
  Vmu2.SetZ( Muon1->zA() );
  // Make the second vector from the Muon hit location to the EM cluster.
  Vme2 = Vem - Vmu2;

  // return the angle.
  return Vme1.Angle(Vme2);
}
```

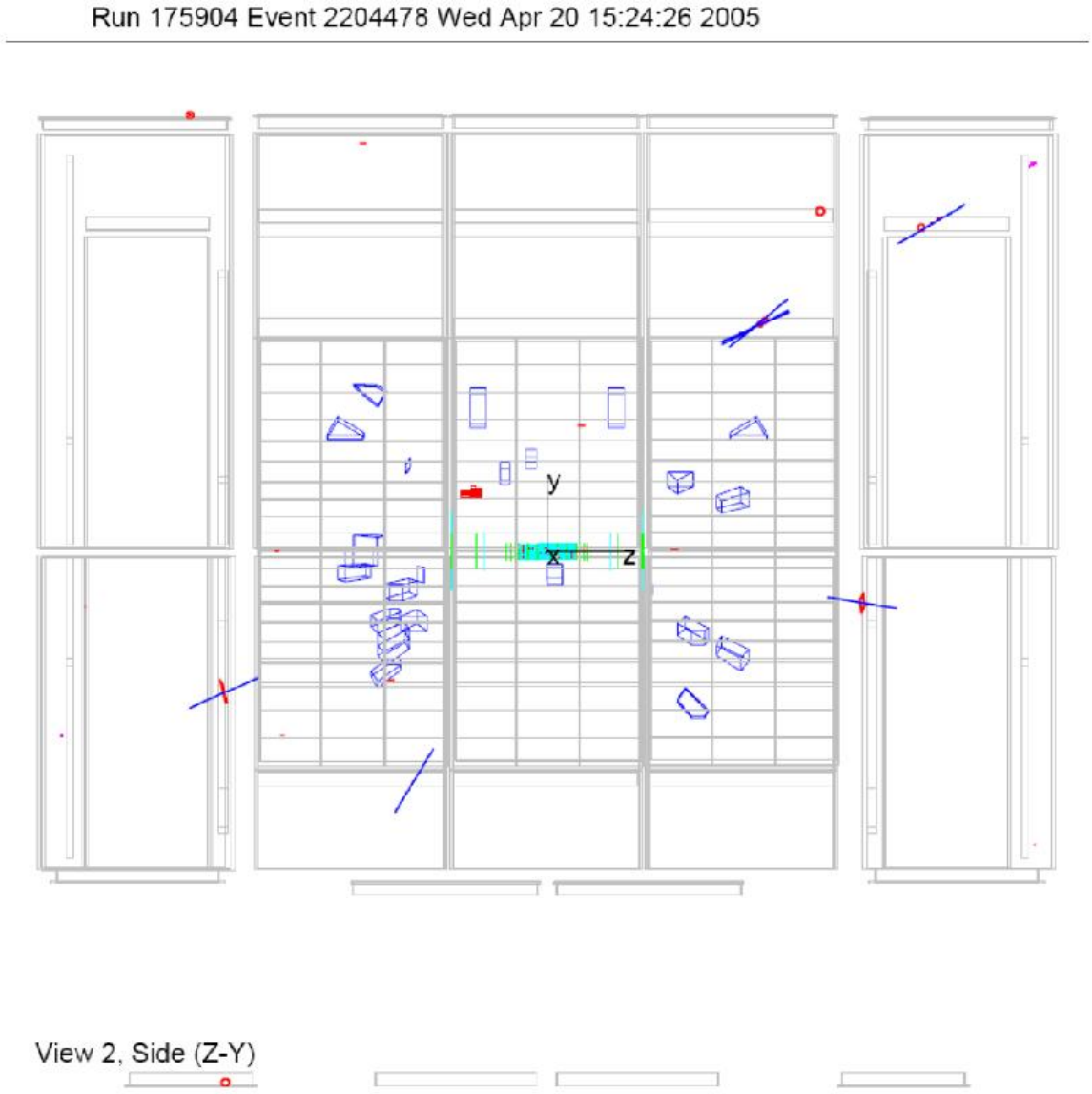

Figure A.1: $z - y$ view of a cosmic bremsstrahlung event

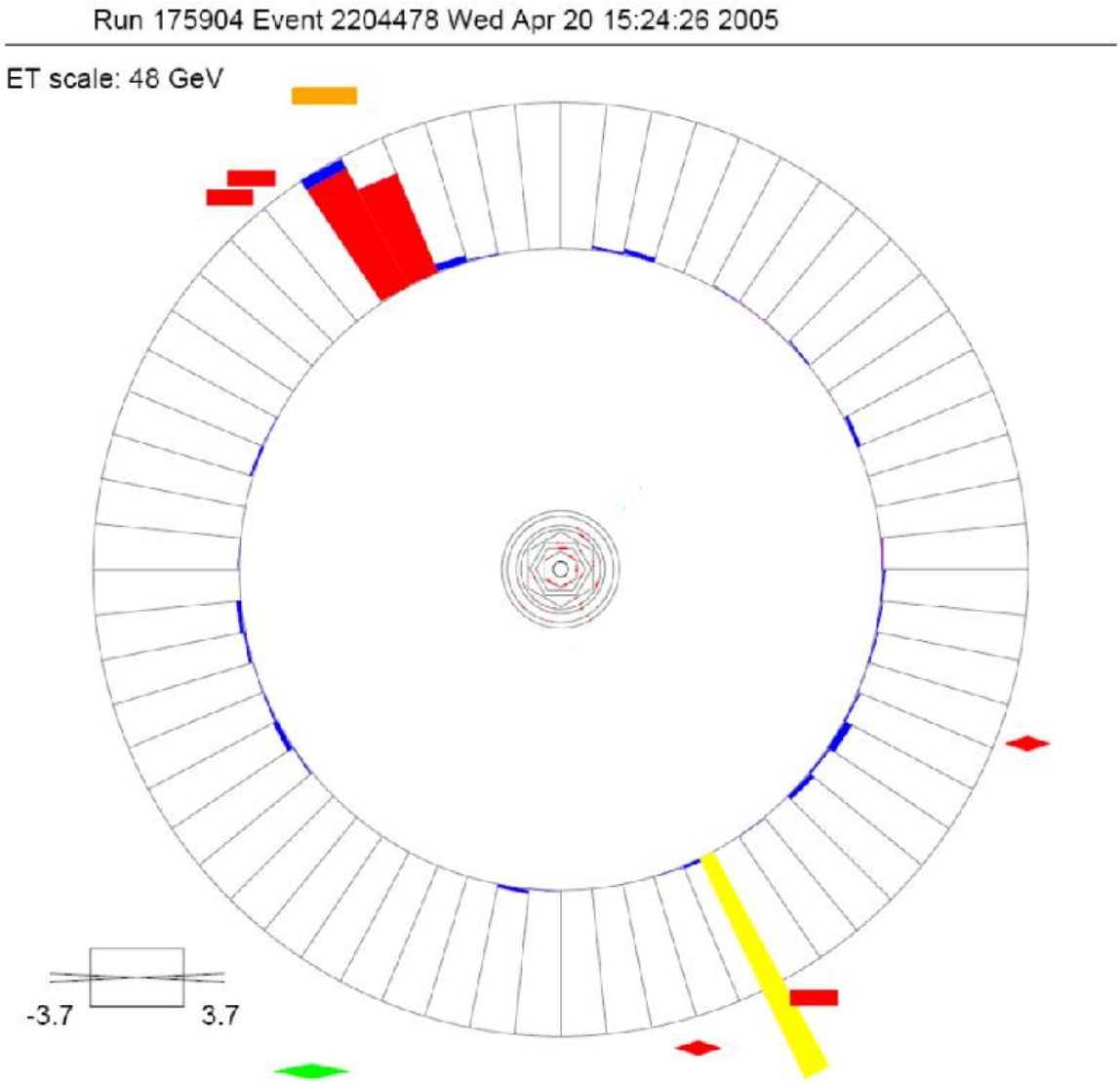

Figure A.2: ϕ view of a cosmic bremsstrahlung event

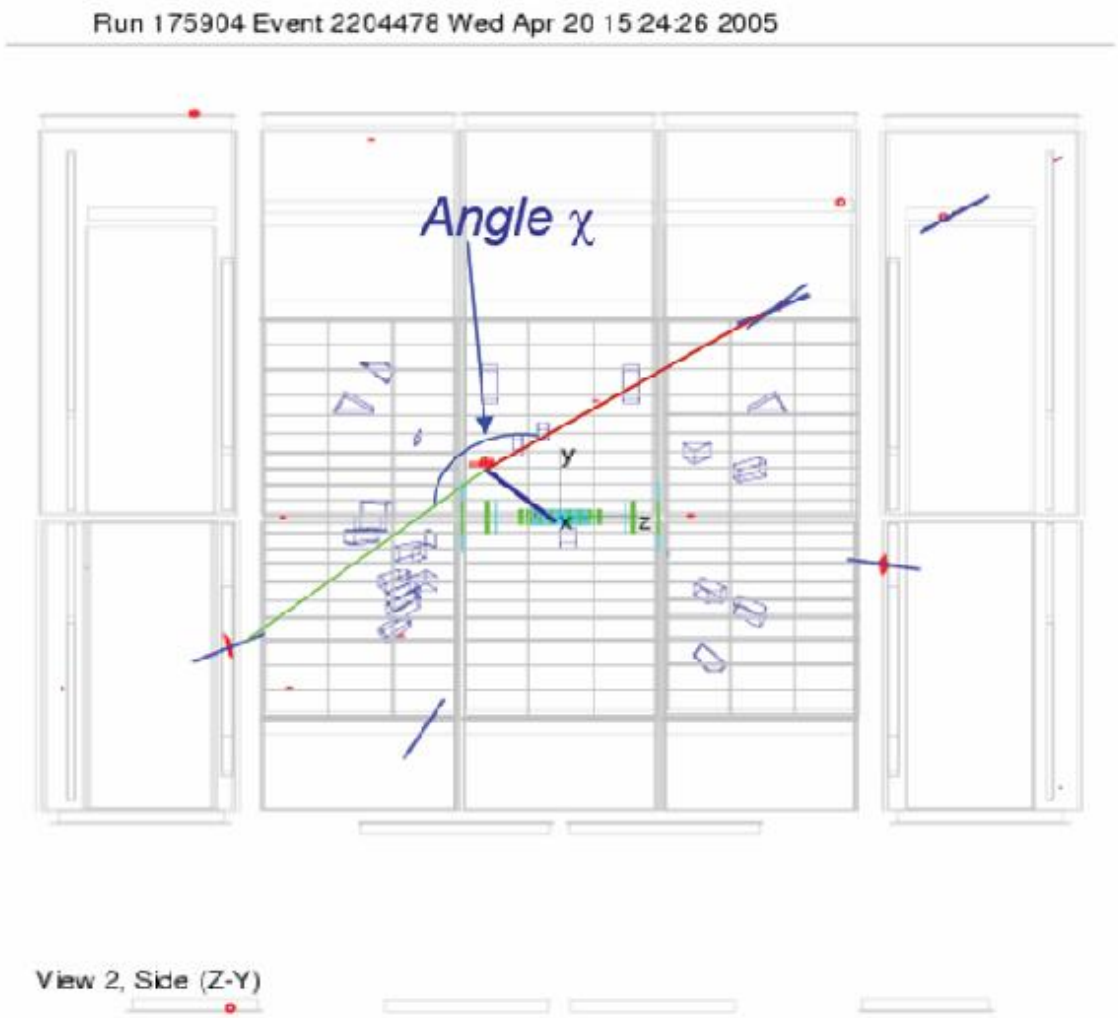

Figure A.3: The red and green lines depict the vectors from the muon hits, A-segments in this case, to the EM candidate. As this display shows, it is possible to have more than one χ calculation per event.

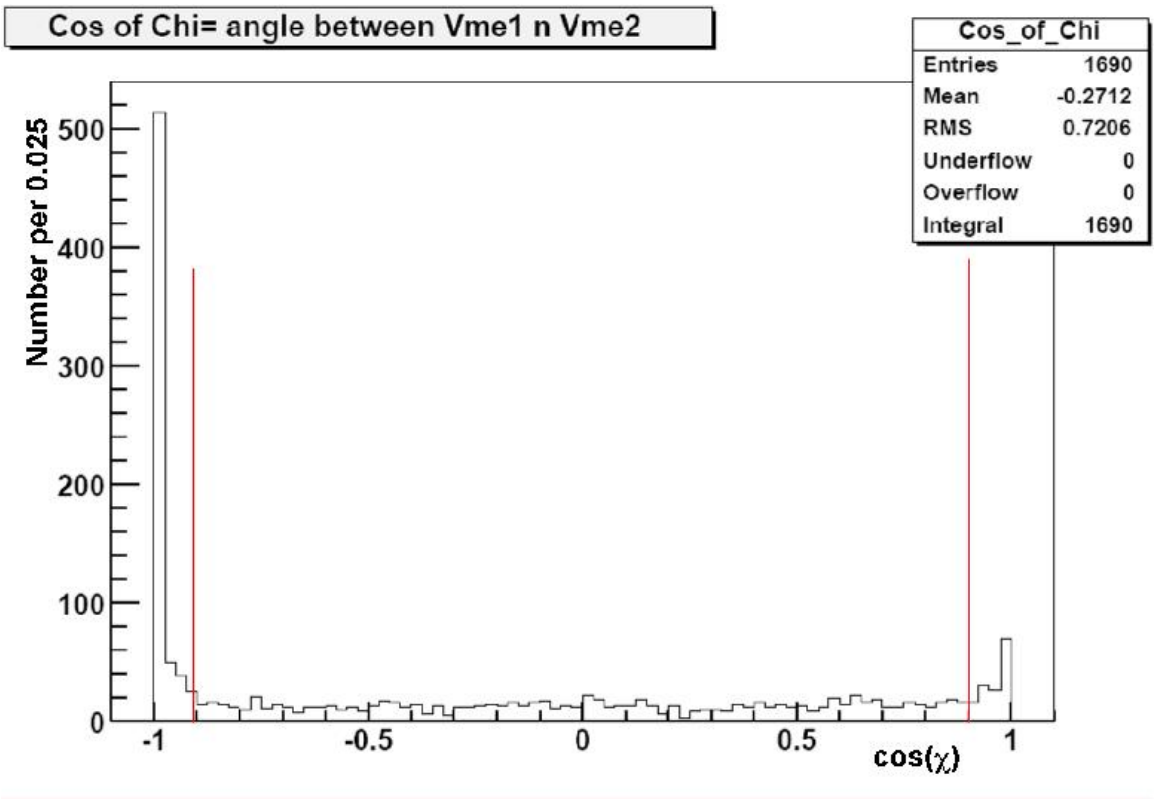

Figure A.4: Cosine of χ distribution for a single photon and $\not\!\!E_T$ data sample passing all of the photon ID requirements including muon veto, isolated track veto, and $\not\!\!E_T$ requirement. The red lines mark the values where the cut was made, which is $|cos(\chi)| > 0.9$.

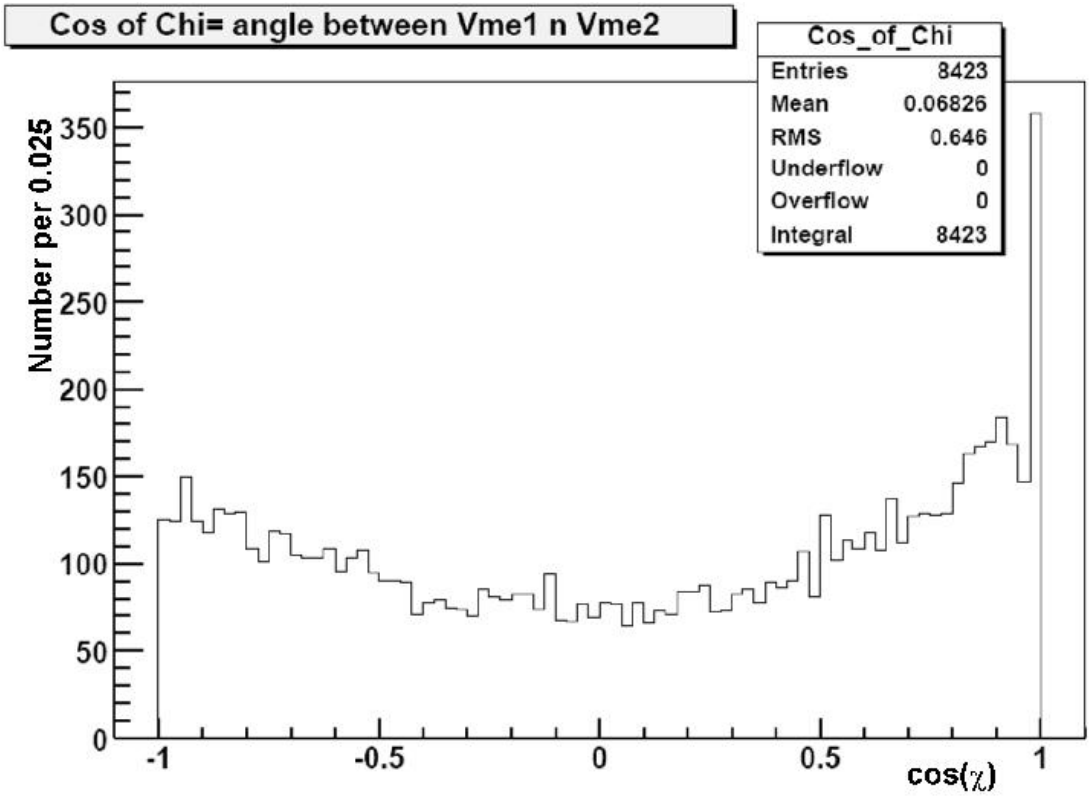

Figure A.5: Cosine of χ distribution for a data sample of $W \rightarrow e\nu$ events passing all of the photon ID requirements including muon veto and $\not\!\!E_T$ requirement.

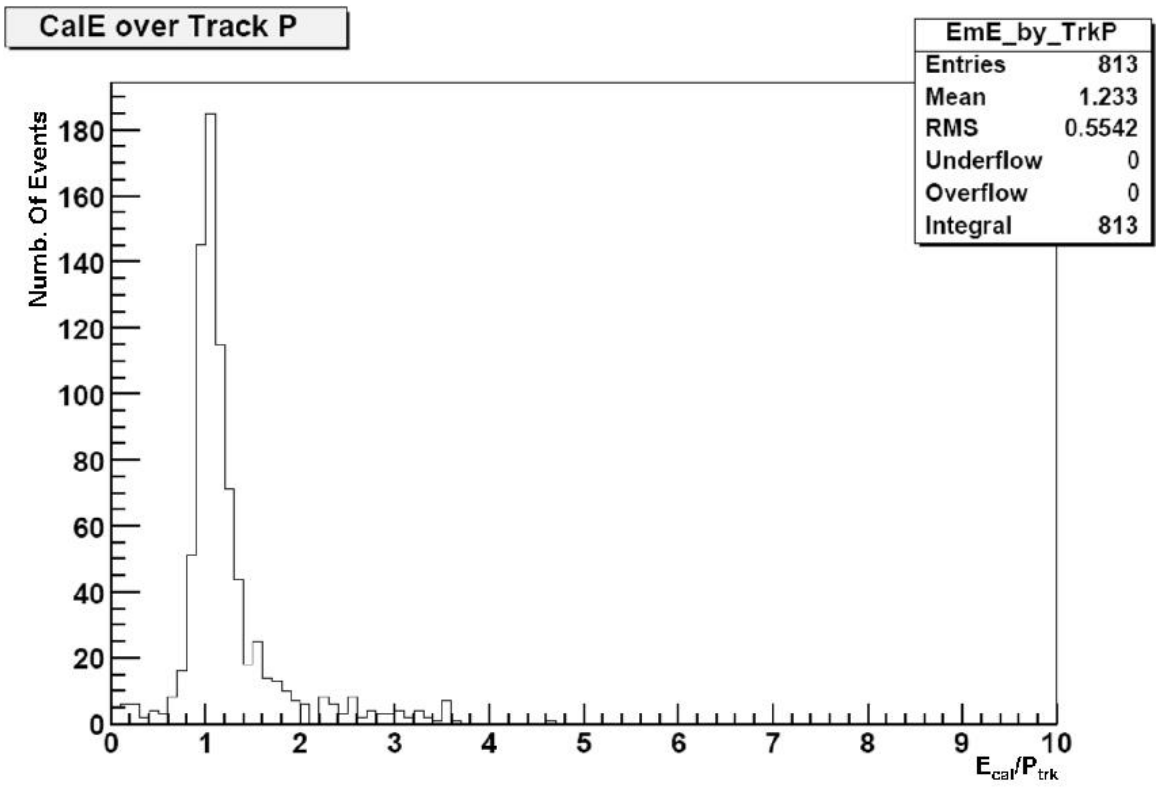

Figure A.6: E_{Cal}/P_{Track} distribution for events in $\cos(\chi) > 0.9$. This distribution indicates that these events are electrons from $W \rightarrow e\nu$ events that happen to line up with muon segments hits.

APPENDIX B

Track Match Efficiency Calculation

As described in Section 4.4, tracks, once found, are matched to calorimeter or muon clusters as part of particle reconstruction. This note answers the following question: Given a track, what is the matching efficiency in the case for electrons?

B.1 Data Selection

For this study, diEMloose skim data set was used as defined by the common sample (CS) group [49]. From the skim, the $Z \rightarrow ee$ peak was reconstructed and selected only those events within the range $20 < Z_{mass}(GeV) < 200$. The electron candidates in each diEM event were required to pass all of the EM ID criteria, as defined in Section 4.1.3 including the shower shape requirement. For completeness, the requirements are outlined here:

- In CC ($|\eta| < 1.0$).
- Use Scone algorithm for EM reconstruction.
- EM object ID 10 and 11.
- EMFract > 0.95.
- EMIso < 0.1.
- EM candidate must be within the $\eta - \phi$ fiducial.
- HMx7 < 15.

The Z peak for events that pass these requirements is shown in Figure B.1.

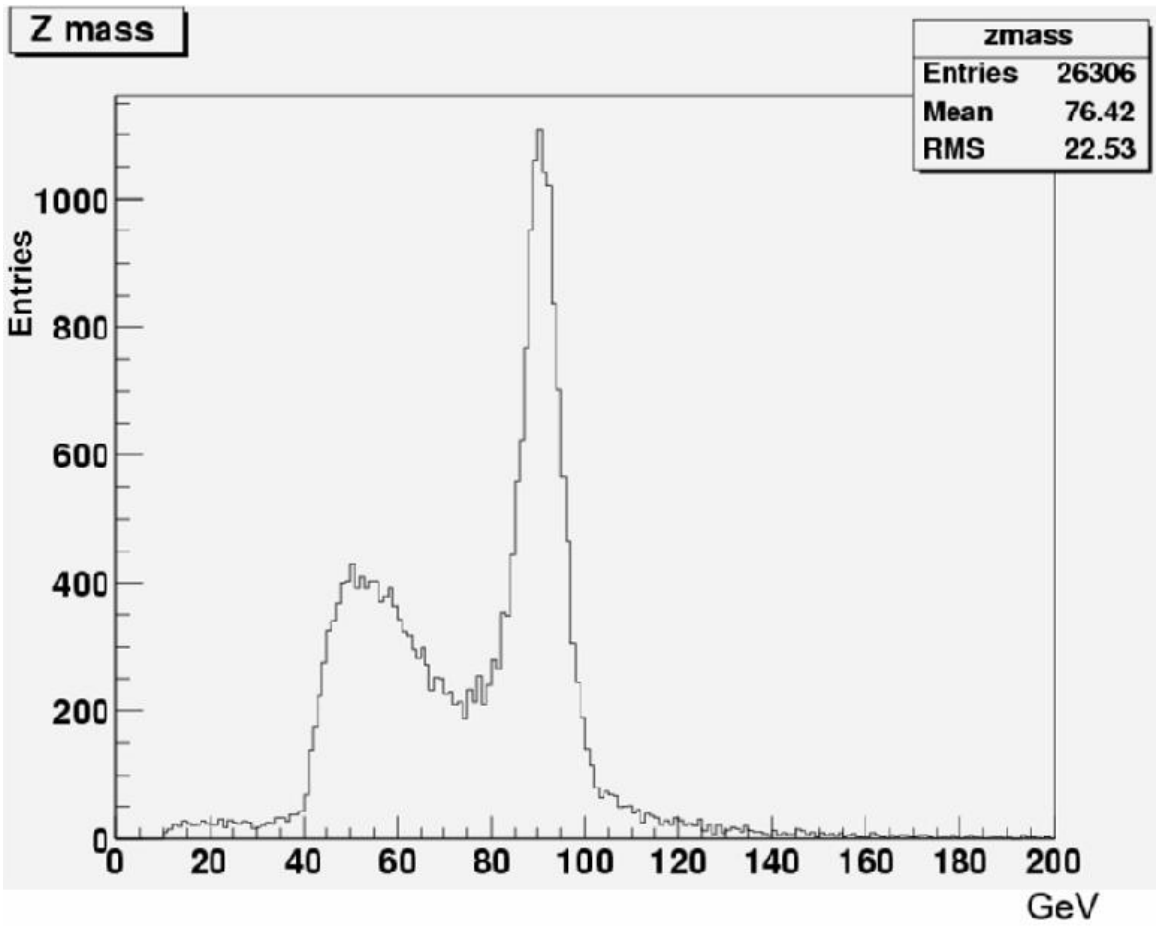

Figure B.1: $Z \rightarrow ee$ peak for diEM events after the certified EM ID requirements as defined in Section 4.1.3. Since these events do not have track match requirements, they includes events in which both EM objects have matched track, 1 EM object has a track match and neither EM objects has a matched track.

This data set was divided into two sets: one set with one EM object matched to a track, and one in which both EM objects had matched tracks. The fitted Z peak distributions for the two sets are shown in Figures B.2 and B.3.

B.2 The Efficiency Equation

The tracking efficiency equation was derived in the following way: Let N_2 be the number of events with two matched tracks, N_1 be the number of events with one matched track, N_0 the number of events with zero tracks and ϵ_{trk} be the tracking efficiency. Table B.1 shows

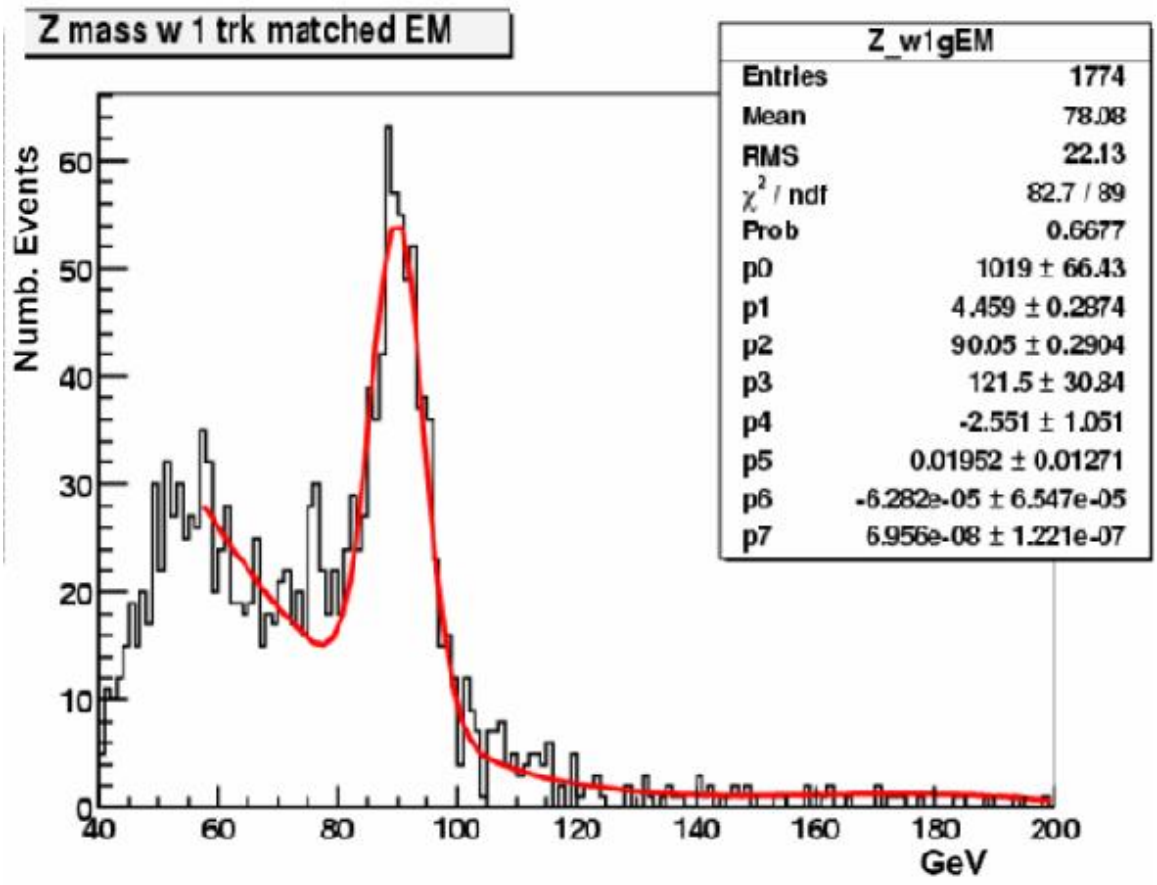

Figure B.2: $Z \rightarrow ee$ peak for events with one electron having a track match

what the efficiency per track in each event is. Base on Table B.1 the following equations can be written.

$$N_2 = N_Z \epsilon_{trk}^2, \tag{B.1}$$

$$N_1 = 2N_Z \epsilon_{trk}(1 - \epsilon_{trk}) \tag{B.2}$$

and

$$N_0 = N_Z (1 - \epsilon_{trk})^2. \tag{B.3}$$

Solving Equations B.1 and B.2 for ϵ_{trk} yields

$$\epsilon_{trk} = \frac{2N_2}{2N_2 + N_1}. \tag{B.4}$$

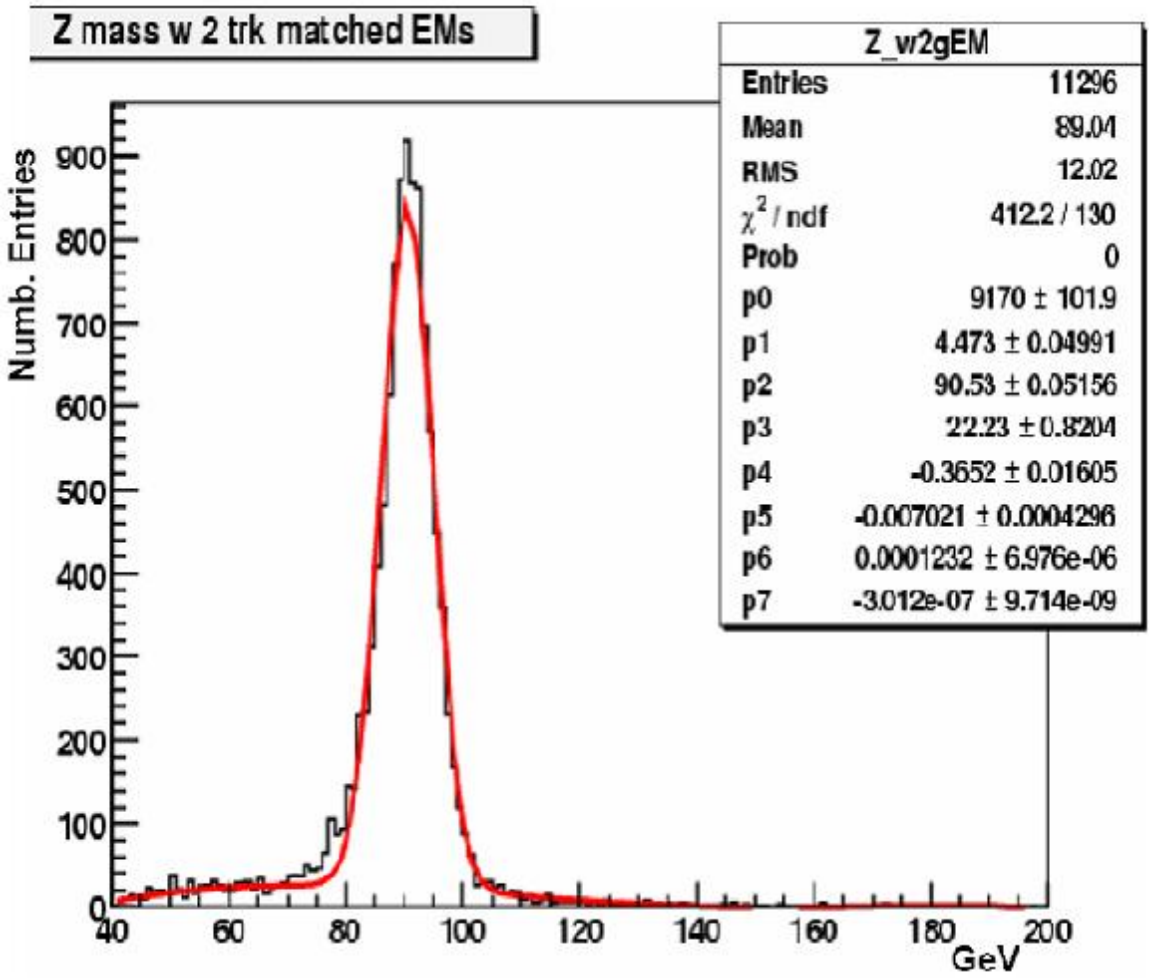

Figure B.3: $Z \rightarrow ee$ peak for events with two electrons having a track match

Table B.1: Presented is the estimation of the tracking efficiency, ϵ_{trk}, for each combination.

	Trk1	Trk2
N_2	ϵ_{trk}	ϵ_{trk}
N_1	ϵ_{trk}	1 - ϵ_{trk}
N_1	1 - ϵ_{trk}	ϵ_{trk}
N_0	1 - ϵ_{trk}	1 - ϵ_{trk}

B.3 Error Calculation

In this case, the error propagation equation is as follows [61]:

$$\sigma_X^2 = \sum \left(\frac{\partial X}{\partial a_i}\right)^2 \sigma_{a_i}^2 \tag{B.5}$$

For simplicity, let the track match efficiency equation be:

$$X = \frac{a}{a+b}. \tag{B.6}$$

After differentiating with respect to a, we get:

$$\frac{\partial X}{\partial a} = \frac{1}{a+b} - \frac{a}{(a+b)^2}. \tag{B.7}$$

Differentiating with respect to b, we get:

$$\frac{\partial X}{\partial b} = -\frac{a}{(a+b)^2}. \tag{B.8}$$

Substituting Equations B.7 and B.8 into Equation B.5, we get:

$$\sigma_X^2 = \left(\frac{1}{a+b} - \frac{a}{(a+b)^2}\right)^2 \sigma_a^2 + \frac{a^2}{(a+b)^4}\sigma_b^2 \tag{B.9}$$

After dividing Equation B.9 by X^2 and some algebra, it becomes:

$$\frac{\sigma_X^2}{X^2} = \frac{b^2}{(a+b)^2}\left(\frac{\sigma_a^2}{a^2} + \frac{\sigma_b^2}{b^2}\right). \tag{B.10}$$

Multiplying by X^2, some algebra and taking the square root, we get:

$$\sigma_X = X(1-X)\sqrt{\frac{\sigma_a^2}{a^2} + \frac{\sigma_b^2}{b^2}} \tag{B.11}$$

After substituting the original values for a and b, we get:

$$\sigma_{\epsilon_{trk}} = \epsilon_{trk}(1-\epsilon_{trk})\sqrt{\frac{\sigma_{2N_2}^2}{2N_2^2} + \frac{\sigma_{N_1}^2}{N_1^2}} \tag{B.12}$$

B.4 Results

With this method, the track matching efficiency was measured to be $\epsilon_{trk} = 94.7 \pm .3(stat)$ %.

REFERENCES

[1] Stanford Encyclopedia of Philosophy. http://plato.stanford.edu/entries/democritus/#2. 1

[2] V. Barger, R. Phillips, "Collider Physics", Updted Edition Addison Wesley, 1996. 1

[3] S. Weinberg. Phys. Rev. Lett. **19** 1264 (1967). 1, 5

[4] P.W. Higgs, Phys. Lett. **12**, 132 (1964). 5

[5] Particle Data Book: *Review of Particle Physics, Volume 592, Issues 1-4, (2005)* *http://pdg.lbl.gov (document), 2.1, 2.2, 2.3, 4.2.1, 4.2.1, 5.3.2*

[6] "Theory of Hadrons" http://www2.slac.stanford.edu/vvc/theory/hadrons.html 5

[7] M. Persic, P. Salucci, F. Stel astro-ph/9506004 2.2

[8] A. Errhmani, T. Ouali, "Dark energy description in an approximate 3-brane Brans-Dicke cosmology." arXiv:gr-qc/0602061, (2006) 2.2

[9] H. Baer, X. Tata, "Weak Scale Super Symetry" Cambridge University Press, (2006). 2.2

[10] W. Bernreuther hep-ph/0205279. 2.2

[11] G. Arnison et al.,*(for the UA1 Collaboration) Phys. Rev. Lett.* **B126** *398 (1983); Phys. Lett.* **B129** *273 (1983) 1*

[12] P. Bagnaia et al.,*(for the UA2 Collaboration) Phys. Rev. Lett.* **B129** *310 (1983); Z. Phys.* **C24** *1 (1984) 1*

[13] B. Abache et al.,*(for the DØ Collaboration) Phys. Rev. Lett.* **74** *2632 (1995). 1, 3.2*

[14] F. Abe et al.,*(for the CDF Collaboration) Phys. Rev. Lett.* **74** *2626 (1995). 1, 3.2*

[15] E.Witten Nucl. Phys. **B 471**, *(1996). 1*

[16] N. Arkani-Hamed, S. Dimopoulos, and G. Dvali Phys. Lett. **B 429**, *263 (1998). 1, 6, 6*

[17] G. Giudice, R. Rattazzi, and J.D. Wells Nucl. Phys. **B544**, *3 (1999) 6, 6, 2.3, 2.3, 2.3, 7*

[18] C.D. Hoyle, U. Schmidt, B.R. Heckel, E.G. Adelberger, J.H. Gundlach, D.J. Kapner, and H.E. Swanson,. Phys. Rev. **86**, 1418(2001). 6, 6

[19] E.G. Floratos and G.K. Leontaris, Phys. Lett. **B 465**, 95 (1999); A. Kehagias and K. Sfetsos, arXiv:hep-th/9905417. 6

[20] T. Han, J.D. Lykken, R.J. Zhang, Phys. Rev. **D59**, 105006 (1999) arXiv:hep-th/9811350 6

[21] Progression of Record Initial Luminosities (Webpage) http://www-d0.fnal.gob/runcoor/run2best.html#recordinit 3.1.2

[22] Fermi National Accelerator Laboratory, Batavia, Illinois (USA). Tevatron Run II Handbook. Internal FNAL Note. (http://www-bd.fnal.gov/runII/index.html). 3.2

[23] S. Abachi et al., (DØ). "The DØ Detector", Nucl. Instrum. Methods, **A552**, 372 (2005) 3.3

[24] For Additional information, see URL: http://www-d0.fnal.gov/hardware/upgrade/upgrade.html and links therein. 3.3

[25] S. Burdin et al., (for the DØ collaboration) D0note4961, "DØ SiliconTracker". 3.3.1

[26] The DØ Collaboration. "The DØ Upgrade Central Fiber Tracker: Technical Design Reprt", (1997). (http://d0server1.fnal.gov/projects/SciFi/cft_home.html). 3.3.2

[27] S. Blessing et al., (for the DØ Collaboration) Fermilab-Pub-05-341-E, arXiv:physiscs/0507191. 3.3.2, 3.3.5, 3.3.7, 3.3.7, 3.4.1, 3.4.2, 3.4.3

[28] M. Bhattachargee et al., Techincal Design Report of the Forward Preshower Detector for the DØ Upgrade. DØ note 3445, 1998. 3.3.3

[29] P. Baringer et al. Cosmic rad data analysis for the DØ Preshower detector. DØ note 3765, 2000. 3.3.3

[30] B. Baldin et al. (Muon Group). "Technical Design of the Central Muon System", Internal DØ note 3365. (updated version, 1998) 3.3.7, 3.3.7, 3.3.7

[31] C. Miao et al. (for the DØ collaboration), "The DØ Run II Luminosity Monitor", DØ note 3573, (1998). 3.4

[32] A.M. Patwa, Ph.D. Thesis, "The Forward Preshower System and a Study of the J/ψ Trigger with the DØ Detector" SUNY at Stony Brook (2002). 3.4.2

[33] F. Fleurent, "DØ Electron/Photon Analysis Package EMAnalyze". http://www-d0.fnal.gov/d0dist/dist/packages/em_analyze/v01-02-22/d0c/EMAnalyze_doc.ps 1

[34] A. Askew, Ph.D. Thesis, "Measurement of the $W\gamma \to \mu\nu\gamma$ Cross Section", Rice University, Houston Tx. (2004) 12, 12, 4.1.3, 4.1.3, 4.2.1, 4.2.3, 18

[35] S. Duensing, Ph.D. Thesis, "Measurement of the $Z^0 \to \tau\overline{\tau}$", University of Nijmegen/MIKHEF, Amsterdam, Netherlands (2004) 4.1.3

[36] G.C. Blazey et. al., "Run II Jet Physics" Proceeding of the QCD and Weak Boson Physics Workshop", hep-ex/0005012. 4.2.1

[37] J.L. Agram et. al., "Jet Energy Scale at DØ Run II", DØ Note 4720, (2005) (document), 4.2.2, 4.2.2, 4.5

[38] O. Peters et. al., "Muon Segment Algorithm" http://www-d0.fnal.gov/nikhef/muon_reco/segmentreco/ 4.3

[39] F. Deliot (internal document) http://www-d0.fnal.gov/~deliot/fitalg.ps 4.3

[40] C. Clement et. al, "Muon ID Certification for p14" DØ Note 4350 , v1.0, March 4, 2004. 4.3.2

[41] A. Garcia-Bellido et.al., Tracking/Vertexing http://www-d0.fnal.gov/global_tracking/. 4.4

[42] G. Borisov, "Ordering a Chaos... or Technical Details of AA Tracking." http://www-d0.fnal.gov/Run2Physics/WWW/algorithm.htm. 4.4

[43] A. Khanov, "HTF: Histograming methond for finding tracks. The algorithm description," DØ Note 3778, 2000. 4.4

[44] G. Hesketh, "Central Track Extrapolation Throught the DØ Detector," DØ Note 4079. 2003.

[45] A. Garcia-Bellido et.al., "Primary Vertex certification in p14," DØ Note 4320, 2004. 4.5, 15

[46] H. Greenlee, "The DØ Kalman Track Fit," DØ Note 4303, 2004. 4.4, 4.5

[47] U. Bassler, G. Bernardi, "Towards a Coherent Treatment of Calorimetric Energies: Missing Transverse Energy, Jets, E.M. Objects and T42 Algorithm," DØ Note 4042, 2002. 4.6

[48] J. Gardner, "Single EM Trigger Efficiency Using a Diem Tag and Probe Method, DØ Note 4338, (2004). 5.1.1, 5.2.2

[49] R. Houser, S. Sharyy (conveners), Common Sample Group, http://www-d0.fnal.gov/Run2Physics/cs/index.html 19, B.1

[50] A. Melnitchouk, Ph.D. Thesis, "Search for non-SM Light Higgs Boson in the $h \to \gamma\gamma$ Channel." Brown University, Providence, Rhode Island, 2004 5.2.2

[51] G. Steinbruck, Ph.D. Thesis, "Measurement of the Angular Distribution of Electrons from W Boson Decays," University of Oklahoma, Norman, Oklahoma, 1999 22

[52] T. Sjöstrand, http://www.thep.lu.se/~torbjorn/Pythia.html. 5.2.2, 5.2.2

[53] J. Grivaz, A. Meyer (conveners) http://www-d0.fnal.gov/Run2Physics/np/ 5.2.2

[54] A. Belyaev, private code for LED in the γ and $\not\!\!E_T$ channel. present email belyaev@pa.msu.edu 5.3.1

[55] S. Eno, M. Verzocchi. Conveners. http://www-d0.fnal.gov/computing/MonteCarlo/pmcs/pmcs_doc/pmcs.html 5.3.1

[56] J. Zhu, "Determination of Electron Energy Scale and Energy Resolution using P14 $Z^o \to e^+e^-$ data", DØ Note 4323, (2004). 28

[57] by CDF Collaboration (D. Acosta et. al). "Limits on Extra Dimensions and New Particle Production in the Exclusive Photon and Missing Energy Signature in $p\bar{p}$ Collisions at $\sqrt{s} = 1.8$ TeV." hep-ex/0205057 6

[58] A. Alton, A. Askew, O. Atramentov, Y. Maravin, "Photon Identification for DØ Run II Data," DØ Note 4487, 2004. 5.3.2

[59] By DØ Collaboration (V.M. Abazov et. al), "Search for large extra dimensions in the monojet + $\not\!\!E_T$channel at DØ ," **Phys. Rev. Lett. 90:251802, 2003**, e-Print Archive:**hep-ex/0302014** 6

[60] C. Hays, "Calorimeter-Based Cosmic Ray Rejection, DØ Note 3814, (2001). A

[61] Glen D. Cowan, "Lectures Notes on Data Analysis", Universität Siegen, (4/25/1996). B.3

BIOGRAPHICAL SKETCH

Jose A. Lazoflores

Jose A. Lazoflores was born on July 19, 1973, in the city of San Miguel, El Salvador. He emigrated to the United States, along with his family, in the spring of 1986. At the time, El Salvador was undergoing a civil war, which was the main reason why his family decided to emigrate. Upon arrival in the USA, his family settled in the city of Houston, Texas, where he lived until the age of 19. He graduated from Westfield High School on the spring of 1991. At the time of his high school graduation, he was not able to attend a university because he was not an American citizen. Tuition for non-citizens was beyond of what his family could afford. After two years of moving from job to job, he enlisted in the United States Air Force in May of 1993 and served for 3 years and 3 months. His goal at the time was to earn a commission and become a fighter pilot. His occupation in the Air Force, as en enlisted member, was to prepare hazardous material for air transportation. After being stationed in Elmendorf Air Force Base, Alaska, for 3 years, he was given a honorable discharge on August of 1996. After the Air Force, he attended Embry-Riddle University in Daytona Beach, Florida, where he was awarded a Bachelors degree in Engineering Physics. Upon arrival at Embry-Riddle, his goal was still to earn a bachelors degree and return to the Air Force as an officer and pursue a flying carrier, but that would soon change. At Embry-Riddle he developed an appreciation for physics, astronomy, philosophical literature and the history of science, among other subjects. These new interests proved to be a turning point in his plans and decided against returning to active duty. During this time, he became a member of the Δ X fraternity where he made friendships that have lasted longer than most friendships he has had prior to to his arrival at Embry-Riddle. He graduated in August of 1999. After his bachelors degree graduation, he decided to pursue his new found interest in science and

enrolled at Florida State University.

For Jose, its been a long journey. Parts of it have been great, some have been good, and parts have been not so good, but that is what life is all about. He enjoyed his life as a graduate student at FSU, but he believes that the best is still to come. He is looking forward to it.